Summer 8-15-2019

Quantum Nanophotonics: Deterministic Photon-based Quantum Logic Gate By Exploiting Few-photon Nonlinearity

Zihao Chen
Washington University in St. Louis

WASHINGTON UNIVERSITY IN ST.LOUIS

School of Engineering & Applied Science
Department of Electrical and Systems Engineering

Dissertation Examination Committee:
Jung-Tsung Shen, Chair
Shantanu Chakrabartty
Erik Henriksen
Matthew Lew
Kater Murch
Xuan 'Silvia' Zhang

Quantum Nanophotonics: Deterministic Photon-based Quantum Logic Gate By Exploiting Few-photon Nonlinearity

by
Zihao Chen

A dissertation presented to
The Graduate School
of Washington University in
partial fulfillment of the
requirements for the degree
of Doctor of Philosophy

August 2019
St. Louis, Missouri

Table of Contents

List of Figures

List of Tables

Acknowledgments

First I would like to express my gratitude to my advisor Dr. J. T. Shen for his doctoral training towards a person with honesty, integrity, open-mindness, and dignity. His specific five requirements, (1) be 100% honest; (2) be professional; (3) be well-articulated; (4) be modest and open-minded; and (5) read more and think deep, crystalize into credo to leave significant impacts on me. Secondly, I would like to thank my colleague Yao and my friends Yijian, Nan, etc. for their generous encouragements and insightful suggestions. Thirdly, I would like to acknowledge instructions and discussions from previous group members and other faculty members, instructors, etc. Last but not least, I would like to express my gratitude to my families and my girlfriend Xinpei for their unconditional love and support.

Zihao Chen

Washington University in Saint Louis

August 2019

Dedicated to my families.

ABSTRACT OF THE DISSERTATION

Quantum Nanophotonics: Deterministic Photon-based Quantum Logic Gate

By Exploiting Few-photon Nonlinearity

by

Zihao Chen

Doctor of Philosophy in Electrical Engineering

Washington University in St. Louis, 2019

Professor Jung-Tsung Shen, Chair

Photon-based quantum logic gate has substantial advantages over conventional atom-based designs as a result of a longer coherence time and an inherent compatibility with quantum communication protocol of flying qubits, photons. As a vital logic gate for universal quantum computing, the two-photon controlled-phase gate demands a few-photon nonlinearity, which historically suffers from either an indeterministic nature in the linear optics regime, or a weak nonlinearity within naturally-occurring materials in the nonlinear optics regime. It is intriguing yet challenging to deliver a logic gate design by exploiting a genuine few-photon nonlinearity. In this dissertation, we study a particular one-dimensional quantum nanophotonic system that offers the desired few-photon nonlinearity through light-matter interactions in the quantum limit (*i.e.*, between light quanta of photons and individual material formation of atoms). Towards this end, we study the exotic photonic trimer state generation to first demonstrate few-photon nonlinearity. Then we report the breakdown of the non-Hermitian Hamiltonian for correlated multi-photon process to unveil the non-trivial effects of few-photon nonlinearity. Finally by exploiting such a nonlinearity, we present a deterministic two-photon controlled-phase gate proposal, and further showcase universal quantum logic gate designs in quantum nanophotonic systems.

Chapter 1

Introduction

To design quantum logic gate for quantum computing is intriguing yet challenging. On one hand, it is intriguing because quantum computing algorithm enables striking speedup over the best known classic one (*e.g.*, exponential speedup for factorizing a large prime number in Shor's algorithm [1] and a quadratic speedup for Grover's search algorithm [2]). On the other hand, it is yet challenging because designing quantum logic gates that have an adequately long coherence time and robust entanglement property in a large scale, are fundamentally difficult.

Conventionally, the quantum logic gate implementations exploit stationary qubits of atoms by encoding binary information in atomic excited and ground states. Practical platforms include trapped ions [3], superconducting qubits [4], quantum dots [5], nuclear magnetic resonance [6, 7], nuclear spin [8], nitrogen-vacancy center in diamond [9], etc. Albeit the atom-based technique is rather mature, photon-based implementations may be advantageous [10] because photons (1) have a longer coherence time; (2) do not require extra carriers; and (3) are readily compatible with quantum communication protocol [11].

To perform a universal quantum computing task, it suffices to employ a complete set of four logic gates at minimum, which is constituted by three single-qubit gates and one two-qubit gate [12]. The single-qubit gate falls into the linear regime entirely while the two-qubit one requires a genuine quantum nonlinearity. For the two-qubit gate, the implementation can be further categorized into linear and nonlinear optical ones. In the linear optics regime (*e.g.*, KLM [13], boson sampling [14], cluster-state scheme [15, 16], and quantum teleportation [17]), as a result of lack of nonlinearity devices, the measurement has to be conducted to introduce the effective nonlinearity through wave function collapses. Thus, the linear scheme is indeterministic in nature. In the nonlinear optics scheme (*e.g.*, cross-Kerr $\chi^{(3)}$ nonlinearity scheme [18]), naturally-occurring materials scarcely offer the desired strong nonlinearity, thus significantly compromising practical feasibility. For example, the nonlinear phase can be estimated by $\hbar\omega^2\Delta t\chi^{(3)}/4\epsilon_o V$ for a typical $\chi^{(3)}$ material of silicon at infrared [19], where ω is the light frequency, $\chi^{(3)}$ is the third-order susceptibility coefficient, Δt denotes the interaction time, V is the interaction volume, and ϵ_o is vacuum permittivity. By plugging in the numerical value of $\omega \sim 10^{14} Hz$, $\chi^{(3)} \sim 10^{-19} m^2 V^{-2}$, $\Delta t \sim 10 ps$, and $V \sim 0.1 cm^3$, it can be shown that the phase has the order of magnitude of $10^{-18} \ll \pi$, which is almost infeasible in practice. A scheme that takes advantage of a genuine few-photon nonlinearity is yet to be proposed.

Photons are electrical neutral and typically have weak interactions, thus rarely manifesting a few-photon nonlinearity. To introduce the desired nonlinearity, light-matter interactions in the quantum limit have to come into play. Specifically, down to the quantum level, interactions between light quanta (photons) and individual matter formation of dipole emitters (atoms) are taken into account. As a result of the fermionic nature, an atom can absorb or spontaneously emit only one photon at the same time to be saturated. Then the atom behaves seemingly differently to a second photon, thereby introducing the few-photon nonlinearity [20, 21].

The resulting nonlinearity manifests as photon correlations, where the collective few-photon behavior can not be predicted by that of an individual photon. The associated nonlinear phase may potentially provide desired ingredient for quantum logic gate designs. Towards this end, my doctoral work focuses on generations and applications of photon correlation in a particular one-dimensional quantum nanophotonic system [22–34], where photonic mode in the continuum is coupled to individual emitters. Specifically, I am motivated by the following questions: (1) how photon correlations are generated; (2) what unknown quantum effects are driven by photon correlations; and (3) how the resulting photon correlations facilitate photon-based logic gate designs.

In Chapter 2, we answer the first question by studying the photonic trimer generation mechanism through a coherent nonlinear three-photon scattering process. We confirm the trimer signature by exploiting the wave function representation and correlation function metrics. Moreover, we show that our formalism agrees with a recent experimental observation.

In Chapters 3, 4, and 5, we answer the second question by investigating the effects of dissipations on photon correlations. Specifically, in Chapters 3 and 4, we develop the dissipation theory of correlated multi-photon transport for scattering loss and material loss scenarios, respectively, Our work, for the first time, unearths the breakdown of the widely-adopted non-Hermitian Hamiltonian description for correlated multi-photon process. In Chapter 5, we report a novel dissipation-induced photonic correlation transition phenomenon.

In Chapters 6 and 7, we answer the third question by presenting deterministic two-photon controlled-phase gate proposal by exploiting photonic dimer generations. Furthermore, we showcase the design of a complete set of four quantum logic gates for universal quantum computing.

Chapter 2

Generation of Photonic Trimer

2.1 Introduction

Bound states are a class of quantum mechanical states where wave functions of constituent particles are localized. Typically, they are formed due to interactions between constituent particles, which is described by the binding energy. For example, molecules are bound states of atoms due to electrostatic interactions. Nonetheless, photons are electrical neutral and rarely interact, thus making it difficult to form photonic bound states. Recently, it has been shown that photons can form bound states due to inherent entanglement mediated by a saturated two-level system [20]. Different from conventional bound states, such states are entanglement-driven as no binding energy concept is demanded. Photonic bound states that involve the least photon number, *i.e.*, photonic dimer has been both theoretically [20, 35–37], experimentally [38], and numerically confirmed [39].

Recently, the bound state of three photons, called a photonic trimer, has also been theoretically predicted in a particular quantum nanophotonic system, waveguide quantum electrodynamics

(waveguide QED) system [24, 40–52], and was recently experimentally confirmed in Rydberg atomic gas [53]. Such a photonic trimer has three salient features. First, in real space, three photons are collocated where the probability amplitude decays exponentially as the distance between any two photons increases. Once generated in the quantum nonlinear medium (*i.e.*, one-dimensional waveguide of continuum modes coupled to two-level systems (*e.g.*, Rydberg atom [38], quantum dot [25], superconducting qubit [27], or N-V center [9]), it can propagate in a linear medium or even in the vacuum, without the assistance of nonlinear medium anymore. Secondly, in the frequency space, three photons are anti-correlated as the total energy of three constituent photons is a specified constant regardless of the frequency-space profile. Such a feature may tremendously enable applications in three-photon fluorescence microscopy [54, 55], entanglement-assisted deep-subwavelength lithography [56], multi-photon-driven super resolution in quantum imaging [57, 58]. Thirdly, generated trimer is imprinted on a phase shift at the order of π, which provides the essential ingredient in designing photon-based quantum logic gates [59].

In this chapter, we present a computational formalism to study photonic trimer generations through coherent three-photon scattering process in waveguide QED system. We confirm the trimer signatures by examining wave functions and correlation function metrics. Our results unveil the substantial role of three-photon hybrid state in three-photon scattering process. Moreover, we show that our formalism can readily describe the recent experimental results.

2.2 System and Hamiltonian

The waveguide QED system, as depicted in Fig. 2.1, consists of a two-level atom coupled to a one-dimensional single-mode waveguide. Consider a three-photon Fock state $|3\rangle$ incident

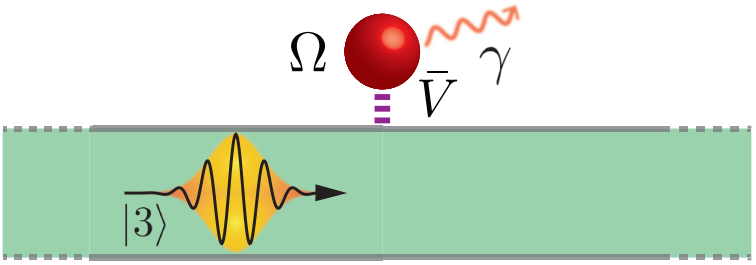

Figure 2.1: Schematics of the waveguide QED system. A two-level atom (represented by a red sphere) is coupled to a one-dimensional single-mode photonic waveguide. A three-photon Fock state $|3\rangle$ is incoming from the left.

from the left. The Hamiltonian of the system is

$$\begin{aligned}\frac{H}{\hbar} =& \int dx c_R^\dagger(x)(-iv_g\partial_x)c_R(x) + \int dx c_L^\dagger(x)(iv_g\partial_x)c_L(x) \\ &+ \sum_{j=R,L}\int dx \bar{V}\delta(x)\left[c_j^\dagger(x)\sigma_- + \sigma_+ c_j(x)\right] + (\omega_e - i\gamma)a_e^\dagger a_e + \omega_g a_g^\dagger a_g,\end{aligned} \tag{2.1}$$

where $c_R^\dagger(x)$ ($c_R(x)$) denotes the creation (annihilation) operator for a right-propagating photon at position x. $c_L^\dagger(x)$ and $c_L(x)$ are similarly defined for a left-propagating photon. $a_e^\dagger$ (a_e) is the creation (annihilation) operator for the atomic excited state. $a_g^\dagger$ and a_g are similarly defined for the atomic ground state. $\sigma_+ = a_e^\dagger a_g$ ($\sigma_- = a_g^\dagger a_e$) represents the atomic raising (lowering) operator. $\hbar\omega_e$ ($\hbar\omega_g$) is the energy of the atomic excited (ground) state. $\Omega \equiv \omega_e - \omega_g$ is the atomic transition frequency. v_g is group velocity of photons and $\bar{V}$ is atom-photon coupling. $\Gamma \equiv \bar{V}^2/v_g$ and γ are the atomic decay rate into the waveguided and non-waveguided modes, respectively [60]. The general form of the three-photon state is given by

$$\begin{aligned}|\Phi(t)\rangle =& \Big(\sum_{i,j=R,L}\int dx_1 dx_2\, e_{ij}(x_1,x_2,t)\frac{1}{\sqrt{2!}}c_i^\dagger(x_1)c_j^\dagger(x_2)\sigma_+ e^{-i\omega_e t} \\ &+ \sum_{i,j,k=R,L}\int dx_1 dx_2 dx_3\, \phi_{ijk}(x_1,x_2,x_3,t)\frac{1}{\sqrt{3!}}c_i^\dagger(x_1)c_j^\dagger(x_2)c_k^\dagger(x_3)e^{-i\omega_g t}\Big)|\varnothing\rangle,\end{aligned} \tag{2.2}$$

where $|\varnothing\rangle$ is the vacuum state that has no waveguided photon and the atom is at the ground state. ϕ_{ijk} denotes the wave function for three waveguided photons in the ijk branch $(i,j,k=R,L)$. e_{ij} represents the amplitude wherein the atom is excited and two waveguided photons are in the ij branch. By applying the Schrödinger equation $H|\Phi(t)\rangle = i\hbar\partial_t|\Phi(t)\rangle$, one obtains the following equations of motion

$$
\begin{aligned}
\partial_t\phi_{RRR} &= -v_g\left(\partial_{x_1}+\partial_{x_2}+\partial_{x_3}\right)\phi_{RRR} - \frac{i\bar{V}}{\sqrt{3}}\Big[\delta(x_1)e_{RR}(x_2,x_3)+\delta(x_2)e_{RR}(x_1,x_3)+\delta(x_3)e_{RR}(x_1,x_2)\Big]e^{-i\Omega t},\\
\partial_t\phi_{RRL} &= -v_g\left(\partial_{x_1}+\partial_{x_2}-\partial_{x_3}\right)\phi_{RRL} - \frac{i\bar{V}}{\sqrt{3}}\Big[\delta(x_1)e_{RL}(x_2,x_3)+\delta(x_2)e_{RL}(x_1,x_3)+\delta(x_3)e_{RR}(x_1,x_2)\Big]e^{-i\Omega t},\\
\partial_t\phi_{RLR} &= -v_g\left(\partial_{x_1}-\partial_{x_2}+\partial_{x_3}\right)\phi_{RLR} - \frac{i\bar{V}}{\sqrt{3}}\Big[\delta(x_1)e_{LR}(x_2,x_3)+\delta(x_2)e_{RR}(x_1,x_3)+\delta(x_3)e_{RL}(x_1,x_2)\Big]e^{-i\Omega t},\\
\partial_t\phi_{RLL} &= -v_g\left(\partial_{x_1}-\partial_{x_2}-\partial_{x_3}\right)\phi_{RLL} - \frac{i\bar{V}}{\sqrt{3}}\Big[\delta(x_1)e_{LL}(x_2,x_3)+\delta(x_2)e_{RL}(x_1,x_3)+\delta(x_3)e_{RL}(x_1,x_2)\Big]e^{-i\Omega t},\\
\partial_t\phi_{LRR} &= v_g\left(\partial_{x_1}-\partial_{x_2}-\partial_{x_3}\right)\phi_{LRR} - \frac{i\bar{V}}{\sqrt{3}}\Big[\delta(x_1)e_{RR}(x_2,x_3)+\delta(x_2)e_{LR}(x_1,x_3)+\delta(x_3)e_{LR}(x_1,x_2)\Big]e^{-i\Omega t},\\
\partial_t\phi_{LRL} &= v_g\left(\partial_{x_1}-\partial_{x_2}+\partial_{x_3}\right)\phi_{LRL} - \frac{i\bar{V}}{\sqrt{3}}\Big[\delta(x_1)e_{RL}(x_2,x_3)+\delta(x_2)e_{LL}(x_1,x_3)+\delta(x_3)e_{LR}(x_1,x_2)\Big]e^{-i\Omega t},\\
\partial_t\phi_{LLR} &= v_g\left(\partial_{x_1}+\partial_{x_2}-\partial_{x_3}\right)\phi_{LLR} - \frac{i\bar{V}}{\sqrt{3}}\Big[\delta(x_1)e_{LR}(x_2,x_3)+\delta(x_2)e_{LR}(x_1,x_3)+\delta(x_3)e_{LL}(x_1,x_2)\Big]e^{-i\Omega t},\\
\partial_t\phi_{LLL} &= v_g\left(\partial_{x_1}+\partial_{x_2}+\partial_{x_3}\right)\phi_{LLL} - \frac{i\bar{V}}{\sqrt{3}}\Big[\delta(x_1)e_{LL}(x_2,x_3)+\delta(x_2)e_{LL}(x_1,x_3)+\delta(x_3)e_{LL}(x_1,x_2)\Big]e^{-i\Omega t},\\
\partial_t e_{RR} &= -\gamma e_{RR} - v_g\left(\partial_{x_1}+\partial_{x_2}\right)e_{RR} - i\frac{\bar{V}}{\sqrt{3}}\Big[\phi_{RRR}(0,x_1,x_2)+\phi_{RRR}(x_1,0,x_2)\\
&+\phi_{RRR}(x_1,x_2,0)+\phi_{RRL}(x_1,x_2,0)+\phi_{RLR}(x_1,0,x_2)+\phi_{LRR}(0,x_1,x_2)\Big]e^{i\Omega t},\\
\partial_t e_{RL} &= -\gamma e_{RL} - v_g\left(\partial_{x_1}-\partial_{x_2}\right)e_{RL} - i\frac{\bar{V}}{\sqrt{3}}\Big[\phi_{RRL}(0,x_1,x_2)+\phi_{RRL}(x_1,0,x_2)\\
&+\phi_{RLR}(x_1,x_2,0)+\phi_{RLL}(x_1,0,x_2)+\phi_{RLL}(x_1,x_2,0)+\phi_{LRL}(0,x_1,x_2)\Big]e^{i\Omega t},\\
\partial_t e_{LR} &= -\gamma e_{LR} + v_g\left(\partial_{x_1}-\partial_{x_2}\right)e_{LR} - i\frac{\bar{V}}{\sqrt{3}}\Big[\phi_{RLR}(0,x_1,x_2)+\phi_{LRR}(x_1,0,x_2)\\
&+\phi_{LRR}(x_1,x_2,0)+\phi_{LRL}(x_1,x_2,0)+\phi_{LLR}(x_1,0,x_2)+\phi_{LLR}(0,x_1,x_2)\Big]e^{i\Omega t},
\end{aligned}
\tag{2.3}
$$

$$\partial_t e_{LL} = -\gamma_a e_{LL} + v_g\left(\partial_{x_1} + \partial_{x_2}\right) e_{LL} - i\frac{\bar{V}}{\sqrt{3}}\Big[\phi_{RLL}(0, x_1, x_2) + \phi_{LRL}(x_1, 0, x_2) + \phi_{LLR}(x_1, x_2, 0) + \phi_{LLL}(0, x_1, x_2) + \phi_{LLL}(x_1, 0, x_2) + \phi_{LLL}(x_1, x_2, 0)\Big] e^{i\Omega t}. \tag{2.4}$$

To investigate photon correlations after scattering, an uncorrelated three-photon pulse, described by a product state $\phi_{\text{in}}(x_1, x_2, x_3) = \phi(x_1)\phi(x_2)\phi(x_3)$, is injected into the waveguide from the left, *i.e.*, $\phi_{RRR}(t = 0) = \phi_{\text{in}}$. In particular, each photon has a Gaussian profile, described by $\phi(x) = 1/(2\pi\sigma^2)^{1/4} e^{-(x-x_o)^2/4\sigma^2 + i\omega_o x/v_g}$ where ω_o, σ, and $x_o = -3.76\sigma$ are center frequency, spatial width, and initial position, respectively. Each photon is resonant with the non-dissipative atom ($\delta \equiv \omega_o - \Omega = 0,\ \gamma = 0$), and has a narrow bandwidth $v_g/2\sigma$ ($= \Gamma/10$), thereby leading to a stronger atomic response, and thus a coherent three-photon scattering. Notably, correlation signatures are only relevant to the atom-photon interaction bandwidth Γ as long as photon bandwidth is adequately small (*i.e.*, $v_g/2\sigma \ll \Gamma$). In real-space representation, $|\phi_{\text{in}}|^2$ is represented by a gray sphere in Fig. 2.2(a). Since the atom is of a fermionic nature, it can only interact with one photon at the same time and become saturated, thus leading to photon entanglement (*i.e.*, photon correlation). To investigate photon correlations, we evolve the spatio-temporal three-photon dynamics by adopting an ab-initio momentum-space numerical methods as discussed in Appendix A, and record the wave function after scattering.

2.3 Three-photon Wave Function

After scattering, scattered wave function is plotted in Fig. 2.2(b) from the perspective of $x_1 = -x_2 = x_3$ to provide an overall view, and in Fig. 2.2(c) from the perspective of $x_1 = x_2 = x_3$ to aid the visualization of particular geometric characteristics. For three transmitted photons in the RRR branch, $|\phi_{RRR}|^2$ forms a spindle-shaped object that is longitudinally localized along the diagonal line (described by $x_1 = x_2 = x_3$, see the cyan

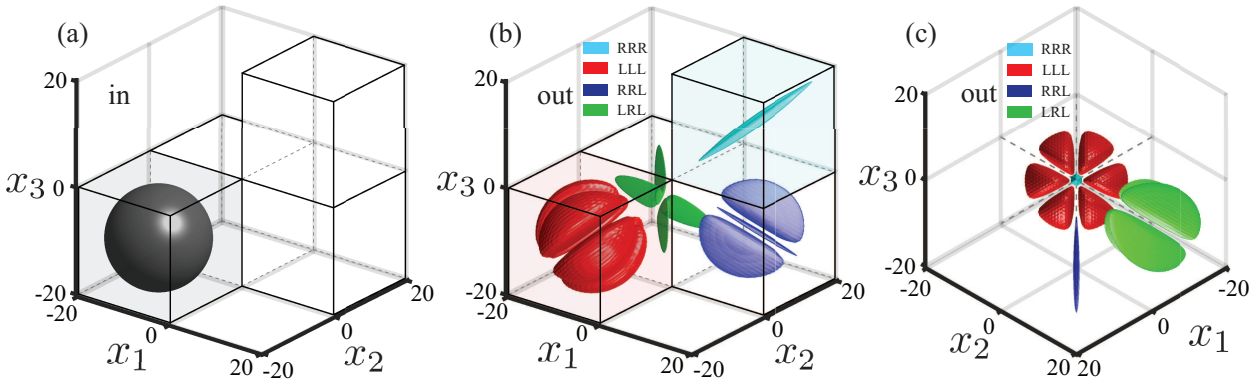

Figure 2.2: Three-photon wave function density plot in real space. (a) Incoming three-photon Gaussian pulse. Scattered state from the perspective of $x_1 = -x_2 = x_3$ in (b), and $x_1 = x_2 = x_3$ in (c). Density plots and axes are in units of Γ^3/v_g^3 and v_g/Γ, respectively.

object in Fig. 2.2(b)). Transversely, $|\phi_{RRR}|^2$ is restricted in an hexagonal area whose dimension is roughly the spatial size of the spontaneous emission process ($\approx v_g/\Gamma$, see Fig. 2.2(c)). That is, three transmitted photons are strongly collocated as they are indistinguishably interacting with the atom within one time window of spontaneous emission. Such a prominent collocated behavior may be direct evidence that three transmitted photons form a trimer.

For three reflected photons in the LLL branch, $|\phi_{LLL}|^2$ is represented by the red object in the octant of $x_1, x_2, x_3 < 0$. Its general envelope remains the same spherical profile as the incoming pulse while $|\phi_{LLL}|^2$ is depleted along three diagonal planes (*i.e.*, $x_1 = x_2$, $x_2 = x_3$, and $x_1 = x_3$). Three depletions lead to a six-lobed shape transversely in Fig. 2.2(c). Particularly, each depletion has a thickness $\approx v_g/\Gamma$, indicating that any two photons can not be reflected within one spontaneous emission time window. That is, three reflected photons are antibunched.

For one-transmitted-two-reflected photons in the LRL, RLL, and LLR branches, only $|\phi_{LRL}|^2$ is presented because the other two can be analyzed by invoking bosonic symmetry $\phi_{LRL}(x_1, x_2, x_3) = \phi_{RLL}(x_2, x_1, x_3) = \phi_{LLR}(x_1, x_3, x_2)$. Specifically, in octant of $x_1, x_3 < 0$, $x_2 > 0$, $|\phi_{LRL}|^2$ consists of two back-to-back seashell-shaped objects (green),

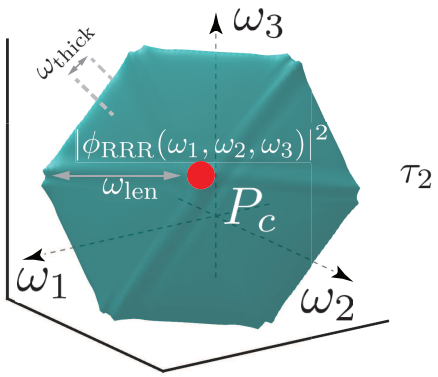

Figure 2.3: Frequency-space wave function density plot $|\phi_{RRR}(\omega_1,\omega_2,\omega_3)|^2$ in units of $1/\Gamma^3$. P_c (Ω,Ω,Ω) is the geometric center. ω_{len} and ω_{thick} denote the side length and thickness of the extended object at which the wave function decays to 0.015 of the maximal value (a suitable value for visualization).

which has two characteristics. First, $|\phi_{LRL}|^2$ is depleted along the plane $(x_1 = x_3)$ as two photons (position described by $x_{1,3}$) can not be reflected within one spontaneous emission window. Secondly, $|\phi_{LRL}|^2$ is restricted on $x_2 = -x_1 + 0.15v_g/\Gamma$ or $x_2 = -x_3 + 0.15v_g/\Gamma$ as the transmitted photon (position described by x_2) propagates $0.15v_g/\Gamma$ ahead of two reflected photons. Such a time lag can be accounted for that reflected photons undergo absorptions and spontaneous emissions while the transmitted photon does not. Similarly, for two-transmitted-one-reflected photons in the RRL, RLR, and LRR branches, only $|\phi_{RRL}|^2$ is analyzed. In octant of $x_1, x_2 > 0,\ x_3 < 0$, $|\phi_{RRL}|^2$ consists of a spindle-shaped object in the middle and two disconnected semicircle plates on the side (purple). Middle and side parts represent that transmitted photons interact with the atom within the same, and in different spontaneous emission window, respectively.

In addition to wave function density information, we further examine the phase shift to evaluate the acquired phase of scattering photons by using three freely-propagating photons as phase references. First, one obtains the reference phase information by invoking the condition that the atom is decoupled from the waveguide (*i.e.*, $\bar{V} = 0$), and then recording the reference wave function $\phi_{RRR,ref}(x_1, x_2, x_3, t_f)$ at a final time t_f. Secondly, one records

the scattered wave function $\phi_{RRR}(x_1, x_2, x_3, t_f)$ at the same final time t_f when the atom is coupled to the waveguide (*i.e.*, $\bar{V} \neq 0$). The phase shift, $\Delta(x_1, x_2, x_3)$, can be evaluated by $\Delta(x_1, x_2, x_3) = \arg[\phi_{RRR}(x_1, x_2, x_3, t_f)] - \arg[\phi_{RRR,ref}(x_1, x_2, x_3, t_f)]$ ($t_f \gg 1/\Gamma$). Remarkably, we observe a precise $\Delta = \pi$ phase (relative error $< 10^{-4}$) imprinted on the trimer (ϕ_{RRR}), which may facilitate designs of photon-based quantum logic gate.

We then examine the anti-correlation signature in frequency space. Specifically, by applying Fourier transform, $|\phi_{RRR}(\omega_1, \omega_2, \omega_3)|^2$ is plotted in Fig. 2.3. It resembles a hexagonal plate that leans against the plane described by $\omega_1 + \omega_2 + \omega_3 = E/\hbar$, to confirm the anti-correlation signature. Moreover, the plate is centered at P_c (Ω, Ω, Ω) with a side length $\omega_{\text{len}} \approx 2.79\Gamma$ and a thickness $\omega_{\text{thick}} \approx 3.46 v_g/\sigma$ (see caption for definitions of the extended object), determined by atom-photon interaction and incident photon bandwidths, respectively. By adopting frequency-space trimer wave function $\phi(\omega_1, \omega_2, \omega_3) = \sqrt{\frac{128}{3v_g}}\frac{\kappa^3}{\pi}\delta(\omega_1+\omega_2+\omega_3-\frac{E}{\hbar})\frac{(\omega_1-\frac{E}{3\hbar})^2+(\omega_1-\frac{E}{3\hbar})(\omega_2-\frac{E}{3\hbar})+(\omega_2-\frac{E}{3\hbar})^2+12\kappa^2}{[(\omega_1-\frac{E}{3\hbar})^2+4\kappa^2][(\omega_2-\frac{E}{3\hbar})^2+4\kappa^2][(\frac{2E}{3\hbar}-\omega_1-\omega_2)^2+4\kappa^2]}$ as a fitting metric, $\kappa \approx \Gamma/2$ is obtained.

2.4 Correlation Functions

The essential correlation signatures of transmitted (ϕ_{RRR}) and reflected (ϕ_{LLL}) photons are of practical interest, which are further compactly encoded in experimentally observable correlation function metrics, $g^{(3)}$ and $g^{(2)}$. Specifically, such metrics recast the wave function

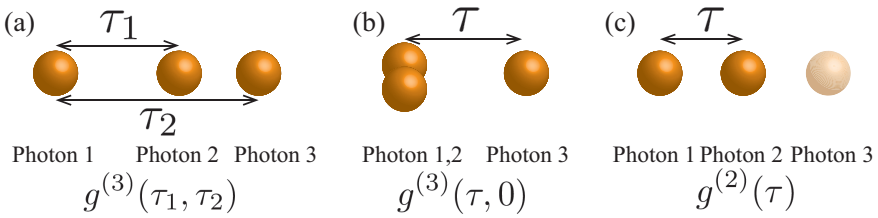

Figure 2.4: Illustration of correlation functions. (a) $g^{(3)}(\tau_1, \tau_2)$, (b) $g^{(3)}(\tau, 0)$, and (c) $g^{(2)}(\tau)$.

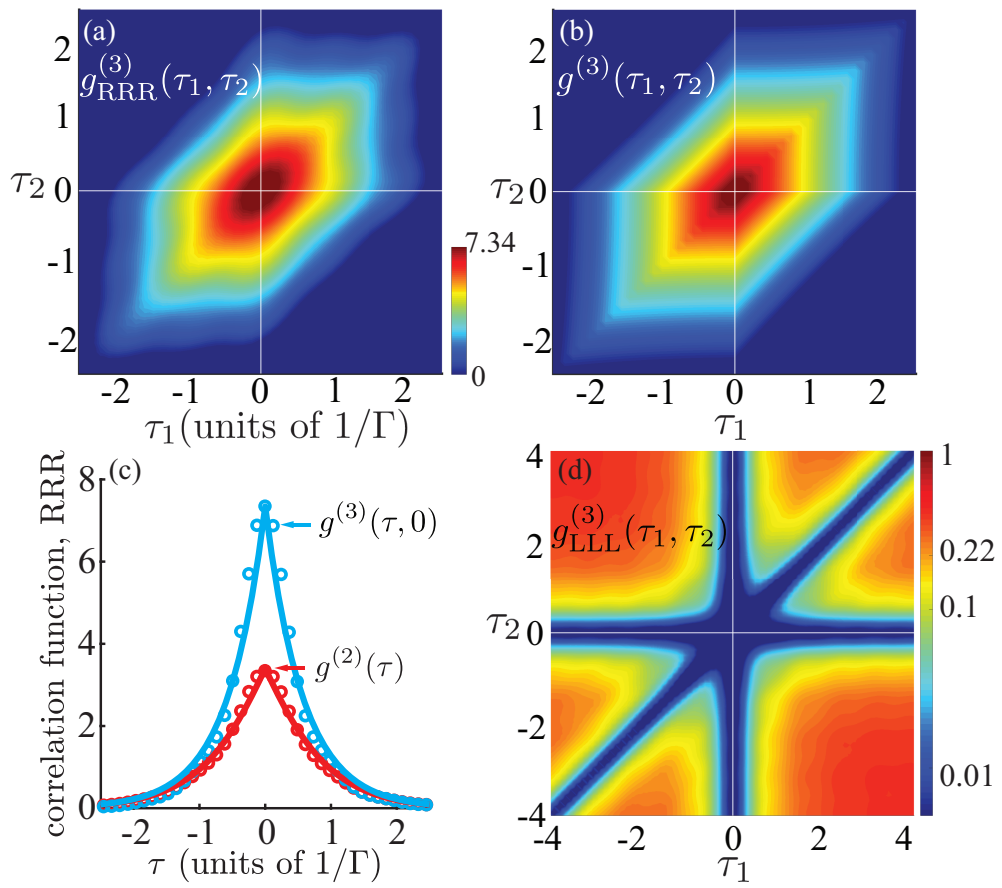

Figure 2.5: (a) Numerical result of $g^{(3)}(\tau_1,\tau_2)$ for ϕ_{RRR}. (b) Trimer correlation function $g^{(3)}(\tau_1,\tau_2) \propto e^{-2\kappa(|\tau_1|+|\tau_2|+|\tau_1-\tau_2|)}$ for $\kappa=\Gamma/2$ with the center value scaled by 7.34. (b) has the same colorbar as (a). (c) Numerical results of $g^{(3)}(\tau,0)$ (blue) and $g^{(2)}(\tau)$ (red) for ϕ_{RRR}. Curves and dots denote numerical and fitting results, respectively. (d) $g^{(3)}(\tau_1,\tau_2)$ for ϕ_{LLL}.

to the joint probability for the following photon coincident measurement: $g^{(3)}(\tau_1,\tau_2)$, detect a second and a third photon after τ_1 and τ_2 units of time of detecting a first photon, respectively (Fig. 2.4(a)); $g^{(3)}(\tau,0)$, detect a third photon after τ units of time of detecting two coincident photons (Fig. 2.4(b)); and $g^{(2)}(\tau)$, detect a second photon after τ units of time of detecting a first photon while information of the rest photon is not of interest and traced over (Fig. 2.4(c)).

For a trimer, its functional form is defined by $\phi(x_1,x_2,x_3)=\sqrt{\frac{4\kappa^2}{3\pi v_g^2}}e^{i\frac{E}{3\hbar v_g}(x_1+x_2+x_3)}e^{-\frac{\kappa}{v_g}(|x_1-x_2|+|x_1-x_3|+|x_2-x_3|)}$, where $1/\kappa$ denotes the temporal correlation width. By applying real-space formalisms of

trimer [21], it can be shown that

$$
\begin{aligned}
&g^{(3)}(\tau_1,\tau_2) \propto e^{-2\kappa(|\tau_1|+|\tau_2|+|\tau_1-\tau_2|)},\ g^{(3)}(\tau,0) \propto e^{-4\kappa|\tau|},\\
&g^{(2)}(\tau) \propto e^{-4\kappa(|\tau|)}(|\tau|+\frac{1}{2\kappa}),
\end{aligned}
\tag{2.5}
$$

which are used to confirm the collocated signature of ϕ_{RRR}. Figure 2.5(a) plots the numerically obtained $g^{(3)}(\tau_1,\tau_2)$, which resembles a hexagon that is elongated along $\tau_1=\tau_2$ while squeezed in the transversal direction. A peak shows up at the origin, *i.e.*, $g^{(3)}(0,0)\approx 7.34$, which states that the joint probability to detect three collocated photons is thirty-three times as large as detecting them independently (compared with $g^{(3)}(0,0)=2/9$ in the uncorrelated scenario). The full-width-at-half-maximum (FWHM) is roughly $1/\Gamma$, indicating that three photons get transmitted within the same spontaneous emission window. By exploiting $g^{(3)}(\tau_1,\tau_2)$ in Eq. (2.5) as fitting metrics, one obtains $\kappa\approx\Gamma/2$ with a good coincidence. Figure 2.5(b) plots the $g^{(3)}(\tau_1,\tau_2)$ of $\kappa=\Gamma/2$ as a benchmark of the correlation signature of trimer.

Figure 2.5(c) plots $g^{(3)}(\tau,0)$ and $g^{(2)}(\tau)$, both of which exhibit a cusp around $\tau=0$ and monotonically decrease as $|\tau|$ increases. Such cusps are fingerprints of a trimer because both metrics are asymptotically described by $e^{-4\kappa|\tau|}$ as $\tau\to 0$. $g^{(2)}(0)\approx 3.34$, which implies that the joint probability to detect two photons together is five times as large as that to detect them independently (compared with $g^{(2)}(0)=2/3$ in the uncorrelated scenario). Notably, FWHM of $g^{(3)}(\tau,0)$ is $0.88/\Gamma$, which is smaller than that of $g^{(2)}(\tau)$, $1.14/\Gamma$, implying that one photon is correlated more strongly to other two photons collectively than to one of them solely. To quantify the correlation signature, we apply $g^{(3)}(\tau,0)$ and $g^{(2)}(\tau)$ in Eq. (2.5) to fit the results, both of which yield approximately $\kappa\approx\Gamma/2$.

For three reflected photons, $g^{(3)}_{LLL}$ (Fig. 2.5(d)) is depleted along two axes ($\tau_{1,2}=0$) and diagonal line ($\tau_1=\tau_2$), indicating an essentially vanishing probability to detect any two

collocated photons to confirm photon antibunching ($g^{(3)}(0,0) \approx 1.37 \times 10^{-4} \ll 2/9$ for uncorrelated state $|3\rangle$).

2.5 Theoretical Explanation

So far, we have confirmed that ϕ_{RRR} manifests as a trimer of $\kappa \approx \Gamma/2$. Note that the three-photon bound state (wave function $\propto e^{iE(x_1+x_2+x_3)/3\hbar v_g - \Gamma(|x_1-x_2|+|x_1-x_3|+|x_2-x_3|)/v_g}$ for a particular system in Fig. 2.1) is a trimer of $\kappa = \Gamma$. Consequently, ϕ_{RRR} does not result from the bound state contribution solely.

Here we present a physical argument that, in the resonant narrow-bandwidth case, the hybrid state contributes a trimer of $\kappa = \Gamma/2$. Particularly, the hybrid state is a product state of dimer and an unbounded single photon. It can be shown that, in the even mode, for the hybrid state (see functional form in Eq. (15) in Ref. [21]), when the energy of unbounded single photon is resonant with the average energy of the dimer, the hybrid state $|H\rangle_{e^{(3)}}$ manifests as a $\Gamma/2$ trimer and a direct-product basis of dimer and single photon as follows

$$|H\rangle_{e^{(3)}} = \beta_1 |B_{\frac{\Gamma}{2}}\rangle_{e^{(3)}} + \beta_2 |B_\Gamma\rangle_{e^{(2)}} |P\rangle_{e^{(1)}}, \tag{2.6}$$

where $\beta_1 = \sqrt{\frac{3v_g}{2\pi\Gamma}}$ and $\beta_2 = -1$. The subscript of $e^{(n)}$ represents a n-photon Hilbert space in the even mode ($n = 1, 2, 3$). $|B_{\frac{\Gamma}{2}}\rangle_{e^{(3)}}$ is a trimer state of $\kappa = \Gamma/2$ and $|B_\Gamma\rangle_{e^{(2)}}$ is a dimer state of $\kappa = \Gamma$. An incident state $|\chi_{\text{in}}\rangle$ can be decomposed into a linear superposition of orthogonal three-photon sub-Hilbert space $e^{(k)}o^{(3-k)}$, where k photons in the even mode and remaining $3-k$ photons in the odd mode ($k = 0, 1, \cdots, 3$), *i.e.*, $|\chi_{\text{in}}\rangle = |\chi_{\text{in}}\rangle_{e^{(3)}} + |\chi_{\text{in}}\rangle_{e^{(2)}o^{(1)}} + \cdots$. To obtain the information of the out-state $|\chi_{\text{out}}\rangle = \mathbf{S}|\chi_{\text{in}}\rangle$ ($\mathbf{S}$ is the scattering matrix), we now need to project the in-state to all eigen-states in three-photon Hilbert space. Notably, only four states may affect photon correlation information, those are, state 1, trimer state

of $\kappa = \Gamma$, $|B_\Gamma\rangle_{e^{(3)}}$; state 2, hybrid state contributions of $\beta_1|B_{\frac{\Gamma}{2}}\rangle_{e^{(3)}}$; state 3, hybrid state contributions of $\beta_2|B_\Gamma\rangle_{e^{(2)}}|P\rangle_{e^{(1)}}$; and state 4, direct-product basis of even-mode dimer and odd-mode single photon, $|B_\Gamma\rangle_{e^{(2)}}|P\rangle_{o^{(1)}}$.

Here we show that the RRR branch is a mixture of trimer of $\kappa = \Gamma/2$ (state 2) and trimer of $\kappa = \Gamma$ (state 1) because states 3 and 4 destructively interfere to be canceled out. To begin with, the in-state can be projected onto eigenstates (of particular interest is the projection onto states 3 and 4 as explicitly shown in the following)

$$|\chi_{\text{in}}\rangle = \beta_2^*\langle B_\Gamma|_{e^{(2)}}\langle P|_{e^{(1)}}|\chi_{\text{in}}\rangle_{e^{(3)}}\beta_2|B_\Gamma\rangle_{e^{(2)}}|P\rangle_{e^{(1)}} + \langle B_\Gamma|_{e^{(2)}}\langle P|_{o^{(1)}}|\chi_{\text{in}}\rangle_{e^{(3)}}|B_\Gamma\rangle_{e^{(2)}}|P\rangle_{o^{(1)}} + \cdots . \tag{2.7}$$

By applying S-matrix to map the in-state to the out-state, it follows that

$$\begin{aligned}
|\chi_{\text{out}}\rangle =& \mathbf{S}|\chi_{\text{in}}\rangle \\
=& |\beta_2|^2\langle B_\Gamma|_{e^{(2)}}\langle P|_{e^{(1)}}|\chi_{\text{in}}\rangle_{e^{(3)}}\mathbf{S}|B_\Gamma\rangle_{e^{(2)}}|P\rangle_{e^{(1)}} + \langle B_\Gamma|_{e^{(2)}}\langle P|_{o^{(1)}}|\chi_{\text{in}}\rangle_{e^{(2)}o^{(1)}}\mathbf{S}|B_\Gamma\rangle_{e^{(2)}}|P\rangle_{o^{(1)}} + \cdots \\
=& \langle B_\Gamma|_{e^{(2)}}\langle P|_{e^{(1)}}|\chi_{\text{in}}\rangle_{e^{(3)}}|B_\Gamma\rangle_{e^{(2)}}|P\rangle_{e^{(1)}} - \langle B_\Gamma|_{e^{(2)}}\langle P|_{o^{(1)}}|\chi_{\text{in}}\rangle_{e^{(2)}o^{(1)}}|B_\Gamma\rangle_{e^{(2)}}|P\rangle_{o^{(1)}} + \cdots \\
=& c(|B_\Gamma\rangle_{e^{(2)}}|P\rangle_{e^{(1)}} - |B_\Gamma\rangle_{e^{(2)}}|P\rangle_{o^{(1)}}),
\end{aligned} \tag{2.8}$$

where we have used $\mathbf{S}|B_\Gamma\rangle_{e^{(2)}}|P\rangle_{e^{(1)}} = |B_\Gamma\rangle_{e^{(2)}}|P\rangle_{e^{(1)}}$, $\mathbf{S}|B_\Gamma\rangle_{e^{(2)}}|P\rangle_{o^{(1)}} = -|B_\Gamma\rangle_{e^{(2)}}|P\rangle_{o^{(1)}}$, and $|\beta_2|^2\langle B_\Gamma|_{e^{(2)}}\langle P|_{e^{(1)}}|\chi_{\text{in}}\rangle_{e^{(3)}}|B_\Gamma\rangle_{e^{(2)}}|P\rangle_{e^{(1)}} = \langle B_\Gamma|_{e^{(2)}}\langle P|_{o^{(1)}}|\chi_{\text{in}}\rangle_{e^{(2)}o^{(1)}}$. Then by transforming the even/odd mode back to the right/left mode via $c_e^\dagger(x) = \frac{1}{\sqrt{2}}(c_R^\dagger(x) + c_L^\dagger(-x)), c_o^\dagger(x) = \frac{1}{\sqrt{2}}(c_R^\dagger(x) - c_L^\dagger(-x))$, it can be shown that, in the RRR branch, contributions from states 3 and 4 cancel out. As a result, the RRR branch is a mixture of trimer of $\kappa = \Gamma/2$ and trimer of $\kappa = \Gamma$ with their weights determined by the hybrid and trimer weights, respectively. From Table V in Ref. [21], it is speculated that for a long Gaussian wave, the hybrid state component dominates over that from the trimer state. Consequently, the RRR branch manifests as a trimer state of $\kappa \approx \Gamma/2$.

2.6 Weak-coherent Input

Table 2.1: $g^{(2)}$ and $g^{(3)}$ metrics for dimer and trimer, forward scattered light of incoming Fock states $|2\rangle$, $|3\rangle$, and weak-coherent state $|\alpha\rangle$.

State	$g^{(2)}(\tau)$	$g^{(3)}(\tau_1, \tau_2)$
dimer	$e^{-2\kappa\|\tau\|}$	0
trimer	$e^{-4\kappa\|\tau\|}(\frac{1}{2\kappa} + \|\tau\|)$	$e^{-2\kappa(\|\tau_1\|+\|\tau_2\|+\|\tau_1-\tau_2\|)}$
$\|2\rangle$	$e^{-2\Gamma\|\tau\|}$	0
$\|3\rangle$	$\approx e^{-2\Gamma\|\tau\|}(\frac{1}{\Gamma} + \|\tau\|)$	$\approx e^{-\Gamma(\|\tau_1\|+\|\tau_2\|+\|\tau_1-\tau_2\|)}$
$\|\alpha\rangle$	$e^{-2\Gamma\|\tau\|}$	$\approx e^{-\Gamma(\|\tau_1\|+\|\tau_2\|+\|\tau_1-\tau_2\|)}$

In practice, instead of a genuine Fock state input, an alternative weak-coherent input that consists of linear superpositions of truncated Fock states, $|\alpha\rangle \propto \sum_{n=0}^{N} e^{-\frac{|\alpha|^2}{2}} \frac{\alpha^n}{\sqrt{n!}} |n\rangle$, is typically adopted, *e.g.,* $N = 3$ in cold atomic gas [53] and $N = 6$ on solid state platform [61]. Due to the linearity of Schrödinger equation in terms of different Fock state sectors, and a small average photon number ($|\alpha|^2 \ll 1$), $g^{(2)}$ and $g^{(3)}$ of scattered photon field for incident $|\alpha\rangle$ are determined by its $|2\rangle$ and $|3\rangle$ Fock state scattering process, respectively [39]. Note that for resonantly incident $|2\rangle$ and $|3\rangle$ states, transmitted photons form a dimer of $\kappa = \Gamma$ [20] and a trimer of $\kappa \approx \Gamma/2$, respectively, whose correlation metrics are summarized in Table 2.1. As a result, in the practical 3D geometry, considering that forward scattered light can be mapped into transmitted photon field in the presented 1D geometry [39], $g^{(2)}$ and $g^{(3)}$ of transmitted photons for incident $|2\rangle$, $|3\rangle$, and $|\alpha\rangle$ states are derived in Table 2.1.

2.7 Experimental Validation

Finally, we apply our formalism to study photon correlations for a recent experiment [53]. Specifically, a weak coherent probe is coupled to a highly-excited Rydberg atomic state, through a strong control laser (Rabi frequency $\Omega_c = 2\pi \times 10\text{MHz}$) coupled to an intermediate

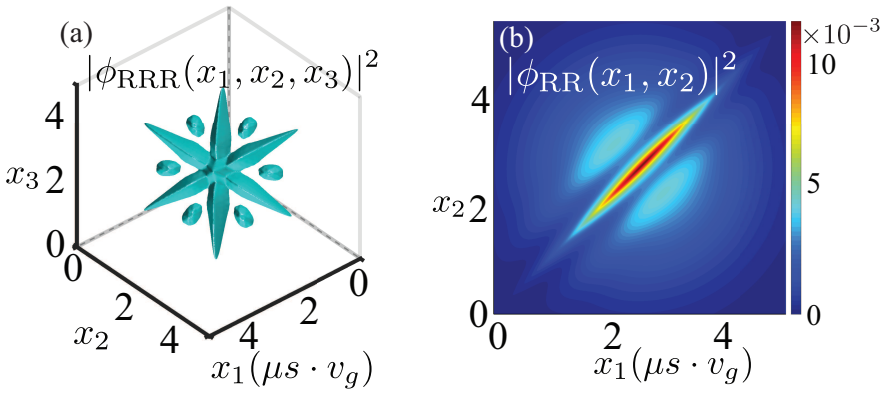

Figure 2.6: Photonic Correlations of forward scattered light for a weak-coherent input $|\alpha\rangle$ under experimental condition [53]. Transmitted (a) three- and (b) two- photon wave functions. Density plots are in units of Γ^3/v_g^3 in (a) and Γ^2/v_g^2 in (b).

state. Here we argue that the experimental geometry is effectively one-dimensional because the beam waist ($\approx 4.5\mu m$) is much smaller than the Rydberg blockade diameter ($\approx 40\mu m$) so that the photons can not travel side by side to walk around the blockade. It can be shown that, in the dispersive regime (probe detuning $\Delta_p = 2\pi \times 30$MHz much larger than intermediate state linewidth $2\gamma_o = 2\pi \times 6.1$MHz), the intermediate state can be adiabatically eliminated so that the three-level ladder system is mapped to an effective two-level system (Fig. 2.1) of detuning $\delta = -\Omega_c^2\Delta_p/4(\Delta_p^2+\gamma_o^2)$ and dissipation rate $\gamma = \Omega_c^2\gamma_o/4(\Delta_p^2+\gamma_o^2)$ (see Appendix B). Furthermore, by adopting optical depth per blockade $OD_B \approx 5.3$ in a one-way setup (omitting $c_L^\dagger$ in Eq. (2.1) due to insignificant backscattered light in the dispersive regime) [62], we send in uncorrelated states $|2\rangle$ and $|3\rangle$, both of which have a long Gaussian profile (temporal duration $6.8\mu s \gg$ spontaneous lifetime $0.23\mu s$). After scattering, we investigate wave functions, correlation functions, and conditional phases of forward scattered photons. For incoming $|3\rangle$ state, Fig. 2.6(a) plots the transmitted three-photon wave function, which has a C_6 symmetry and exhibits a center diagonal-line part, six side-lobes, and six disconnected dots, representing three-photon bound, hybrid, and unbounded states, respectively. For incoming $|2\rangle$ state, Fig. 2.6(b) plots transmitted two-photon wave function, which exhibits a diagonal-line part and two side-lobes to represent two-photon bound and unbounded states, respectively.

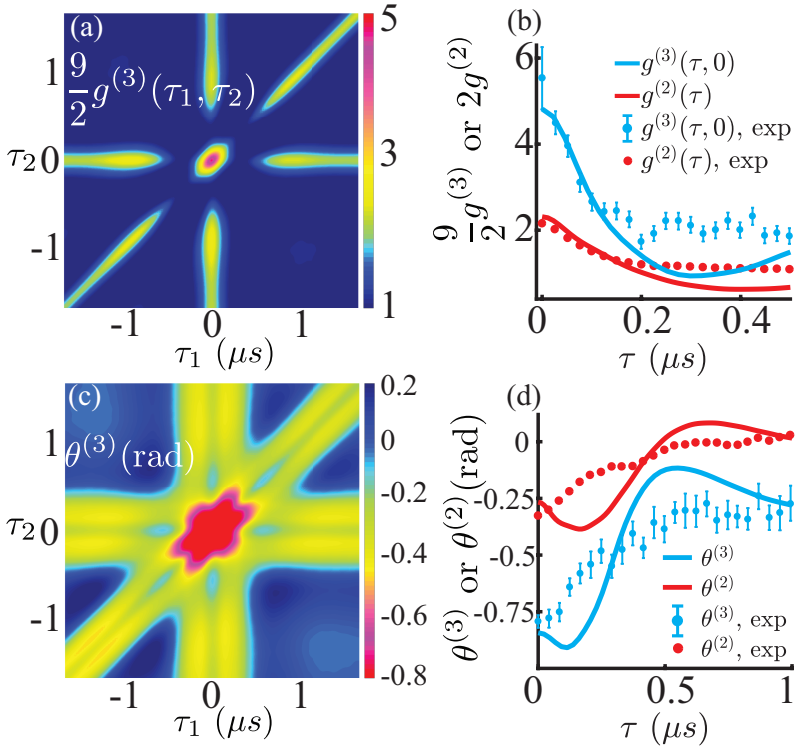

Figure 2.7: Photonic Correlations of forward scattered light for a weak-coherent input $|\alpha\rangle$ under experimental condition [53]. (a) $\frac{9}{2}g^{(3)}(\tau_1,\tau_2)$. (b) $\frac{9}{2}g^{(3)}(\tau,0)$ and $2g^{(2)}(\tau)$. (c) $\theta^{(3)}(x_m, x_m+v_g\tau_1, x_m+v_g\tau_2)$. $x_m = 4.38\sigma$ is a reference point that is irrelevant to results. (d) $\theta^{(3)}(x_m, x_m, x_m+v_g\tau)$ and $\theta^{(2)}(x_m, x_m+v_g\tau)$. Experimental data in (c) and (d) are adapted from Fig. 2B and 3B in Ref. [53], respectively.

To validate our formalism, we compare numerically obtained correlation functions and conditional phases with experimental results: $\frac{9}{2}g^{(3)}$, $\theta^{(3)}$ for $|3\rangle$ scattering; and $2g^{(2)}$, $\theta^{(2)}$ (two-photon conditional phase, defined similar to $\theta^{(3)}$) for $|2\rangle$ scattering (note that experimental measured correlation functions for weak-coherent inputs are normalized to $\frac{9}{2}g^{(3)}$ for $|3\rangle$ and $2g^{(2)}$ for $|2\rangle$ [39]). Figure 2.7(a) plots $\frac{9}{2}g^{(3)}$, which exhibits a center hexagon, on-axis diagonal strips, and off-axis off-diagonal background to represent bound, hybrid, and unbounded state contributions, respectively. Apparently, Fig. 2.7(c) agrees well with Fig. 2A in Ref. [53]. Figure 2.7(b) plots numerically obtained $\frac{9}{2}g^{(3)}(\tau,0)$ (blue curve) and $2g^{(2)}(\tau)$ (red curve), where $\frac{9}{2}g^{(3)}(0,0)\approx 5$ and $2g^{(2)}(0)\approx 2$ are consistent with experiments. The full-width-at-$1/e$ of $g^{(3)}$ is half of that of $g^{(2)}$, which is also confirmed in experiments. Notably, numerical results (curves) are slightly inconsistent with experimental ones (dots) due to the multiple Rydberg blockade effect in practice. Specifically, experimentally measured correlation functions may contain the information of uncorrelated photons interacting with different Rydberg blockade so that correlation functions flatten out in contrast to predictions from our single-atom model. $\theta^{(3)}$ in Fig. 2.7(c) echoes Fig. 2.7(a) to indicate different conditional phases due to different state contributions, which agrees with Fig. 3A in Ref. [53]. Figure 2.7(d) plots both numerical (curves) and experimental (dots) results of $\theta^{(3)}$ and $\theta^{(2)}$. Quantitatively, $\theta^{(3)}|_{\tau=0}\approx -0.84$ rad, and $\theta^{(2)}|_{\tau=0}\approx -0.27$ rad agree with experiment results, and can be approximated using first-principle results in Ref. [20, 21]. For instance, $\theta^{(2)}|_{\tau=0}$ can be approximated by the angle of two-photon bound state transmission amplitude $t_B^{(2)}$ substracted by that of single-photon transmission amplitude $t^{(1)}$, *i.e.*, $\theta^{(2)}|_{\tau=0}\approx \arg t_B^{(2)} - 2\arg t^{(1)}$. Due to the aforementioned multiple Rydberg blockade effect, dips at $\tau\approx 0.1\mu s$ and overshootings at $\tau\approx 0.5\mu s$ predicted from our formalism are smeared out in experimental observations.

2.8 Summary and Outlook

In this chapter, we present a computational study of coherent three-photon scattering off a single two-level atom in waveguide QED systems. Our results confirm the trimer signatures by examining the wave function representations and correlation function metrics. Moreover, we show that the correlation metrics obtained from the three- and two- photon Fock state scattering also apply to a weak-coherent input, and describe well the recent experimental discovery of photonic trimers.

Our work opens up a new research direction of computational study for correlated three-photon scattering and transport, which may be generalized to more complicated waveguide QED architectures [63–65]. Exotic photonic trimer state may tremendously enhance three-photon fluorescence efficiency due to collocated behavior and anti-correlation properties [66, 67]. Observed strong antibunching statistics can be exploited to realize faithful single-photon source for secure quantum communication protocol [68–70]. Moreover, the imprinted π phase shift may be exploited to implement deterministic quantum logic gates for universal quantum computing.

Chapter 3

Correlated Multi-photon Dissipation Theory: Scattering Loss

3.1 Introduction

Dissipations are ubiquitous in any physical system. However, from a perspective of the global universe (Fig. 3.1), there are no dissipations because particle and energy are conserved globally. Every process is coherent and reversible, which is described by a Hermitian Hamiltonian. Nonetheless, only the degrees of freedom nearby are of interest that are referred to as the system of interest while all other degrees of freedom are treated as the external reservoir. Due to inevitable coupling between them, photons may leak out of the system to the reservoir, thereby manifesting as irreversible dissipations. The reservoir, in general, can be characterized into two different types of nature. On one hand, the reservoir can be non-excitable and is modeled as photonic scattering channels [71]. The model describes the photon leakages out of the QED system of interest as photonic scattering loss. On the other hand, the reservoir

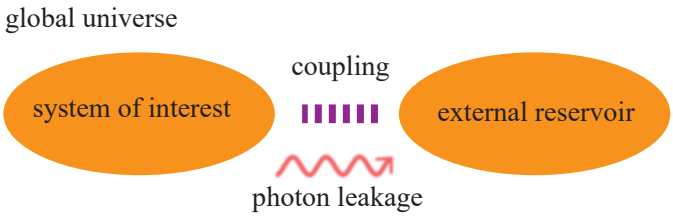

Figure 3.1: Illustration of the emerging concept of dissipations from a perspective of global universe. Due to the coupling between the system of interest and the external reservoir, the photon leakages manifest as dissipations.

can be excitable, which contains infinitely many excitation oscillators to be discussed in next chapter. In the presence of dissipation, the dynamics of the system is typically described by a reduced non-Hermitian Hamiltonian (*i.e.*, adding an imaginary part in the atomic transition frequency) and a reduced eigenstate (*i.e.*, omitting the scattering channels of the reservoir in the wave function) which are restricted to the Hilbert space of interest only [72]. It is not clear, *a priori*, whether the correlated multi-photon transport properties can still be described by the non-Hermitian Hamiltonian.

In this chapter, we develop a correlated multi-photon dissipation theory to describe the photonic scattering loss for an arbitrary Fock state process. The presented approach preserves the system-reservoir entanglement throughout the procedure, which does not rely on any uncontrolled approximations. By examining equations of motion and restricted scattering matrix, we rigorously validate the non-Hermitian Hamiltonian description for single-, two-, and an arbitrary N-photon Fock state process.

3.2 Model and Hamiltonian

Figure 3.2 schematically shows a general waveguide QED system in a non-excitable reservoir. An N-photon Fock state $|N\rangle$ is launched from the left and interacts with the atom. Each photon can escape the waveguide to the reservoir or remain waveguided. The reservoir is

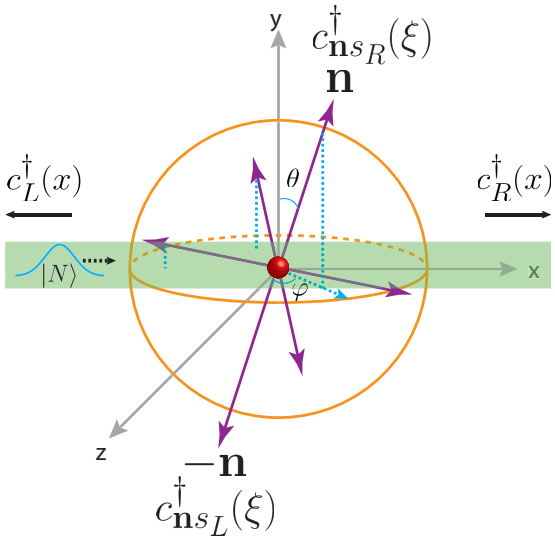

Figure 3.2: Schematic of the dissipation model of scattering channels (indicated by purple lines) in a waveguide QED system. A two-level atom (transition frequency $\Omega = \omega_e - \omega_g$) is side-coupled to a single-mode waveguide (along the x-axis). The atom sits at the origin. $\mathbf{n} = (\sin\theta\sin\varphi, \cos\theta, \sin\theta\cos\varphi)$ is the direction of the scattering channel. The orientation within $\mathbf{n}$ is further specified by $\mathbf{n}_R = \mathbf{n}$ and $\mathbf{n}_L = -\mathbf{n}$. s denotes the polarization. $\theta \in [0, \pi)$ and $\varphi \in [0, \pi)$.

characterized by infinitely many three-dimensional scattering channels, each of which is uniquely specified by the direction of photon momentum, $\mathbf{n}$, and the polarization, s. The infinitely many degrees of freedom of the scattering channels give rise to an irreversible process macroscopically. To begin with, we first discretize the photonic phase space as follows: the polar angle, θ, and the azimuthal angle, φ, are discretized uniformly so that now each scattering channel is uniquely specified by a doublet $\{\theta_i, \varphi_j\} = \{\frac{\pi}{M_1}i, \frac{\pi}{M_2}j\}$, where $i = 0, 1, \cdots, M_1$; $j = 0, 1, \cdots, M_2$; and $\sum_{\mathbf{n}} = \sum_{i,j} M_1 M_2 \Delta\theta_i \Delta\varphi_j/\pi^2$. The system Hamiltonian is described by

$$\begin{aligned}\frac{H_S}{\hbar} = &\int dx \left[c_R^\dagger(x)(-iv_g\partial_x)c_R(x) + c_L^\dagger(x)(iv_g\partial_x)c_L(x)\right] \\ &+ \int dx \bar{V}\delta(x)\left[c_R^\dagger(x)\sigma_- + \sigma_+ c_R(x) + c_L^\dagger(x)\sigma_- + \sigma_+ c_L(x)\right] + \omega_e a_e^\dagger a_e + \omega_g a_g^\dagger a_g,\end{aligned} \tag{3.1}$$

where notations are defined the same as in Eq. (2.1). Notably, $\bar{V} \propto -\vec{d} \cdot E(\vec{x}_a)$ denotes the atom-waveguide coupling strength, encoding the angular information of guided-mode polarizations, atomic quantization axes, and atomic states ($\vec{d}$ is the atomic dipole moment, $\vec{E}$ is the electric field, and x_a is the atomic location, which is taken to be the origin in our configuration). The coupling varies inside the waveguide, but is uniquely determined once the atom location is fixed. The Hamiltonian of the reservoir scattering channels, H_C, is [71]

$$\frac{H_C}{\hbar} = \sum_{\mathbf{n},s} \int d\xi \Big[c^\dagger_{\mathbf{n}s_R}(\xi)(-iv\partial_\xi) c_{\mathbf{n}s_R}(\xi) + c^\dagger_{\mathbf{n}s_L}(\xi)(iv\partial_\xi) c_{\mathbf{n}s_L}(\xi) \Big], \tag{3.2}$$

where $c^\dagger_{\mathbf{n}s_R}$ denotes the creation operator of the right-moving photon of the $\mathbf{n}s$ channel, and $c^\dagger_{\mathbf{n}s_L}$ is analogously defined. v is the speed of light in the homogeneous environment. Here, the coordinate variables x and ξ are used for the waveguided and channel modes, respectively. The system-reservoir coupling is characterized by the Hamiltonian, H_{SC},

$$\frac{H_{SC}}{\hbar} = \sum_{\mathbf{n},s} \int d\xi \bar{V}_{\mathbf{n}s} \delta(\xi) \Big[c^\dagger_{\mathbf{n}s_R}(\xi)\sigma_- + \sigma_+ c_{\mathbf{n}s_R}(\xi) + c^\dagger_{\mathbf{n}s_L}(\xi)\sigma_- + \sigma_+ c_{\mathbf{n}s_L}(\xi) \Big], \tag{3.3}$$

where $\bar{V}_{\mathbf{n}s}$ denotes the coupling strength between the atom and the channel $\mathbf{n}s$. The complete Hamiltonian is given by $H = H_S + H_C + H_{SC}$.

3.3 Single-photon Case

In the single-photon case, the general state involving both the system and the reservoir is given by

$$|\Phi_1\rangle = \Big(\int dx \Big[\phi_R(x) c^\dagger_R(x) + \phi_L(x) c^\dagger_L(x) \Big] + e\sigma_+ + \sum_{\mathbf{n},s} \int d\xi \left[\phi_{\mathbf{n}s_R}(\xi) c^\dagger_{\mathbf{n}s_R}(\xi) + \phi_{\mathbf{n}s_L}(\xi) c^\dagger_{\mathbf{n}s_L}(\xi) \right] \Big) |\varnothing\rangle, \tag{3.4}$$

where ϕ_R denotes the single-photon wave function for the right-moving waveguided photon, and ϕ_L, $\phi_{\mathbf{n}s_R}$, and $\phi_{\mathbf{n}s_L}$ can be analogously defined. e is the atomic excitation amplitude. $|\varnothing\rangle$ is the photonic vaccum state with the atom at the ground state. By imposing the condition $H|\Phi_1\rangle = \hbar\epsilon|\Phi_1\rangle$ ($\hbar\epsilon$ is the eigen-energy of the combined system), we obtain the equations of motion

$$\epsilon\phi_R(x) = -iv_g\partial_x\phi_R(x) + \bar{V}\delta(x)e + \omega_g\phi_R(x), \tag{3.5a}$$

$$\epsilon\phi_L(x) = iv_g\partial_x\phi_L(x) + \bar{V}\delta(x)e + \omega_g\phi_L(x), \tag{3.5b}$$

$$\epsilon\phi_{\mathbf{n}s_R}(\xi) = -iv\partial_\xi\phi_{\mathbf{n}s_R}(\xi) + \bar{V}_{\mathbf{n}s}\delta(\xi)e + \omega_g\phi_{\mathbf{n}s_R}(\xi), \tag{3.5c}$$

$$\epsilon\phi_{\mathbf{n}s_L}(\xi) = iv\partial_\xi\phi_{\mathbf{n}s_L}(\xi) + \bar{V}_{\mathbf{n}s}\delta(\xi)e + \omega_g\phi_{\mathbf{n}s_L}(\xi), \tag{3.5d}$$

$$\epsilon e = \omega_e e + \bar{V}\left[\phi_R(0) + \phi_L(0)\right] + \sum_{\mathbf{n},s}\bar{V}_{\mathbf{n}s}\left[\phi_{\mathbf{n}s_R}(0) + \phi_{\mathbf{n}s_L}(0)\right]. \tag{3.5e}$$

We note that Eqs. (3.5a) and (3.5b) involve only the variables of the system while Eqs. (3.5c) and (3.5d) involve variables of the reservoir. Both sets are coupled by Eq. (3.5e), which involves the photonic wave function at the atom location.

By expressing $\phi_{\mathbf{n}s_R}(0)$ and $\phi_{\mathbf{n}s_L}(0)$ in terms of e, Eqs. (3.5a), (3.5b), and (3.5e) become self-consistent involving only the system variables. As the photon is initially injected into the waveguide and is scattered into the channels by the atom, the single-photon wave function in the scattering channel, $\phi_{\mathbf{n}s_R}$ and $\phi_{\mathbf{n}s_L}$, must take the forms of $\phi_{\mathbf{n}s_R}(\xi) = p_{\mathbf{n}s}\theta(\xi)e^{ik\xi}$, and $\phi_{\mathbf{n}s_L}(\xi) = q_{\mathbf{n}s}\theta(-\xi)e^{-ik\xi}$ where θ is Heaviside function. One now plugs $\phi_{\mathbf{n}s_R}$ and $\phi_{\mathbf{n}s_L}$ into Eqs. (3.5c) and (3.5d) to obtain $p_{\mathbf{n}s} = q_{\mathbf{n}s} = -i\frac{\bar{V}_{\mathbf{n}s}}{v}e$. One also has that $\phi_{\mathbf{n}s_R}(0) = p_{\mathbf{n}s}/2, \phi_{\mathbf{n}s_L}(0) = q_{\mathbf{n}s}/2$, where we have employed $\theta(0) = 1/2$. Thus, Eq. (3.5e) now reads as

$$\epsilon e = (\omega_e - i\sum_{\mathbf{n},s}\frac{\bar{V}_{\mathbf{n}s}^2}{v})e + \bar{V}\left[\phi_R(0) + \phi_L(0)\right], \tag{3.6}$$

which now does not involve the wave functions of the scattering channels. Eqs. (3.5a), (3.5b), and (3.6) now form a set of self-consistent equations which only involve the system variables ϕ_R, ϕ_L, and e. Eq. (3.6) states that such an approach is equivalent to adding an imaginary part $-i\gamma_S$ to ω_e in H_S, where $\gamma_S = \sum_{\mathbf{n},s} \bar{V}^2_{\mathbf{n}s}/v$ is identified as the atomic dissipation rate due to scattering loss. This set of self-consistent equations can be derived from a reduced non-Hermitian Hamiltonian and a restricted eigen-state ($|\Phi_1\rangle = (\int dx \left[\phi_R(x)c_R^\dagger(x) + \phi_L(x)c_L^\dagger(x)\right] + e\sigma_+)|\varnothing\rangle$) that only involves the variables of the system. The dissipative process is described by the added imaginary part $-i\gamma_S$.

3.4 Multi-photon Case

3.4.1 Two-photon Case

We now generalize the approach for the two-photon case. To facilitate the mathematical description, we transform H to the even (H_e) and odd (H_o) modes ($H = H_e + H_o$) such that H_e and H_o are decoupled ($[H_e, H_o] = 0$, see Ref. [20]). Since the photon-atom interaction is present in the even mode, but not in the odd one, only the even mode is taken into account from now on. H_e takes the following form,

$$\begin{aligned}\frac{H_e}{\hbar} = &\int dx c_e^\dagger(x)(-iv_g\partial_x)c_e(x) + \int dx V\delta(x)\left[c_e^\dagger(x)\sigma_- + \sigma_+ c_e(x)\right] \\ &+ \sum_{\mathbf{n},s}\left(\int d\xi c^\dagger_{\mathbf{n}s_e}(\xi)(-iv\partial_\xi)c_{\mathbf{n}s_e}(\xi)\right) + \omega_e a_e^\dagger a_e + \omega_g a_g^\dagger a_g + \sum_{\mathbf{n},s}\int d\xi V_{\mathbf{n}s}\delta(\xi)\left[c^\dagger_{\mathbf{n}s_e}(\xi)\sigma_- + \sigma_+ c_{\mathbf{n}s_e}(\xi)\right],\end{aligned} \tag{3.7}$$

where $V = \sqrt{2}\bar{V}$, $V_{\mathbf{n}s} = \sqrt{2}\bar{V}_{\mathbf{n}s}$. H_e describes that photons propagate unidirectionally to the $+x$ or $+\xi$ direction. We have used the operator transformations $c_e^\dagger(x) = \left[c_R^\dagger(x) + c_L^\dagger(-x)\right]/\sqrt{2}$, $c_o^\dagger(x) = \left[c_R^\dagger(x) - c_L^\dagger(-x)\right]/\sqrt{2}$, $c^\dagger_{\mathbf{n}s_e}(\xi) = \left[c^\dagger_{\mathbf{n}s_R}(\xi) + c^\dagger_{\mathbf{n}s_L}(-\xi)\right]/\sqrt{2}$, and $c^\dagger_{\mathbf{n}s_o}(\xi) = \left[c^\dagger_{\mathbf{n}s_R}(\xi) - c^\dagger_{\mathbf{n}s_L}(-\xi)\right]/\sqrt{2}$. The corresponding even-mode two-photon state is

given by

$$
\begin{aligned}
|\Phi_2\rangle = \Bigg(& \int dx_1 dx_2 \frac{1}{\sqrt{2}} \phi(x_1, x_2) c_e^\dagger(x_1) c_e^\dagger(x_2) \\
& + \sum_{\mathbf{n},s} \int dx d\xi \frac{1}{\sqrt{2}} \Big[\phi_{e\mathbf{n}s}(x,\xi) c_e^\dagger(x) c_{\mathbf{n}s_e}^\dagger(\xi) + \phi_{\mathbf{n}se}(\xi, x) c_{\mathbf{n}s_e}^\dagger(\xi) c_e^\dagger(x) \Big] \\
& + \int dx e(x) c_e^\dagger(x) \sigma_+ + \sum_{\mathbf{n},s} \int d\xi e_{\mathbf{n}s}(\xi) c_{\mathbf{n}s_e}^\dagger(\xi) \sigma_+ + \cdots \Bigg) |\varnothing\rangle,
\end{aligned}
\tag{3.8}
$$

where ϕ denotes the two-photon wave function in the even waveguided mode. $\phi_{e\mathbf{n}s}$ ($\phi_{\mathbf{n}se}$) denotes the wave function where the first (second) photon is in the even waveguided mode and the other photon in the even mode of channel $\mathbf{n}s$. e and $e_{\mathbf{n}s}$ denote the atomic excitation wave functions where the photon is in the even waveguided mode and $\mathbf{n}s$ channel, respectively. In Eq. (3.8), we omit the terms involving both photons in the scattering channels as it turns out that such terms do not directly affect the following results. The equations of motion relevant to the analysis are

$$
\begin{aligned}
\epsilon \phi(x_1, x_2) = & -i v_g \left(\partial_{x_1} + \partial_{x_2} \right) \phi(x_1, x_2) \\
& + \frac{1}{\sqrt{2}} \left[V e(x_1) \delta(x_2) + V e(x_2) \delta(x_1) \right] + \omega_g \phi(x_1, x_2),
\end{aligned}
\tag{3.9a}
$$

$$
\begin{aligned}
\epsilon \phi_{e\mathbf{n}s}(x, \xi) = & -i \left(v_g \partial_x + v \partial_\xi \right) \phi_{e\mathbf{n}s}(x, \xi) \\
& + \frac{1}{\sqrt{2}} \left[V_{\mathbf{n}s} e(x) \delta(\xi) + V e_{\mathbf{n}s}(\xi) \delta(x) \right] + \omega_g \phi_{e\mathbf{n}s}(x, \xi),
\end{aligned}
\tag{3.9b}
$$

$$
\begin{aligned}
\epsilon \phi_{\mathbf{n}se}(\xi, x) = & -i \left(v \partial_\xi + v_g \partial_x \right) \phi_{\mathbf{n}se}(\xi, x) \\
& + \frac{1}{\sqrt{2}} \left[V e_{\mathbf{n}s}(\xi) \delta(x) + V_{\mathbf{n}s} e(x) \delta(\xi) \right] + \omega_g \phi_{\mathbf{n}se}(\xi, x),
\end{aligned}
\tag{3.9c}
$$

$$
\begin{aligned}
\epsilon e(x) = & \omega_e e(x) - i v_g \partial_x e(x) + \frac{V}{\sqrt{2}} \left[\phi(x, 0) + \phi(0, x) \right] \\
& + \sum_{\mathbf{n},s} \frac{V_{\mathbf{n}s}}{\sqrt{2}} \left[\phi_{e\mathbf{n}s}(x, 0) + \phi_{\mathbf{n}se}(0, x) \right].
\end{aligned}
\tag{3.9d}
$$

Similar to the single-photon case, we now express $\phi_{e\mathbf{n}s}(x, 0)$ and $\phi_{\mathbf{n}se}(0, x)$ in terms of e in Eq. (3.9d). From continuous boundary condition near $x = 0$ in Eqs. (3.9b) and (3.9c), one

obtains

$$\begin{aligned}\phi_{e\mathbf{n}s}(x,0^+)-\phi_{e\mathbf{n}s}(x,0^-)&=-i\frac{V_{\mathbf{n}s}}{\sqrt{2}v}e(x),\\ \phi_{\mathbf{n}se}(0^+,x)-\phi_{\mathbf{n}se}(0^-,x)&=-i\frac{V_{\mathbf{n}s}}{\sqrt{2}v}e(x).\end{aligned}\tag{3.10}$$

Plugging Eq. (3.10) into Eq. (3.9d), one obtains

$$\epsilon e(x)=(\omega_e-i\sum_{\mathbf{n},s}\frac{\bar{V}_{\mathbf{n}s}^2}{v})e(x)-iv_g\partial_x e(x)+\frac{V}{\sqrt{2}}\left[\phi(x,0)+\phi(0,x)\right],\tag{3.11}$$

where we have used $\phi_{e\mathbf{n}s}(x,0)=[\phi_{e\mathbf{n}s}(x,0^+)+\phi_{e\mathbf{n}s}(x,0^-)]/2$. In Eq. (3.11), we have also employed the condition $\phi_{e\mathbf{n}s}(x,0^-)=0$. $\phi_{e\mathbf{n}s}(x,0^-)$ is the probability amplitude when one photon is at x in the even waveguided mode and the other photon is at $\xi=0^-$ in the even mode of channel $\mathbf{n}s$. Since the photon leaks from the atom to the scattering channels at $\xi=0$, and the photon can only propagate in the $+\xi$ direction, $\phi_{e\mathbf{n}s}(x,0^-)$ vanishes.

Eqs. (3.9a) and (3.11) now form a set of self-consistent equations that describe two-photon transport, which can also be derived by a reduced non-Hermitian Hamiltonian and a restricted eigenstate. This procedure validates the approach in the two-photon case.

3.4.2 N-photon Case

Subject to the same even-mode scenario in Eq. (3.7), the N-photon general state is given by

$$
\begin{aligned}
|\Phi_N\rangle =& \Bigg(\int dx_1 \cdots dx_N \frac{1}{\sqrt{N!}} \phi(x_1, \cdots, x_N) c_e^\dagger(x_1) \cdots c_e^\dagger(x_N) \\
&+ \sum_{\mathbf{n},s} \int dx_1 \cdots dx_N \frac{1}{\sqrt{N!}} \sum_j \phi_{\mathbf{n}s_j}(x_1, \cdots, x_j, \cdots, x_N) c_e^\dagger(x_1) \cdots c_e^\dagger(x_{j-1}) c_{\mathbf{n}s_e}^\dagger(\xi) c_e^\dagger(x_{j+1}) \cdots c_e^\dagger(x_N) \\
&+ \int dx_1 \cdots dx_{N-1} \frac{1}{\sqrt{(N-1)!}} e(x_1, \cdots, x_{N-1}) c_e^\dagger(x_1) \cdots c_e^\dagger(x_{N-1}) \sigma_+ \\
&+ \sum_{\mathbf{n},s} \int dx_1 \cdots dx_{N-1} \frac{1}{\sqrt{(N-1)!}} \\
&\sum_j e_{\mathbf{n}s_j}(x_1, \cdots, x_{N-1}) c_e^\dagger(x_1) \cdots c_e^\dagger(x_{j-1}) c_{\mathbf{n}s_e}^\dagger(\xi) c_e^\dagger(x_{j+1}) \cdots c_e^\dagger(x_{N-1}) \sigma_+ + \cdots \Bigg) |\varnothing\rangle,
\end{aligned}
\tag{3.12}
$$

where ϕ denotes the N-photon wave function in the even waveguided mode. $\phi_{\mathbf{n}s_j}$ denotes the N-photon wave function wherein the j-th photon is in the even mode of channel $\mathbf{n}s$, while all others are in the even waveguided mode ($j = 1,\ 2,\ 3,\ \cdots,\ N$). e denotes the atomic excitation amplitude when $N-1$ photons are in the even waveguided mode. $e_{\mathbf{n}s_j}$ denotes the atomic excitation where the photon arrangement is the same as $\phi_{\mathbf{n}s_j}$. The equations of

motion of relevant variables are given by

$$\begin{aligned}
&\epsilon\phi(x_1,\cdots,x_N)=\omega_g\phi-iv_g\left(\partial_{x_1}+\cdots+\partial_{x_N}\right)\phi\\
&+\frac{V}{\sqrt{N}}\sum_i e(x_1,\cdots,x_{i-1},x_{i+1},\cdots,x_N)\delta(x_i),
\end{aligned}\tag{3.13a}$$

$$\begin{aligned}
&\epsilon\phi_{\mathbf{n}s_j}(x_1,\cdots,x_{j-1},\xi,x_j,\cdots,x_{N-1})=\omega_g\phi_{\mathbf{n}s_j}\\
&-iv_g\left(\partial_{x_1}+\cdots+\frac{v}{v_g}\partial_\xi+\cdots+\partial_{x_{N-1}}\right)\phi_{\mathbf{n}s_j}\\
&+\frac{1}{\sqrt{N}}\Big[V_{\mathbf{n}s}e(x_1,\cdots,x_{j-1},x_j,\cdots,x_{N-1})\delta(\xi)\\
&+\sum_{i,i\neq j}Ve_{\mathbf{n}s_i}(x_1,\cdots,x_{i-1},x_{i+1},\cdots,x_{N-1})\delta(x_i)\Big],
\end{aligned}\tag{3.13b}$$

$$\begin{aligned}
&\epsilon e(x_1,\cdots,x_{N-1})=\omega_e e-iv_g\Big(\partial_{x_1}+\cdots+\partial x_{N-1}\Big)e\\
&+\frac{V}{\sqrt{N}}\left[\phi(0,x_1,\cdots,x_{N-1})+\cdots+\phi(x_1,\cdots,x_{N-1},0)\right]\\
&+\sum_{\mathbf{n},s}\frac{V_{\mathbf{n}s}}{\sqrt{N}}\sum_j\phi_{\mathbf{n}s_j}(x_1,\cdots,x_{j-1},0,x_j,\cdots,x_{N-1}).
\end{aligned}\tag{3.13c}$$

Similar to Eq. (3.10), for the N-photon case, now we have

$$\begin{aligned}
&\phi_{\mathbf{n}s_j}(x_1,\cdots,x_{j-1},0^+,x_j,\cdots,x_{N-1})=\\
&\phi_{\mathbf{n}s_j}(x_1,\cdots,x_{j-1},0^-,x_j,\cdots,x_{N-1})-i\frac{V_{\mathbf{n}s}}{\sqrt{N}v}e(x_1,\cdots,x_{N-1}).
\end{aligned}\tag{3.14}$$

Plugging Eq. (3.14) into Eq. (3.13c), one obtains

$$\begin{aligned}
\epsilon e(x_1,\cdots,x_{N-1})=&\left(\omega_e-i\sum_{\mathbf{n},s}\frac{\bar{V}^2_{\mathbf{n}s}}{v}\right)e-iv_g\Big(\partial_{x_1}+\cdots+\partial_{x_{N-1}}\Big)e\\
&+\frac{V}{\sqrt{N}}\left[\phi(0,x_1,\cdots,x_{N-1})+\cdots+\phi(x_1,\cdots,x_{N-1},0)\right].
\end{aligned}\tag{3.15}$$

Eqs. (3.13a) and (3.15) are now self-consistent to describe the N-photon correlated transport, which can be derived from a reduced non-Hermitian Hamiltonian and a restricted eigen-state, thereby validating the approach in the N-photon case. We have laid out an exact dissipation model for arbitrary photonic Fock states. As a coherent state is a linear superposition of Fock states, our dissipation model also applies when the input is a coherent state. We also note that the conclusion remains valid regardless of the explicit form of $\bar{V}_{\mathbf{n}s}$.

One now converts the expression of γ_S from the discrete phase space to the continuum. Writing that $\sum_{\mathbf{n},s} \bar{V}^2_{\mathbf{n},s}/v = \sum_s \sum_{i,j} \bar{V}^2_s(\theta_i, \varphi_j)\Delta\theta_i\Delta\varphi_j/\pi^2 v$ and taking the limit $M_1, M_2 \to \infty$, one obtains

$$\gamma_S = \sum_s \frac{1}{\pi^2} \int_0^\pi d\theta \int_0^\pi d\varphi \frac{\bar{V}^2_s(\theta,\varphi)}{v}. \tag{3.16}$$

We also note that different discretization schemes only differ in a Jacobian and should lead to the same continuum limit. When the discretization scheme is to discretize the solid angle, then γ_S takes the form $\sum_s 1/2\pi \int_0^\pi \sin\theta d\theta \int_0^\pi d\varphi \bar{V}^2_s(\theta,\varphi)/v$.

3.5 Validity of Non-Hermitian Hamiltonian from Scattering Matrix

The information of the scattering eigenstates of the system dictates the scattering matrix. The scattering matrix $\mathbf{S}$ maps an arbitrary in-state (the prepared photonic state injected into the waveguide) into the out-state: $\mathbf{S}|\text{in}\rangle = |\text{out}\rangle$ [20]. In reality, however, only the waveguided photonic states are measurable but not those leaked into the reservoir. Consequently, a restricted scattering matrix which maps the in-state into the waveguided photonic states solely is of practical importance. Without loss of generality, we take the two-photon case as an example while an arbitrary N-photon case can be examined in a similar manner.

In the reservoir-free case, $|W_{k,p}\rangle$ and $|B_K\rangle$ are orthogonal eigenstates of the scattering matrix so that the scattering matrix is diagonal, given by $\mathbf{S}_{e^{(2)}} = \sum_{k\leq p} t_k t_p |W_{k,p}\rangle\langle W_{k,p}| + \sum_K t_K |B_K\rangle\langle B_K|$ [20]. By construction, in the non-excitable reservoir scenario, *e.g.*, the restricted scattering matrix is $\mathbf{S}^r_{e^{(2)}} = \sum_{k\leq p} \bar{t}'_k \bar{t}'_p |W_{k,p}\rangle\langle W_{k,p}| + \sum_K \bar{t}'^{(2)}_K |B_K\rangle\langle B_K|$, where $\bar{t}'_{k,p} = (\omega_{k,p} - \bar{\Omega}' - i\Gamma/2)/(\omega_{k,p} - \bar{\Omega}' + i\Gamma/2)$, $\bar{t}'^{(2)}_K = (Kv_g - 2\bar{\Omega}' - 2i\Gamma)/(Kv_g - 2\bar{\Omega}' + 2i\Gamma)$, and the renormalized frequency $\bar{\Omega}' = \Omega - i\gamma_S$, where γ_S is the photonic scattering loss rate [60]. Apparently, by examining the restricted scattering matrix, the non-Hermitian Hamiltonian description is valid by adding a purely imaginary part $-i\gamma_S$ in the original Hermitian Hamiltonian.

3.6 Summary and Outlook

The atomic dissipation given rise from the photonic scattering channels has been discussed in the literature. Conventionally, photonic scattering channels are alternatively labeled by folded scattering channel modes $\mathbf{n}s_u$ and $\mathbf{n}s_d$ (see Ref. [73]). By invoking analogous transformations of $c^\dagger_{\mathbf{n}s_e}(\xi) = \left[c^\dagger_{\mathbf{n}s_u}(\xi) + c^\dagger_{\mathbf{n}s_d}(\xi)\right]/\sqrt{2}$ and $c^\dagger_{\mathbf{n}s_o}(\xi) = \left[c^\dagger_{\mathbf{n}s_u}(\xi) - c^\dagger_{\mathbf{n}s_d}(\xi)\right]/\sqrt{2}$, it is straightforward to show that the two labeling schemes are mathematically equivalent.

Finally, we comment on the cavity dissipations. By employing the explicit photon-cavity interaction [72] and using the same approach outlined above, one can also show that the photonic scattering channels also result in a reduced non-Hermitian Hamiltonian (by adding an imaginary part to the eigen-frequency of cavity modes) and a restricted eigenstate (omitting the scattering channels of the reservoir in the wave function). Thus, our approach provides a computationally feasible yet numerically exact platform for studying correlated photon transport in waveguide QED systems in the presence of both atomic and cavity dissipations.

Chapter 4

Correlated Multi-photon Dissipation Theory: Material Loss

4.1 Introduction

Apart from the non-excitation reservoir scenario as presented in Chap. 3, on one hand, the environment contains an excitable medium, and is conventionally treated as a reservoir of oscillators [72, 74]. Conventionally, a very fruitful approach to studying the effects of dissipation is the density matrix approach. Such an approach traces over the reservoir degrees of freedom and phenomenologically parametrizes the system-reservoir interaction as damping terms in the Lindblad superoperators in the resultant quantum master equation for a dissipative system [75, 76]. The detailed information of the system-reservoir entanglement is eliminated at the very beginning in the density matrix approach. As a result, the density matrix approach provides a probabilistic measure for the system evolutions in terms of mixed states. Another aspect is that, as the density matrix approach does not include the wave

function of the photon field, the photon-atom entanglement can not be directly described. Other successful approaches include the quantum Langevin approach, which is also widely used to investigate the dissipation-driven fluctuation and temporally-correlated statistics [77]; and the quantum jump approach which has been developed for statistical single-photon loss processes [78] and can be numerically simulated using the Monte-Carlo techniques [79]. The limitations of the density matrix approach with regard to the entanglement also apply to the quantum Langevin and the quantum jump approaches.

In this chapter, we apply an entanglement-preserving approach to investigate the waveguide QED system of the same configuration as that in Chap. 3, but now instead with an excitable reservoir that consists of infinitely many quantum oscillators. Such a scenario is ubiquitous in practical photonic systems (e.g., free-carrier absorption in highly-doped semiconductor waveguide [80], absorption-driven cladding loss in photonic crystal fiber [81], and generic material absorption in other silica-based photonic devices [82, 83]), and has been of great theoretical and experimental interest to the studies of waveguide QED systems. We rigorously confirm that the reduced non-Hermitian Hamiltonian description breaks down for correlated multi-photon process. We also carry out the calculation using the density matrix approach and show that the result obtained from the Markovian density matrix approach is the lowest order of α obtained using the entanglement-preserving approach. Furthermore, we identify a weak-reservoir limit where the non-Hermitian Hamiltonian is still valid.

4.2 Model and Hamiltonian

The waveguide QED system considered is shown schematically in Fig. 4.1. The system (S) consists of a two-level atom coupled to a single-mode photonic waveguide, and an N-photon Fock state, $|N\rangle$, is injected into the waveguide from the left. The incoming photons interact

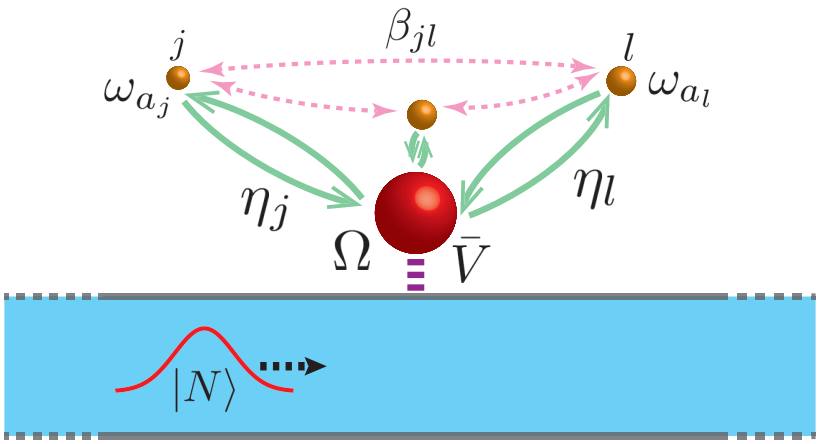

Figure 4.1: Schematics of the waveguide QED system with an excitable reservoir. A two-level atom (represented by a red sphere) is coupled to the one-dimensional single-mode photonic waveguide. The atom is further coupled to a reservoir that consists of infinitely many excitable oscillators (represented by yellow dots). j and l are indices of any two oscillators ($j, l = 1, 2, \cdots$). Ω and ω_a denote transition frequencies for the atom and the oscillators, respectively. $\bar{V}$, η, and β are the atom-photon, atom-oscillator, and the inter-oscillator coupling strengths, respectively. $|N\rangle$ denotes the incoming N-photon Fock state.

with the atom through absorptions, spontaneous, and stimulated emission processes. On the other hand, due to the coupling between the atom and the external excitable oscillators, the photon may leak out to the reservoir and undergo secondary scattering processes between the oscillators. The Hamiltonian describing the waveguide QED system in Fig. 4.1, H_S, is

$$\begin{aligned}\frac{H_S}{\hbar} = \int dx \Big\{ & c_R^\dagger(x)(-iv_g\partial_x)c_R(x) + c_L^\dagger(x)(iv_g\partial_x)c_L(x) \\ & + \bar{V}\delta(x)[(c_R^\dagger(x) + c_L^\dagger(x))\sigma_- + \sigma_+(c_R(x) + c_L(x))]\Big\} \\ & + \omega_e a_e^\dagger a_e + \omega_g a_g^\dagger a_g,\end{aligned} \tag{4.1}$$

where the linear dispersion approximation and the rotating-wave approximation are employed [72]. Notations are defined the same as Eq. (2.1). The Hamiltonian describing the

reservoir, H_R, is given by

$$\begin{aligned}\frac{H_R}{\hbar} =& \sum_j \left[(\omega_{e_j} - i\varepsilon) a_{e_j}^\dagger a_{e_j} + \omega_{g_j} a_{g_j}^\dagger a_{g_j}\right] \\ &+ \sum_{j,l,j\neq l} \frac{\beta_{jl}}{2} \left(\sigma_{j+}\sigma_{l-} + \sigma_{l+}\sigma_{j-}\right),\end{aligned} \tag{4.2}$$

where $a_{g_j}^\dagger$ (a_{g_j}) denotes the creation (annihilation) operator for the ground state of the j-th oscillator with energy $\hbar\omega_{g_j}$ ($j = 1, 2, \cdots$); $a_{e_j}^\dagger$, a_{e_j}, and ω_{e_j} are similarly defined for its excited state; and $\omega_{a_j} \equiv \omega_{e_j} - \omega_{g_j}$ is the transition frequency of the j-th oscillator. $\sigma_{j+} = a_{e_j}^\dagger a_{g_j}$ ($\sigma_{j-} = a_{g_j}^\dagger a_{e_j}$) denotes the raising (lowering) operator for the j-th oscillator. β_{jl} represents the inter-oscillator coupling strength between the j-th and the l-th oscillators. In the following, a general description is provided without imposing special constraints on the functional form of β_{jl}'s, thus allowing the incorporation of various scenarios. For example, the value of β_{jl} can decrease as the separation between the the j-th and the l-th oscillators increases according to a specified fashion so that only short-ranged hops make contributions. Each oscillator has an intrinsic scattering loss rate ε, which is taken to be 0^+ at the end of the calculation to ensure the causality condition. It is worth noting that albeit only frequency and inter-oscillator coupling of the reservoir are considered, our approach can readily incorporate more reservoir degrees of freedom (*e.g.*, mode, polarization, spin, intrinsic scattering loss, etc). The Hamiltonian describing the system-reservoir coupling, H_{SR}, is

$$\frac{H_{SR}}{\hbar} = \sum_j \eta_j \left(\sigma_{j+}\sigma_- + \sigma_+\sigma_{j-}\right), \tag{4.3}$$

where η_j is the coupling strength between the atom and the j-th oscillator. The Hamiltonian describing the combined system $S \oplus R$ (waveguide QED system + reservoir), H, is given by $H_S + H_R + H_{SR}$.

4.3 Single-photon Case

For the single-photon case, the general single-photon eigenstate of the combined system, $|\Phi_1\rangle$, is

$$|\Phi_1\rangle = \Big(\int dx \left[\phi_R(x) c_R^\dagger(x) + \phi_L(x) c_L^\dagger(x) \right] + e\sigma_+ + \sum_j \phi_j \sigma_{j+} \Big) |\varnothing\rangle, \tag{4.4}$$

where ϕ_R (ϕ_L) denotes the right- (left-) moving single-photon wave function. e and ϕ_j denote the excitation amplitude for the atom and the j-th oscillator, respectively. $|\varnothing\rangle$ is the photonic vacuum state that has no waveguided photons; the atom is in the ground state; and none of the oscillators are excited. By applying Schrödinger Equation $H|\Phi_1\rangle = \hbar\tilde{\epsilon}|\Phi_1\rangle$, where $\hbar\tilde{\epsilon} = \hbar(\omega_k + \omega_g + \sum_j \omega_{g_j})$ is the total energy of the combined system with $\hbar\omega_k$ being the energy of the incident photon, and equating the coefficients for each basis, the equations of motion are obtained as follows,

$$\omega_k \phi_R(x) = -iv_g \partial_x \phi_R(x) + V\delta(x)e, \tag{4.5a}$$

$$\omega_k \phi_L(x) = iv_g \partial_x \phi_L(x) + V\delta(x)e, \tag{4.5b}$$

$$\omega_k e = V\left[\phi_R(0) + \phi_L(0)\right] + \Omega e + \sum_j \eta_j \phi_j, \tag{4.5c}$$

$$\omega_k \phi_j = (\omega_{a_j} - i\varepsilon)\phi_j + \eta_j e + \sum_{l, l\neq j} \beta_{jl}\phi_l. \tag{4.5d}$$

By substituting Eq. (4.5d) into Eq. (4.5c) (see Ref. [84]), Eq. (4.5c) now reads as

$$\begin{aligned} &\omega_k e = V\left[\phi_R(0) + \phi_L(0)\right] + (\Omega + \alpha)e, \quad \text{where} \\ &\alpha = \sum_{n=1}^{\infty} \alpha_n, \quad \alpha_1 = \sum_{i_1} \frac{\eta_{i_1}^2}{\omega_k - \omega_{a_{i_1}} + i\varepsilon}, \\ &\alpha_n = \sum_{i_1} \sum_{i_2, i_2\neq i_1} \cdots \sum_{i_n, i_n \neq i_{n-1}} \frac{\eta_{i_1}\beta_{i_1 i_2}\cdots\beta_{i_{n-1}i_n}\eta_{i_n}}{\prod_{l=1}^{n}(\omega_k - \omega_{a_{i_l}} + i\varepsilon)}, \quad n = 2, 3, \cdots . \end{aligned} \tag{4.6}$$

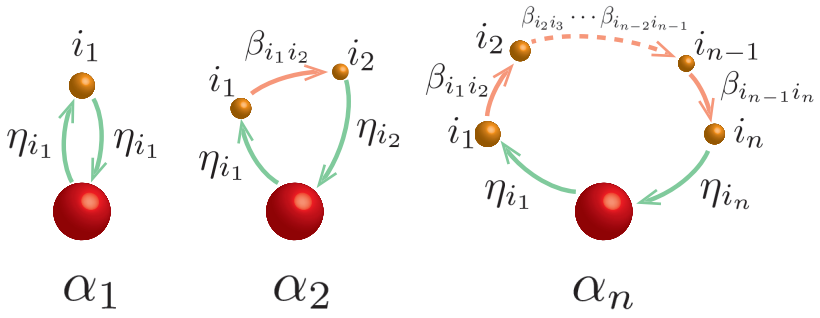

Figure 4.2: Graphic representation of the complex frequency renormalization $\alpha \equiv \sum_n \alpha_n$: for each α_n, the numerator describes a closed path of the photon, staring from the two-level atom (η) and hopping $n-1$ times between the oscillators in the reservoir (β's), and finally ending with the two-level atom (η).

Note that for each α_n, the numerator describes a closed path of the photon, starting from the two-level atom (the η_{i_1} term) and hopping $n-1$ times between the oscillators in the reservoir (the β's terms), and eventually ending with the two-level atom (the η_{i_n} term). The real part and the imaginary part of the complex frequency renormalization $\alpha = \Delta_M - i\gamma_M$ describe the shift of the transition frequency of the two-level atom and the dissipation rate, respectively, due to coupling to the excitable reservoir. Figure 4.2 provides a graphic representation of the numerators of α_n. The returning nature of the single-photon paths has a far-reaching consequence for the correlated multi-photon transport, as the returning times are statistical and generally breaks down the photonic temporal entanglement within the waveguide.

Together, Eqs. (4.5a), (4.5b), and (4.6) now form a set of self-consistent equations which only involve the system amplitudes ϕ_R, ϕ_L, and e. Such a result states that after taking into account the statistical fluctuations of the system-reservoir coupling (*i.e.*, η) and the secondary scattering characteristic of the reservoir (*i.e.*, β), the wave function information of ϕ_j can be traced over and incorporated in the renormalized frequency $\bar{\Omega} \equiv \Omega + \alpha$ ($\alpha \equiv \sum_{n=1}^{\infty} \alpha_n$). That is, the combined system can be described by a reduced Hamiltonian (substituting Ω with the renormalized transition frequency $\bar{\Omega}$ in the system Hamiltonian H_S), and a

restricted eigenstate $|\Phi_1\rangle = (\int dx \left[\phi_R(x)c_R^\dagger(x) + \phi_L(x)c_L^\dagger(x)\right] + e\sigma_+)|\varnothing\rangle$ which contains only the degrees of freedom of the system.

4.4 Multi-photon Case

4.4.1 Two-photon Case

For the dissipationless two-photon case when no reservoir is present, it has been shown that the two-photon plane-wave states alone do not form a complete set of two-photon eigenstates of the scattering matrix, and a two-photon bound state must be included for the completeness [20]. We now examine the effects of the reservoir for the plane-wave states and the bound state solutions separately.

Following the same even-odd mode decomposition technique in Chap. 3 one obtains the following even-mode Hamiltonian H_e describing the combined system,

$$\begin{aligned}\frac{H_e}{\hbar} = &\int dx \left\{c_e^\dagger(x)(-iv_g\partial_x)c_e(x) + V\delta(x)\left[c_e^\dagger(x)\sigma_- + \sigma_+ c_e(x)\right]\right\} \\ &+\omega_e a_e^\dagger a_e + \omega_g a_g^\dagger a_g + \sum_j \eta_j\left(\sigma_{j+}\sigma_- + \sigma_+\sigma_{j-}\right) \\ &+\sum_j \left((\omega_{e_j} - i\varepsilon)a_{e_j}^\dagger a_{e_j} + \omega_{g_j} a_{g_j}^\dagger a_{g_j}\right) \\ &+\sum_{j,l,j\neq l}\frac{\beta_{jl}}{2}\left(\sigma_{j+}\sigma_{l-} + \sigma_{l+}\sigma_{j-}\right),\end{aligned} \tag{4.7}$$

where $c_e^\dagger(x)$ ($c_e(x)$) is the operator to create (annihilate) a photon at position x in the even mode. $V = \sqrt{2}\bar{V}$ and $\Gamma \equiv V^2/v_g$ are the atom-photon coupling strength and atomic spontaneous emission rate into the waveguide in the even mode. The general form of the

two-photon interacting eigenstate of the combined system, $|\Phi_2\rangle$, is given by

$$\begin{aligned}|\Phi_2\rangle =&\Big(\iint dx_1 dx_2 \phi(x_1,x_2)\frac{1}{\sqrt{2}}c_e^\dagger(x_1)c_e^\dagger(x_2) \\ &+\int dx e(x)c_e^\dagger(x)\sigma_+ + \sum_j \int dx \phi_j(x)c_e^\dagger(x)\sigma_{j+} \\ &+\sum_j e_j\sigma_+\sigma_{j+} + \sum_{j,l,j<l} e_{jl}\sigma_{j+}\sigma_{l+}\Big)|\varnothing\rangle,\end{aligned} \tag{4.8}$$

where $\phi(x_1,x_2)$ denotes the wave function for two waveguided photons in the even mode. Due to the boson statistics, the wave function satisfies $\phi(x_1,x_2) = +\phi(x_2,x_1)$, and is continuous on the line $x_1 = x_2$. $e(x)$ is the probability amplitude distribution of one waveguided photon while the atom in the excited state. $\phi_j(x)$ denotes the probability amplitude distribution of one waveguided photon while the j-th oscillator in the excited state. e_j represents the excitation amplitude wherein two photons are absorbed by the atom and the j-th oscillator, respectively. e_{jl} is the excitation amplitude wherein two photons are absorbed by the j-th and the l-th oscillators, respectively. By applying the Schrödinger Equation, $H_e|\Phi_2\rangle = \hbar\tilde{\epsilon}|\Phi_2\rangle$,

one obtains the following equations of motion,

$$\begin{aligned}\epsilon\phi(x_1,x_2) =& -iv_g\left(\partial_{x_1}+\partial_{x_2}\right)\phi(x_1,x_2)\\ &+\frac{V}{\sqrt{2}}\left[\delta(x_1)e(x_2)+\delta(x_2)e(x_1)\right],\end{aligned} \tag{4.9a}$$

$$\begin{aligned}\epsilon e(x) =& -iv_g\partial_x e(x)+\frac{V}{\sqrt{2}}\left[\phi(0,x)+\phi(x,0)\right]\\ &+\Omega e(x)+\sum_j \eta_j\phi_j(x),\end{aligned} \tag{4.9b}$$

$$\begin{aligned}\epsilon\phi_j(x) =& -iv_g\partial_x\phi_j(x)+V\delta(x)e_j+(\omega_{a_j}-i\varepsilon)\phi_j(x)\\ &+\eta_j e(x)+\sum_{l,l\neq j}\beta_{jl}\phi_l(x),\end{aligned} \tag{4.9c}$$

$$\begin{aligned}\epsilon e_j =& V\phi_j(0)+\sum_{l,l<j}\eta_l e_{lj}+\sum_{l,l>j}\eta_l e_{jl}\\ &+\left(\omega_a+\omega_{a_j}-i\varepsilon\right)e_j+\sum_{l,l\neq j}\beta_{jl}e_l,\end{aligned} \tag{4.9d}$$

$$\begin{aligned}\epsilon e_{jl} =& \eta_j e_l+\eta_l e_j+\left(\omega_{a_j}+\omega_{a_l}-2i\varepsilon\right)e_{jl}+\sum_{m,m\neq l,m<j}\beta_{lm}e_{mj}\\ &+\sum_{m,m\neq l,m>j}\beta_{ml}e_{jm}+\sum_{m,m\neq j,m<l}\beta_{jm}e_{ml}+\sum_{m,m\neq j,m>l}\beta_{mj}e_{lm},\end{aligned} \tag{4.9e}$$

where $\hbar\epsilon=\hbar(\tilde{\epsilon}-\omega_g-\sum_j\omega_{g_j})$ gives the total energy of two photons.

Our computational strategy is as follows. We will solve Eqs. (4.9a), (4.9b), and (4.9c) to obtain the solution of the interacting eigenstate of H_e for the variables restricted in the system of interest (*i.e.*, $\phi(x_1,x_2)$ and $e(x)$). In particular, we will show that the wavefunctions of the reservoir degrees of freedom (*i.e.*, $\phi_j(x)$, e_j, and e_{jl}) can be traced over, and have no direct relevance to our results, which is similar to the single-photon case. Thus, in the end, Eqs. (4.9d) and (4.9e) are not directly involved in the calculation. The two-photon in- and out- states can be constructed based upon the interacting eigenstates for restricted

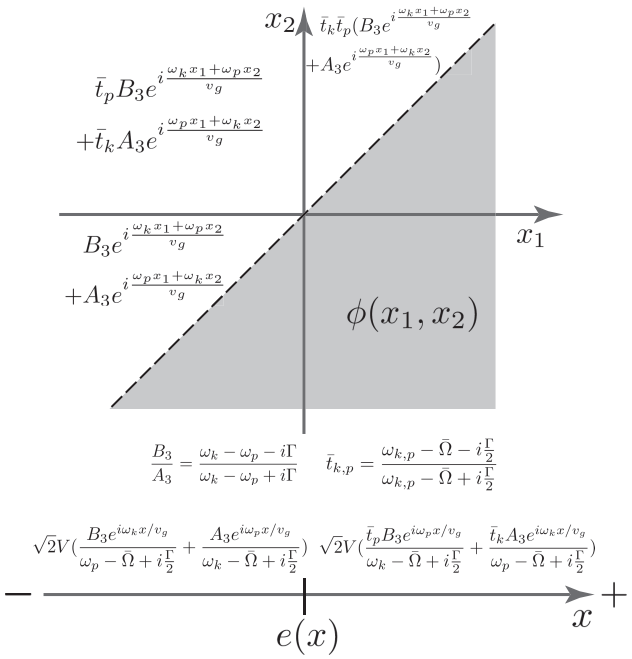

Figure 4.3: Interacting eigenstate solution of the restricted system variables $\phi(x_1, x_2)$ and $e(x)$ to Eqs. (4.8) for the two-photon plane-wave state case. $\phi(x_1, x_2)$ is specified in Region 1, 2, and 3. $e(x)$ is specified for both $x > 0$ and $x < 0$.

system variables (*i.e.*, $|\Phi_2\rangle = \Big(\iint dx_1 dx_2 \phi(x_1, x_2) c_e^\dagger(x_1) c_e^\dagger(x_2)/\sqrt{2} + \int dx e(x) c_e^\dagger(x) \sigma_+ \Big) |\varnothing\rangle$), and further normalized to obtain eigenstates of the restricted scattering matrix.

Plane-wave Solution. By adopting the divide and conquer scheme, eigen wave functions of the restricted system variables (*i.e.*, $\phi(x_1, x_2)$ and $e(x)$) for the two-photon plane-wave solution is obtained, as summarized in Fig. 4.3. Interestingly, the solutions follow the same form as that in the reservoir-free case (see Fig. 7 in Ref. [85]), yet with a frequency renormalization $\Omega \to \bar{\Omega}$ that is the same as the single-photon case. By applying Lippmann-Schwinger formalism, one can construct the normalized eigenstate $|W_{k,p}\rangle$ of the restricted even-mode S-matrix, $\mathbf{S}^r_{e^{(2)}}$, in the following form,

$$
\begin{aligned}
|W_{k,p}\rangle &= \iint dx_1 dx_2 W_{k,p}(x_1, x_2) \frac{1}{\sqrt{2}} c_e^\dagger(x_1) c_e^\dagger(x_2) |\varnothing\rangle, \quad \text{where} \\
W_{k,p}(x_1, x_2) &= \frac{\sqrt{2} e^{iKx_c} [2\Delta \cos \Delta x_d - \kappa \mathrm{sgn}(x_d) \sin \Delta x_d]}{2\pi \sqrt{[4\Delta^2 + \kappa^2]}},
\end{aligned}
\tag{4.10}
$$

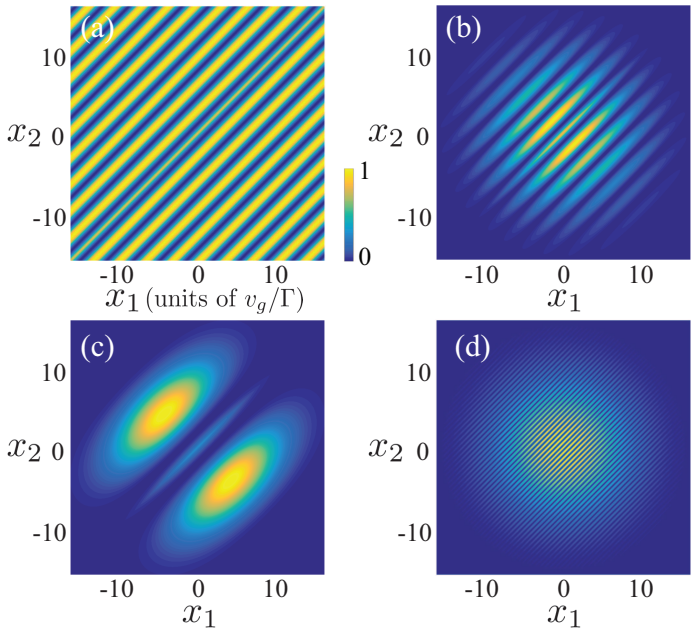

Figure 4.4: Density plot for the wavefunction of the two-photon plane-wave state. (a) $|W_{k,p}|^2$ when $\Delta = \kappa$. (b) Gaussian-modulated two-photon plane-wave state $|W^G_{k,p}|^2$ when $\Delta = \kappa$. $|W^G_{k,p}|^2$ is centered at $x_1 = x_2 = x_o = 0$. (c) $|W^G_{k,p}|^2$ when $\Delta = 0.2\kappa$. (d) $|W^G_{k,p}|^2$ when $\Delta = 5\kappa$. For the density plot, the numerical values for one unit scale are (a) 0.25, (b) 0.23, (c) 0.027, and (d) 5 in units of Γ^2/v_g^2 (which has a unit of $1/\text{Length}^2$).

where $K = \epsilon/v_g$, $x_d = x_1 - x_2$, $x_c = (x_1 + x_2)/2$, $\kappa = \Gamma/v_g$, $\Delta = (\omega_k - \omega_p)/2v_g$ and sgn is the sign function. It can be immediately obtained from the analysis outlined above that $\mathbf{S}^r_{e^{(2)}}|W_{k,p}\rangle = \bar{t}_k\bar{t}_p|W_{k,p}\rangle$. Here, we note that $|W_{k,p}\rangle$ follows exactly the same functional form as that in the reservoir-free case.

To visualize the real-space representation of the two-photon plane-wave state, here we plot the wave function density $|W_{k,p}(x_1, x_2)|^2$ in Fig. 4.4. Figure. 4.4(a) plots the case of $\Delta = \kappa$, wherein the interference fringes are extended along the diagonal ($x_1 = x_2$), and periodically modulated in the transverse direction ($x_1 = -x_2$). Such a periodic structure results from the fact that given a fixed Δ, $|W_{k,p}|^2$ only depends on the distance between two individual photons, *i.e.*, $x_1 - x_2$, and is modulated by the sinusoidal functions. The spatial period is $\pi/\sqrt{2}\Delta$, and the corresponding spatial frequency is $2\sqrt{2}\Delta$. The maximal

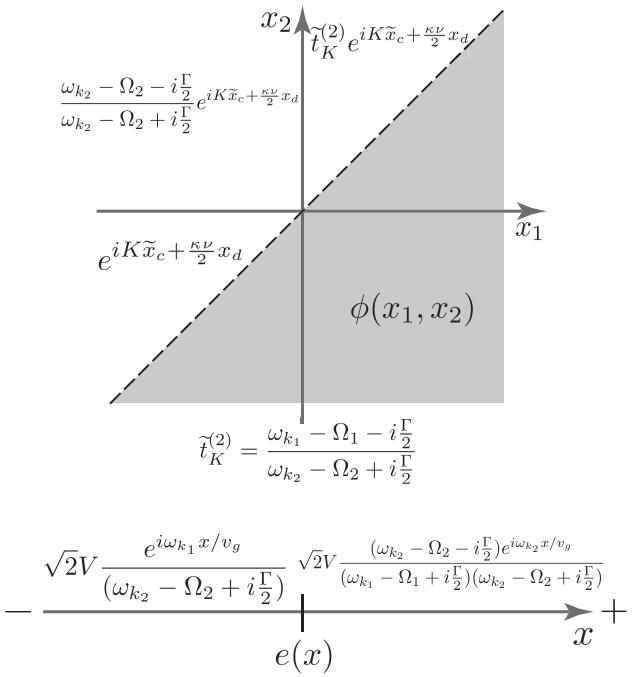

Figure 4.5: Interacting eigenstate solution of the restricted system variables $\phi(x_1, x_2)$ and $e(x)$ to Eqs. (4.8) for the reservoir-modified two-photon bound state case.

density is $|W_{k,p}|^2_{\max} = 1/2\pi^2$, which is attained when $\Delta x_d = m\pi - \arccos(2\Delta/\sqrt{4\Delta^2+\kappa^2})$ ($m = 0, \pm1, \pm2, \cdots$). Nonetheless, the density on the $x_1 = x_2$ line does not attain the maximal density, which is equal to only $4\Delta^2/(4\Delta^2+\kappa^2)$ of $|W_{k,p}|^2_{\max}$.

In practice, the two-photon states exist as wavepackets (pulses), which have a finite spatial size and a finite frequency bandwidth. Figure 4.4(b) plots the density of the Gaussian-modulated plane-wave state $W^G_{k,p} \equiv W_{k,p} \times \mathcal{M}$, where $\mathcal{M} \equiv \exp[-(x_1-x_o)^2/4\sigma_x^2 - (x_2-x_o)^2/4\sigma_x^2]$ is the modulation function. x_o is the center position of the wave packet. The spatial width of the modulation σ_x is chosen to be $5v_g/\Gamma$ such that the pulse has a narrow bandwidth $\Gamma/10$. $|W^G_{k,p}|^2$ decreases as $|x_1 - x_2|$ increases. Figure 4.4(c) and (d) plot $|W^G_{k,p}|^2$ for $\Delta = 0.2\kappa$ and $\Delta = 5\kappa$, respectively, wherein the number of fringes reflects the spatial beating frequencies of the two photons.

Reservoir-modified Bound State Solution. After some algebra, it is found that $|B_K\rangle$ fails to be an eigenstate in the presence of the reservoir. Instead, we identify the interacting eigenstate solution for a reservoir-modified bound state $|D_K\rangle$, shown in Fig. 4.5. Specifically, $|D_K\rangle$ takes the following form,

$$\begin{aligned} |D_K\rangle &= \iint dx_1 dx_2 D_K(x_1, x_2) \frac{1}{\sqrt{2}} c_e^\dagger(x_1) c_e^\dagger(x_2), \quad \text{where} \\ D_K(x_1, x_2) &= \sqrt{\frac{\kappa\nu}{4\pi}} e^{iK\frac{\xi_1 x_1 + \xi_2 x_2}{2} - \frac{\kappa\nu}{2}|x_1 - x_2|}. \end{aligned} \tag{4.11}$$

ν and $\xi_{1/2}$ are dimensionless constants that characterize the reservoir-modified correlation width and re-distributed photon energy, respectively. Note that in the reservoir-free case, the transmission coefficient for the bound state is $t_K^{(2)} = (Kv_g/2 - \Omega - i\Gamma)/(Kv_g/2 - \Omega + i\Gamma)$. It can be shown that, in the absence of the reservoir (*i.e.*, $\eta = \beta = 0$), $\widetilde{t}_K^{(2)}$ reduces to $t_K^{(2)}$ in the absence of the reservoir. Nonetheless, when the reservoir is present, the renormalized transmission coefficient for the reservoir-modified bound state $\widetilde{t}_K^{(2)}$ can not be obtained by simply using a frequency renormalization in $t_K^{(2)}$.

To illustrate the reservoir-induced effect on the bound state, we now plot the wave function density for the bound state $|B_K\rangle$ and the reservoir-modified bound state $|D_K\rangle$ in Fig. 4.6. Figure 4.6(a) plots $|B_K|^2$ wherein the bound state is unmodulated and thus extends along the diagonal ($x_1 = x_2$); the state has a correlation width of $1/\kappa$ along the transverse direction ($x_1 = -x_2$). That is, two photons propagate in a collocated manner within a spatial range of $1/\kappa$. To represent a practical pulse of finite spatial size, we plot the density for a Gaussian-modulated bound state $|B_K\mathcal{M}|^2$ in Fig. 4.6(b) using the same parameter set of $\mathcal{M}$ as the preceding plane-wave case. For the modulated state, the spatial size of the modulation is the coherence length, which also determines the coherence time of the pulse. Specifically, the coherence length of $|B_K\mathcal{M}|^2$ is determined by the Gaussian modulation parameter σ_x while the correlation width remains the same as $|B_K|^2$. We further plot the wave function

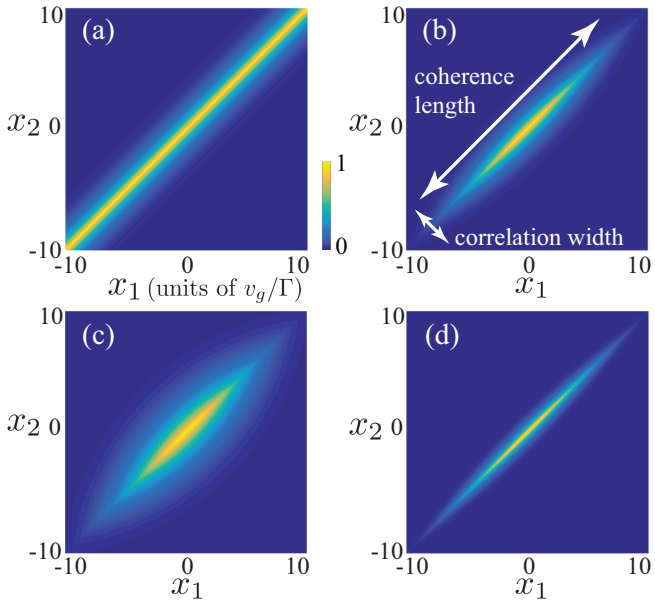

Figure 4.6: Wave function density plot for the reservoir-free two-photon bound state $|B_K\rangle$ and the reservoir-modified two-photon bound state $|D_K\rangle$. (a) Two-photon bound state $|B_K|^2$. (b) Gaussian-modulated two-photon bound state $|B_K\mathcal{M}|^2$. The correlation length and the coherence width are given by $1/\kappa$ and σ_x, respectively. $|B_K\mathcal{M}|^2$ is centered at $x_1 = x_2 = x_o = 0$. (c) Gaussian-modulated reservoir-modified bound state $|D_K\mathcal{M}|^2$ when $\nu = 0.5$. (d) $|D_K\mathcal{M}|^2$ when $\nu = 2$. For the density plot, the numerical values of one unit scale is (a) 0.4, (b) 0.0025, (c) 0.00012, and (d) 0.005 in units of Γ^2/v_g^2 (which has a unit of $1/\text{Length}^2$).

density of the Gaussian-modulated reservoir-modified bound state $|D_K\mathcal{M}|^2$ to visualize the effect of the reservoir on the bound state. Figure 4.6(c) and (d) plot $|D_K\mathcal{M}|^2$ for $\nu = 0.5$ and $\nu = 2$, respectively, wherein the correlation width is doubled and halved, respectively. That is, the correlation width of $|D_K\mathcal{M}|^2$ now becomes $1/\kappa\nu$ where varying ν values depends on the system-reservoir coupling (*i.e.*, described by η) and the secondary scattering strength in the reservoir (*i.e.*, described by β). Unmodulated reservoir-modified bound state $|D_K|^2$ is not plotted because all entanglement information is already provided in the plots for the modulated case in Fig. 4.6(c) and (d).

4.4.2 N-photon Case

Having studied the single-photon and the two-photon cases, we now examine the case for an arbitrary N-photon Fock state transport. It has been rigorously confirmed that, in the reservoir-free case, a complete set of N-photon in-states can be classified into three categories, *i.e.*, the N-photon extended state, N-photon bound state, and N-photon hybrid states [21]. Specifically, the N-photon extended state is a generalization of two-photon plane-wave state to the N-photon case, wherein all N photons are uncorrelated. For the N-photon bound state, all photons are entangled. In particular, any two-photon pair is spatially characterized by a correlation width v_g/Γ. The N-photon hybrid states are product states of plane-wave and bound states. Hereafter we will focus on the extended and bound state solutions. The hybrid state case can be examined through a similar procedure.

By applying the divide and conquer scheme, the interacting eigenstates of N-photon extended state remains the same form as that in the reservoir-free case whereas the transmission amplitudes are renormalized. The form of the extended state solution indicates that the N photons interact with the lossy atom independently. Similar to the two-photon case, it can be shown that the N-photon bound state $|B_K\rangle$ fails to be an eigenstate of restricted scattering

matrix $\mathbf{S}^r_{e^{(N)}}$ in the presence of the reservoir, as it would give rise to a discontinuity of the atomic excitation wave function (*i.e.*, $e(x_1, \cdots, x_{N-1})$ is not continuous at the boundary between any two adjacent Region $j+1$ and j for $j = 1, \cdots, N$). Note for the reservoir-modified bound state solution, neither the interacting eigenstates for the restricted system variables nor the transmission coefficient can be described by a simple frequency renormalization of the results in the reservoir-free case (see Eqs. (19), (A28), and (A29) in Ref. [21]). Furthermore, the reservoir-modified N-photon hybrid states can be determined through a similar procedure, and it is also found that the hybrid states can not be obtained by a frequency renormalization of the results in the reservoir-free case. Thus, the existence of the reservoir-modified bound state and the hybrid states make the reduced Hamiltonian approach invalid in the N-photon case.

4.5 Breakdown of Non-Hermitian Hamiltonian from Scattering Matrix

Here we examine the restricted scattering matrix to check the validity of non-Hermitian Hamiltonian description using the two-photon case as an example. By construction, $|D_K\rangle$ is a scattering eigenstate of the restricted scattering matrix $\mathbf{S}^r_{e^{(2)}}$ such that $\mathbf{S}^r_{e^{(2)}}|D_K\rangle = \widetilde{t}^{(2)}_K|D_K\rangle$. One can directly check the orthogonality relation $\langle D_{K'}|D_K\rangle = \delta(K-K')2\sqrt{\nu\nu'}/(\nu+\nu')$, where ν and ν' are determined by K and K', respectively. In Ref. [85], it has been confirmed that the reservoir-free two-photon bound state $|B_K\rangle$ is orthogonal to the two-photon plane-wave state $|W_{k,p}\rangle$, *i.e.*, $\langle W_{k,p}|B_K\rangle = 0\ \forall k$, p, and K. In contrast, when the excitable reservoir is present, we find that

$$\langle W_{k,p}|D_K\rangle = \sqrt{\frac{\kappa^3\nu}{2\pi}}\frac{(\nu-1)\Delta}{\sqrt{\Delta^2+\frac{\kappa^2}{4}}\left(\Delta^2+\frac{\kappa^2\nu^2}{4}\right)}\delta(K-(k+p)). \tag{4.12}$$

(Note that $|W_{k,p}\rangle$ has the same form for both the reservoir-free case and the excitable-reservoir case, as described above.) That is, the reservoir-modified bound state $|D_K\rangle$ and the plane-wave state $|W_{k,p}\rangle$ are degenerate and not orthogonal when the two states have the same energy *i.e.,* $\langle W_{k,p}|D_K\rangle \neq 0$ when $K = k + p$. The fact that the two states have a non-zero overlap at the same energy indicates the two states can transform to each other. The physical reason is that, due to the existence of the scatterers in the excitable reservoir, when a waveguided photon in either state leaks into the reservoir, the photon has a non-zero amplitude to scatter back to the waveguide. The re-entrant photon can form a different state with the remaining photon.

Thus, the restricted out-state of an arbitrary in-state can be straightforwardly obtained by decomposing the in-state into linear superposition of $|W_{k,p}\rangle$ and $|D_K\rangle$, and followed by operating the scattering matrix on each eigenstate. To this end, we investigate the explicit form of $\mathbf{S}^r_{e^{(2)}}$ under the bases of its eigenstates, $|W_{k,p}\rangle$ and $|D_K\rangle$, which, by imposing eigen-relations $\mathbf{S}^r_{e^{(2)}}|W_{k,p}\rangle = \bar{t}_k\bar{t}_p|W_{k,p}\rangle$ and $\mathbf{S}^r_{e^{(2)}}|D_K\rangle = \widetilde{t}^{(2)}_K|D_K\rangle$, after some algebra, can be shown to have the following form

$$\begin{aligned}\mathbf{S}^r_{e^{(2)}} =& \sum_{k\leq p} \bar{t}_k\bar{t}_p|W_{k,p}\rangle\langle W_{k,p}| + \sum_K \widetilde{t}^{(2)}_K|B_K\rangle\langle B_K| \\ &+ \sum_{k\leq p}\sum_K \sqrt{\frac{\kappa^3}{8\pi}}\frac{(\nu^2-1)\Delta}{\sqrt{\Delta^2+\frac{\kappa^2}{4}}\left(\Delta^2+\frac{\kappa^2\nu^2}{4}\right)}(\widetilde{t}^{(2)}_K - \bar{t}_k\bar{t}_p)\delta(K-k-p)|W_{k,p}\rangle\langle B_K|,\end{aligned} \tag{4.13}$$

where $\Delta_{1,2} = (k_{1,2} - p_{1,2})/2$. The first term describes the transmission of uncorrelated two-photon states, while second and third terms describe the transmission of correlated states. We note that the off-diagonal term that maps the correlated state $|B_K\rangle$ to uncorrelated state $|W_{k,p}\rangle$. Furthermore, it can be straightforwardly shown that $\mathbf{S}^r_{e^{(2)}}\mathbf{S}^{r\ \dagger}_{e^{(2)}} \neq 1$, indicating that $\mathbf{S}^r_{e^{(2)}}$ is not unitary. When the external reservoir is present, the resulting photon loss leads to a non-unitary property as the total photonic flux in the waveguide is not conserved

and decreased (i.e., transmission coefficients, $|\bar{t}'_k\bar{t}'_p|^2$, $|\bar{t}_k\bar{t}_p|^2$, $|\bar{t}'^{(2)}_K|^2$, and $|\widetilde{t}^{(2)}_K|^2 < 1$). The properties of the restricted scattering matrix for each scenario are summarized in Table 4.1.

Table 4.1: Properties of restricted scattering matrix $\mathbf{S}^r_{e^{(2)}}$ in the $\{|W_{k,p}\rangle, |B_K\rangle\}$ bases.

Scenarios	Diagonal	Unitary
reservoir-free	$\surd$	$\surd$
non-excitable	$\surd$	$\times$
excitable	$\times$	$\times$

To gain deeper insights, we further apply the Markovian and non-Markovian density matrix approach to the presented material loss, and summarize the results in Appendix C.

4.6 Weak-reservoir Condition

For scenarios wherein the material loss is weak, we derive the condition such that the reduced Hamiltonian approach is approximately valid for the multi-photon case. This is called the weak-reservoir condition.

The weak-reservoir condition requires: the system-reservoir coupling $\bar{\eta}$ and the secondary scattering strength $\bar{\beta}$ are both weak enough, *i.e.*, $\bar{\eta}, \bar{\beta} \ll \Omega, \Gamma$; and the photon-reservoir detuning $\bar{\delta}$ is much larger than the photon-atom interaction strength, *i.e.*, $\bar{\delta} \gg \Gamma/2$. When such a condition is fulfilled, two-photon case as an example, the interacting eigenstates for the restricted system variables for the reservoir-modified bound state solution (Fig. 4.5) reduces to the functional forms with a frequency renormalization $\Omega \to \bar{\Omega} = \Omega + \Delta_M - i\gamma_M$ in the reservoir-free case. Thus, the solutions for both the plane-wave state (Fig. 4.3) and the bound state are renormalized by a frequency renormalization ($\Omega \to \bar{\Omega}$). As a result, the reduced Hamiltonian approach remains valid for the two-photon case when the weak-reservoir

condition is satisfied. The same conclusions apply to the two-photon and arbitrary N-photon two-mode cases.

4.7 Summary and Outlook

In essentially all quantum optical scenarios, photonic dissipation results from both photonic scattering loss (coupling with a non-excitable reservoir) and material loss (coupling with an excitable reservoir). For photonic scattering loss, it has been shown that, for all input states, the effects can be incorporated by adding an imaginary part $-i\gamma_S$ in the renormalized transition frequency (γ_S is the photonic scattering loss rate) [60]. Thus, when the weak-reservoir condition is satisfied, to take into account the effects of both scattering loss and material loss, the reduced Hamiltonian approach is valid via the frequency renormalization $\Omega \to \Omega + \Delta_M - i(\gamma_M + \gamma_S)$. As a coherent state is a linear superposition of Fock states, the reduced Hamiltonian approach is also valid when the input is a coherent state under the weak-reservoir condition. Moreover, by employing the explicit photon-cavity interactions, and applying the same approach outlined above, it can be shown that the reduced Hamiltonian approach is also valid in the presence of cavity dissipations. That is, the dissipation rate γ_M due to the reservoir can be measured by a single-photon scattering experiment (*e.g.*, a transmission measurement); the resulting reduced Hamiltonian is then valid for all quantized optical input.

Chapter 5

Dissipation-induced Photonic Correlation Transition

5.1 Introduction

One of the central goals in quantum nanophotonics is to generate photonic entanglement via atom-mediated photon-photon interactions [20, 21, 38, 86]. In general, dissipations are considered deleterious that undermine photonic entanglement and impair photon transport (*e.g.,* total transmissions and reflections in one-dimensional systems). On the other hand, from the perspective of microscopic scattering, photonic dissipations are manifestations of photon leakages from the system of interest to the external environment. For initially entangled photons in the system, the entanglement should persist even after some of the photons are scattered out of the system (perhaps shared with other degrees of freedom in the environment). Conventionally, it is convenient to discuss the dynamics of the states that are restricted to the system only, and phenomenologically parametrize the effects of photon

leakages by a set of few parameters. By doing so, it is obvious that photon transport is degraded by the dissipations. However, it is not clear, as *a priori*, how photonic entanglement is affected by dissipations. In this article, we computationally study the effects of dissipations on the photonic entanglement and the photon transport in waveguide QED systems. We confirm that when the dissipation increases, the transport metrics quickly degrade and exhibit no correlation signatures. Nonetheless, our results also reveal that even in this dissipative regime, the photons are still correlated (bunched or antibunched). That is, the correlation persists even when the transport metrics are described by a single-photon picture. Moreover, by varying the dissipations, the photon correlation can have a crossover from bunching to antibunching.

5.2 System and Hamiltonian

To begin with, we describe the waveguide QED systems of interest. We focus on the configuration that is one fundamentally building block for more complicated systems: Fig. 5.1, a single two-level atom coupled to a single-mode photonic waveguide. A two-photon Fock state $|2\rangle$ is injected into the waveguide from the left and, after scattering, the photonic

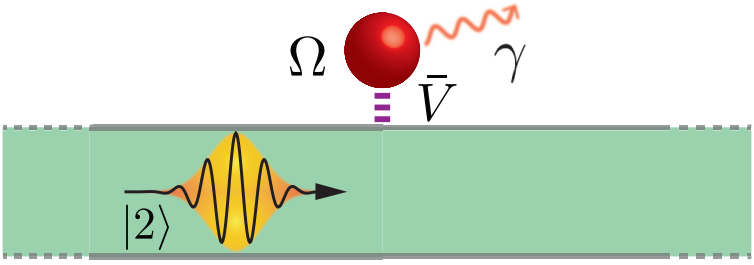

Figure 5.1: Schematics of the waveguide QED system. A two-level atom (represented by a red sphere) is coupled to a one-dimensional single-mode photonic waveguide. A two-photon Fock state $|2\rangle$ is incoming from the left.

correlation is numerically determined. The Hamiltonian is described by

$$\begin{aligned}\frac{H}{\hbar} = \int dx \Big(& c_R^\dagger(x)(-iv_g\partial_x)c_R(x) + c_L^\dagger(x)(iv_g\partial_x)c_L(x) \\ & + \bar{V}\delta(x)\left[(c_R^\dagger(x) + c_L^\dagger(x))a_g^\dagger a_e + a_e^\dagger a_g(c_R(x) + c_L(x))\right]\Big) \\ & + (\omega_e - i\gamma)a_e^\dagger a_e + \omega_g a_g^\dagger a_g,\end{aligned} \tag{5.1}$$

where notations are defined the same as in Eq. (2.1). γ is the atomic dissipation rate, where only the effects of photonic scattering loss is considered [60] while the material loss is neglected [84]. Such a scenario applies to a common setup in cold Rydberg atomic gas [38, 87, 88] where photons are scattered off the Rydberg blockade into the three-dimensional free space. Notably, such a scenario can be further applied whenever the dissipation mechanism from first-principle is aligned with that describe by Weisskopf Wigner theory [76]. The two-photon state is

$$\begin{aligned}|\Phi(t)\rangle = \Big(& \int dx \sum_{j=R,L} e_j(x,t)c_j^\dagger(x)e^{-i\omega_e t}a_e^\dagger a_g \\ & + \iint dx_1 dx_2 \sum_{j,l=R,L} \phi_{jl}(x_1,x_2,t)e^{-i\omega_g t}\frac{c_j^\dagger(x_1)c_l^\dagger(x_2)}{\sqrt{2}}\Big)|\varnothing\rangle.\end{aligned} \tag{5.2}$$

$|\varnothing\rangle$ is the vacuum state that has no waveguided photons, and the atom is in the ground state. $e_{R(L)}$ denotes the single-photon probability amplitude wherein one photon is absorbed by the atom and the other waveguided photon is moving to the right (left). ϕ_{RL} denotes the two-photon probability amplitude for the RL branch wherein one photon is moving to the right and the other to the left. ϕ_{RR}, ϕ_{LR}, and ϕ_{LL} are similarly defined.

To numerically determine the two-photon transport and the correlations, a two-photon Fock state is injected from the left. The incoming Fock state is an uncorrelated two-photon product state wherein each photon is resonant with the atom, and has a Gaussian waveform

$\phi(x) = 1/(2\pi\sigma^2)^{1/4} \exp[-(x-x_o)^2/4\sigma^2 + i\omega_o x/v_g]$ ($\omega_o = \Omega$ is the center frequency). The numerical initial condition is $\phi_{RR} = \phi_{in} = \phi(x_1)\phi(x_2)$ at $t = 0$. Here, $\sigma\Gamma/v_g = 15$ so that the photon has a narrow bandwidth $\Gamma/30$ ($x_o \approx -3.6\sigma$ is the initial position of the photon, and has no direct relevance of numerical results). The equations of motion are obtained from the Schrödinger equation $i\hbar\partial_t|\Phi\rangle = H|\Phi\rangle$, which are numerically evolved to obtain the full spatiotemporal dynamics of the system [39]. In particular, such a numerical procedure yields, after scattering, the two-photon transmitted (ϕ_{RR}), two-photon reflected (ϕ_{LL}), and one-transmitted-one-reflected (ϕ_{RL} and ϕ_{LR}) wave functions, which provide complete information on the two-photon transport and correlations. We note that such an approach is also applicable to a weak coherent state input [39].

5.3 Transport Metrics

After scattering, the photon transport properties are characterized by three quantities, T_2 (both photons are transmitted), R_2 (both reflected), and TR (one transmitted, the other reflected), respectively. T_2 is numerically evaluated by the two-photon transmitted flux $\iint dx_1 dx_2 |\phi_{RR}(x_1, x_2)|^2$. R_2 and TR are similarly defined. We visualize the transport properties by representing the triplet (T_2, R_2, TR) as a point in a three-dimensional plot (Fig. 5.2(a)). When γ varies, the triplet traces out a curve $\mathcal{C}$ (blue curve, the arrow indicates the direction of the increasing γ). To obtain deeper insight on the photon correlation, we also plot the trace of the triplet based upon the single-photon picture. From the single-photon picture, the two-photon transport is the joint probability of the transports of two independent photons. Specifically, the uncorrelated two-photon transport is given by $T_2 = T_1^2, R_2 = R_1^2, TR = 2T_1R_1$, where T_1 and R_1 are single-photon transmission and reflection coefficients, respectively $(T_1, R_1) = ((\gamma/\Gamma)^2/(1+\gamma/\Gamma)^2, 1/(1+\gamma/\Gamma)^2)$. When varying γ, the triplet of the uncorrelated two-photon transport traces out a curve $\mathcal{C}'$ (red curve). It can be shown that $\mathcal{C}'$ lies on a

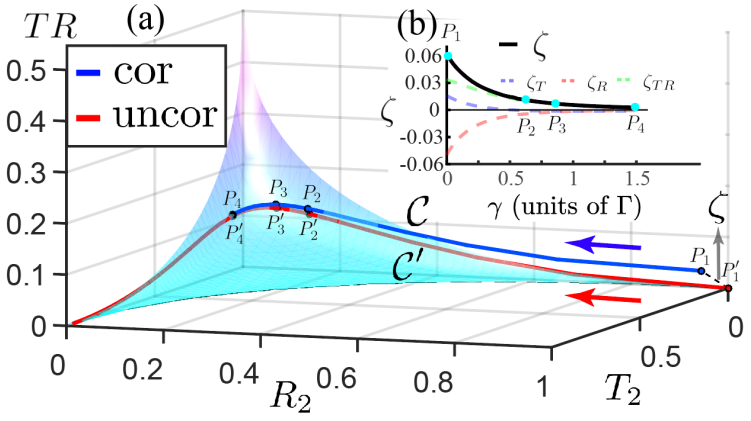

Figure 5.2: Visualization of the two-photon transport metrics in the dissipative single-atom case. (a) Trajectory for correlated ($\mathcal{C}$) and uncorrelated ($\mathcal{C}'$) transport properties when varying γ. The points P_1, P_2, P_3, and P_4 on $\mathcal{C}$ represent the cases when $\gamma/\Gamma = 0,\ 0.62,\ 0.85,$ and 1.5, respectively. The primed points denote the corresponding points on $\mathcal{C}'$. (b) ζ, ζ_T, ζ_R and ζ_{TR} as a function of γ.

surface because the constraint $\sqrt{T_2} + \sqrt{R_2} + \sqrt{2TR} = 1$ holds $\forall\ \gamma/\Gamma$ (noting that $\mathcal{C}$ does not lie on this surface). By definition, any point representing a scattering process that does not lie on $\mathcal{C}'$ indicates a two-photon correlation.

For a given γ, the transport properties of the correlated and uncorrelated systems are represented by P and P', respectively. For example, P_1 and P'_1 describe the case for $\gamma = 0$. We now define the distance ζ between the two curves as the distance of two corresponding point for the same γ, $\zeta \equiv \sqrt{\zeta_T^2 + \zeta_R^2 + \zeta_{TR}^2}$, where $\zeta_T = T_{2,cor} - T_{2,uncor}$, and ζ_R, ζ_{TR} are similarly defined. Fig. 5.2(b) plots ζ as a function of γ. As expected, ζ monotonically decreases and approaches to zero rapidly when γ increases. For example, when $\gamma = 1.5\Gamma$, ζ degrades to only 2.7×10^{-3}. Thus, for large dissipations, the two-photon transport metrics essentially exhibit no correlation signatures, and indeed can be predicted from a single-photon picture.

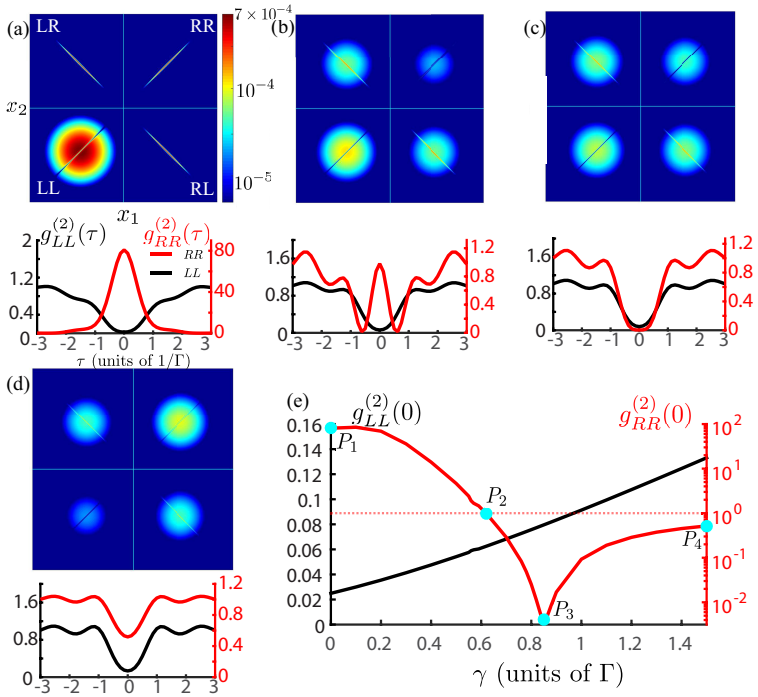

Figure 5.3: Numerical results of the photonic correlations in the dissipative single-atom case. (a) Upper: probability density of the scattered photons for $\gamma = 0$. (a) Lower: $g^{(2)}(\tau)$ of the RR (red curve, right) and the LL (black curve, left) branches for $\gamma = 0$. (b) $\gamma = 0.62\Gamma$. (c) $\gamma = 0.85\Gamma$. (d) $\gamma = 1.5\Gamma$. (e) $g^{(2)}_{RR}(0)$ (red curve, right) and $g^{(2)}_{LL}(0)$ (black curve, left) for varying γ. The P points correspond to the cases in (a)-(d), respectively, which are the same as in Fig. 5.2.

5.4 Correlation Transition

Here, we study the effects of dissipations on photonic correlation by examining the second-order correlation function $g^{(2)}(\tau)$. Numerically, $g^{(2)}(\tau) = |\phi(x_m, x_m+v_g\tau)|^2 / \int dx' |\phi(x', x_m)|^2 \int dx' |\phi(x', x_m+v_g\tau)|^2$, where x_m is a reference position [39]. In Fig. 5.3(a), we plot the probability density ($|\phi|^2$) of the scattered photons for the $\gamma = 0$ case. $|\phi_{RR}|^2$ for two transmitted photons in Quadrant I (RR branch) is localized along $x_1 = x_2$, indicating photonic bunching because two photons tend to be collocated at the same spatial point. We find numerically that $T_{2,cor} \approx 1.6\%$ while the single-photon picture gives $T_{2,uncor} = 0$. The numerically computed $g^{(2)}_{RR}(\tau)$ (red curve in Fig. 5.3(a)) is peaked at $\tau = 0$ ($g^{(2)}_{RR}(0) \approx 85 \gg 1$), confirming the bunching behavior. In Quadrant III, $|\phi_{LL}|^2$ for two reflected photons (LL branch) is depleted along $x_1 = x_2$, and $g^{(2)}_{LL}(\tau)$ has a dip at $\tau = 0$ (black curve, $g^{(2)}_{LL}(0) \approx 0.025 \ll 1$), both of which confirm the antibunching phenomenon.

Table 5.1: Numerical metrics of scattered photons in RR and LL branches in the dissipative single-atom case. Abbreviations represent, S: photon statistics; A: antibunching; and B: bunching.

$\frac{\gamma}{\Gamma}$	$\zeta(\gamma)$	$T_{2,cor}(\%)$	$g^{(2)}_{RR}(0)$	S_{RR}	$R_{2,cor}(\%)$	$g^{(2)}_{LL}(0)$	S_{LL}
0	0.062	1.6	85	B	95	0.025	A
0.62	0.011	2.1	0.98	B	14	0.062	A
0.85	0.0071	4.3	0.0039	A	8.3	0.08	A
1.5	0.0027	12.7	0.51	A	2.5	0.13	A

We now examine the effects of dissipations by scanning γ in the range of $[0, 1.5\Gamma]$. We first focus on the RR branch. When γ increases, the two transmitted photons remain bunched while the bunching quality degrades as $g^{(2)}_{RR}(0)$ decreases. For example, when $\gamma \approx 0.62\Gamma$, $g^{(2)}_{RR}(\tau)$ still exhibits a peak at $\tau = 0$ and $g^{(2)}_{RR}(0) \approx 1$ (Fig. 5.3(b)). When γ is further increased to $\approx 0.85\Gamma$, the peak of $g^{(2)}_{RR}(\tau)$ at $\tau = 0$ disappears and a dip emerges, indicating

that the photon statistics has a crossover, and now exhibits a strong antibunching signature ($g^{(2)}_{RR}(0) \approx 0$, Fig. 5.3(c)). Two transmitted photons remain antibunched when γ is further increased throughout the scanning range while the antibunching quality degrades as $g^{(2)}_{RR}(0)$ elevates and approaches to 1. Figure 5.3(d) plots the results for the $\gamma = 1.5\Gamma$ case. For the LL branch, we find that two reflected photons remain antibunched throughout the scanning range so that no crossover occurs. Figure 5.3(e) plots $g^{(2)}_{RR}(0)$ and $g^{(2)}_{LL}(0)$ as a function of γ, and Table 5.1 provides further numerical metrics. Here, we emphasize that when the correlation transition occurs (Fig. 5.3(c)), the transport metric ζ already significantly degrades to 7.1×10^{-3}, essentially agreeing with the single-photon picture. Thus, the information of photonic correlation is beyond that of the transport metric. In addition, we note that in the dissipative regime (Fig. 5.3(b)-(d)), $|\phi_{RR}|^2$, $|\phi_{RL}|^2$, and $|\phi_{LR}|^2$ spread out to off-diagonal regions. Such a photonic halo effect has been reported in Ref. [68, 69].

5.5 Theoretical Explanation

Here we present a physical argument to account for the dissipation-induced correlation transition phenomenon. To demonstrate the physics, without loss of generality, we restrict the discussions in the even mode, where closed-form analytical results are readily established [85].

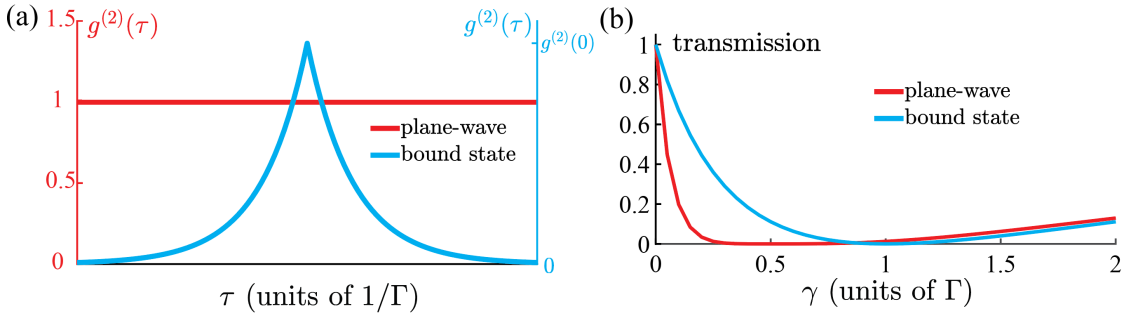

Figure 5.4: (a) $g^{(2)}(\tau)$ signatures for two-photon plane-wave (red, left) and bound states (blue, right). (b) Two-photon transmission for plane-wave and bound states.

It has been shown that a complete set of eigenstates in two-photon Hilbert space consists of two states, uncorrelated two-photon plane-wave state $|W_{k,p}\rangle$ and correlated two-photon bound state $|B_K\rangle$ [20]. Photon correlations are sharply manifest in second-order correlation function $g^{(2)}(\tau)$. As plotted in Fig. 5.4(a), $g^{(2)}(\tau)$ for $|W_{k,p}\rangle$ (red line, left) remains a constant cross the entire coherence range of interest, indicating that to detect one is independent from to detect the other. In contrast, $g^{(2)}(\tau)$ for $|B_K\rangle$ exhibits a sharp cusp near the origin (blue curve, right).

Notably, any two-photon state can be decomposed into such two states. Henceforth, the $g^{(2)}(\tau)$ behavior results from a combined one from two states. Specifically, when bound state contribution dominates, $g^{(2)}(\tau)$ should exhibit a center peak to manifest bunching statistics. When plane-wave contribution dominates, $g^{(2)}(\tau)$ may exhibit a dip to manifest antibunching statistics. Such a contribution can be inferred from the transmission amplitude metrics. In particular, for the resonant condition, given a dissipation rate γ, single-photon transmission amplitude is $(\gamma - \Gamma/2)/(\gamma + \Gamma/2)$ while the two-photon bound state transmission amplitude is $(\gamma - \Gamma)/(\gamma + \Gamma)$. The weight can be approximated by the two-photon transmission for plane-wave $(\gamma - \Gamma/2)^4/(\gamma + \Gamma/2)^4$ and that for bound state $(\gamma - \Gamma)^2/(\gamma + \Gamma)^2$, respectively. As plotted in Fig. 5.4(b), the bound state transmission dominates when $\gamma \lesssim 0.87\Gamma$ while the plane-wave transmission dominates when $\gamma \gtrsim 0.87\Gamma$. As a result, the photon statistics for transmitted photons undergoes a crossover from bunching to antibunching around $\gamma \approx 0.87\Gamma$, which qualitatively explains our numerical observations. The inconsistency here attributes to a finite-bandwidth effect of practical wave packets as the analysis is performed for single-frequency component. In conclusion, the induced correlation transition phenomenon can be explained by, varying dissipations can alter the weight of uncorrelated and correlated components to effectively change the photon correlations.

5.6 Summary and Outlook

In this chapter, we computationally study the dissipation-induced correlation transition in waveguide QED systems. The observation unveils a non-trivial quantum many-body effect driven by photon correlations. Such a phenomenon may provide a recipe for the design of fundamental nodes of quantum-optical networks in the presence of dissipations [34, 89], and could tremendously enable the manipulation of photon entanglement [90] via dissipation-engineering techniques [91, 92]. Moreover, our results may also provide significant insights for studies on the effects of dissipations on quantum many-body systems [93, 94].

Chapter 6

Deterministic Two-photon Controlled-phase Gate Proposal

6.1 Introduction

The crucial importance of a deterministic two-photon logic gate designing has been introduced in Chap. 1. Of particular interest is the two-photon controlled-phase gate (referred to as a CZ gate throughout this chapter [12]), which introduces a nonlinear π-phase shift only when both control and target qubits are one. There have been quite a few proposals in the literature. On one hand, the gate can be implemented in linear optics. Three representative schemes are: (1) the KLM scheme exploits a Mach-Zehnder interferometer (MZI) with an NS gate on each arm [13]. By performing measurement on an ancilla port of NS gate in a probabilistic manner, the two-photon Fock state is sign-flipped to give rise to the desired phase shift; (2) the cluster-state scheme initiates a multi-qubit entangled state through local in-neighbor interactions described by the Ising model [15, 16]. Then, by performing sequential

measurements, the cluster-state collapses to the desired two-qubit state in a probabilistic fashion as well; and (3) the quantum teleportation scheme transports the in-state through well-crafted quantum circuits. With proper single-qubit operations based on heralded information, a desired state can be obtained [17]. As a result of linear nature of instrument and a inherent nonlinear requirement of gate operation, linear optical implementations are doomed to be indeterministic. The accumulated faults become intractable when being integrated in a large scale.

On the other hand, a variety of schemes are proposed to take advantage of the inherent quantum nonlinearity to enable the desired π phase. For instance, Zheng et al. exploits the dipole transition in N-type four-level system to enable the operation [95]. Nonetheless, it requires a perfect quantum memory that is by far infeasible. Duan et al. decomposes the sign-flip step by properly injecting two extra strong laser pulses, which is barely scalable [96]. Gorshkov et al. maps the photonic state to spin wave and enable the π-phase shift using electron-electron interactions [97]. The scheme is yet too complicated to be controllable. Ralph et al. exploits the π phase of photonic molecule generations to enable a deterministic NS gate in KLM scheme while the scheme is too complicated to have practical significance [98]. Biswas et al. adopts the ab-initio system evolution using a hybrid photonic and atomic degrees of freedom. Nonetheless, the scheme may not be feasible due to a requirement of precise truncated control at a final evolution time [99].

To sum it up, a faithful, deterministic, and scalable CZ scheme is yet to be proposed. To this end, in this chapter, we present a CZ gate proposal by exploiting genuine few-photon nonlinearity in waveguide QED system.

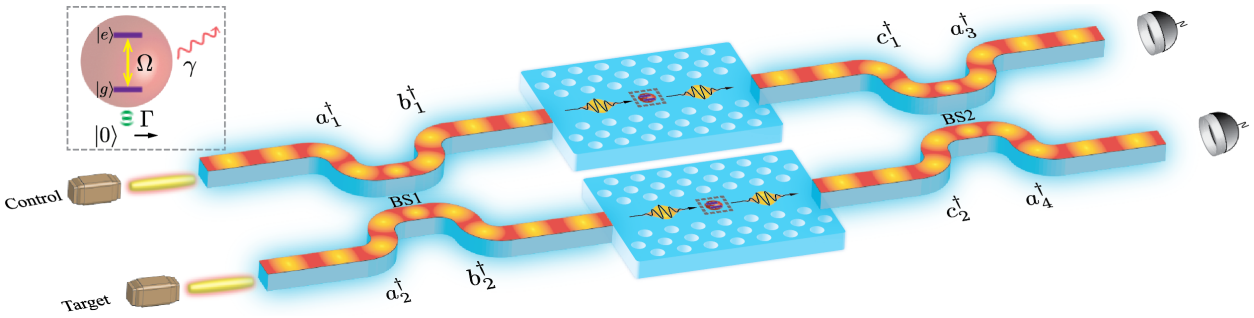

Figure 6.1: Schematic diagram of the CZ gate proposal, which is characterized by an MZI with chiral waveguide QED systems on both arms. Qubits $|0\rangle$ and $|1\rangle$ are different propagating modes supported in the waveguide. The two-level atom of transition frequency Ω is coupled to only the state $|0\rangle$. Γ and γ are atomic decay rates into the waveguided and non-waveguided modes, respectively. Photodetectors perform frequency-domain quantum tomography measurement.

6.2 Schematics

The system is schematically shown in Fig. 5.1, which is characterized by an MZI with chiral waveguide QED systems on both arms. *Chiral* represents that the atom only emits photons to the right. In particular, control and target qubits are frequency-bin and are injected from two respective input ports. Then two channels are interfered through a 50:50 beam splitter BS1, and are both coupled to chiral waveguide QED systems. Two parameters are of particular interest: atom-photon coupling strength Γ, and atomic transition frequency Ω. Here, binary qubits are encoded by photon frequency degrees of freedom, *i.e.*, $|0\rangle = |\omega_0\rangle, |1\rangle = |\omega_1\rangle$. Specifically, $\omega_0 = \Omega$ and ω_1 is arbitrary as long as $|\omega_1 - \Omega| \gg \Gamma$. Both qubits are both propagating modes supported in the waveguide. Thus, only qubit $|0\rangle$ is resonantly coupled to the atom while $|1\rangle$ is essentially decoupled. Notably, desired operations are performed through resonant atom-photon interactions. Next, outputs are mixed through another 50:50 beam splitter BS2, thereby giving rise to output ports of qubits 1 and 2, respectively.

The Hamiltonian to describe motion of $|0\rangle$ is given by

$$\begin{aligned}\frac{H_{|0\rangle}}{\hbar} = &\int dx c^\dagger(x)(-iv_g\partial_x)c(x) + \int dx V\delta(x)\left[c^\dagger(x)\sigma_- + \sigma_+ c(x)\right] \\ &+\omega_g a_g^\dagger a_g + (\omega_e - i\gamma)a_e^\dagger a_e,\end{aligned} \tag{6.1}$$

where $c^\dagger(x)$ ($c(x)$) is the operation to create (annihilate) a photon at position x in the chiral mode. Other notations are defined the same as in Eq. (2.1). The Hamiltonian to describe dynamics of $|1\rangle$ is given by

$$\frac{H_{|1\rangle}}{\hbar} = \int dx c^\dagger(x)(-iv_g\partial_x)c(x). \tag{6.2}$$

6.3 Operation Mechanism

CZ gate demands four operations on qubits, which are shown to be viable in the presented scheme. To begin with, BS1 and BS2 perform the following operator transformations.

$$\begin{aligned}a_1^\dagger =& \frac{b_2^\dagger - b_1^\dagger}{\sqrt{2}}, \quad a_2^\dagger = \frac{b_2^\dagger + b_1^\dagger}{\sqrt{2}}, \\ c_1^\dagger =& \frac{a_4^\dagger - a_3^\dagger}{\sqrt{2}}, \quad c_2^\dagger = \frac{a_4^\dagger + a_3^\dagger}{\sqrt{2}}.\end{aligned} \tag{6.3}$$

Here, it is worth noting that beam splitter operation bandwidth readily covers both frequency modes of qubit. Nonetheless, we show that the same beam splitter operation is performed on both $|\omega_0\rangle$ and $|\omega_1\rangle$. The reason is $|\lambda_0 - \lambda_1|$ can be adequately small so that both qubits are within the same operating bandwidth of beam splitter. Typically, the beam splitter operating bandwidth is $\sim$ 100 nm. Note that $|\omega_0 - \omega_1| \gg \Gamma$ is required to fulfill the Hamiltonian requirement. Then we estimate $|\lambda_0 - \lambda_1|$ under practical condition $v = 10^8 m \cdot s^{-1}, \lambda =$

$1.5\mu m, \Gamma = 1GHz, |\omega_0 - \omega_1| = 10\Gamma$. One has

$$\Delta\lambda = |\lambda_0 - \lambda_1| \approx 0.225nm \ll 100nm,$$

which apparently falls into the same operating bandwidth.

1. $|1\rangle_{a_1}|1\rangle_{a_2} \rightarrow |1\rangle_{a_3}|1\rangle_{a_4}$

   For the in-state $|\text{in}\rangle = |1\rangle_{a_1}|1\rangle_{a_2} = a^\dagger_{1,\omega_1}a^\dagger_{2,\omega_1}|\varnothing\rangle$, where $|\varnothing\rangle$ is photonic vacuum state. After BS1, the state turns into $\frac{1}{2}\left(b^{\dagger\,2}_{2,\omega_1} - b^{\dagger\,2}_{1,\omega_1}\right)|\varnothing\rangle$. Note that both photons undergo free propagations and do not interact with the atom so that $b^\dagger_{1,\omega_1} \rightarrow c^\dagger_{1,\omega_1}$, $b^\dagger_{2,\omega_1} \rightarrow c^\dagger_{2,\omega_1}$. Thus, out-state is $|\text{out}\rangle = \frac{1}{2}\left(c^{\dagger\,2}_{2,\omega_2} - c^{\dagger\,2}_{1,\omega_1}\right)|\varnothing\rangle = a^\dagger_{3,\omega_1}a^\dagger_{4,\omega_1}|\varnothing\rangle = |1\rangle_{a_3}|1\rangle_{a_4}$, which remains the same as the in-state.

2. $|0\rangle_{a_1}|1\rangle_{a_2} \rightarrow -|0\rangle_{a_3}|1\rangle_{a_4}$

   For the in-state $|\text{in}\rangle = |0\rangle_{a_1}|1\rangle_{a_2} = a^\dagger_{1,\omega_0}a^\dagger_{2,\omega_1}|\varnothing\rangle$. After BS1, the state turns into $\frac{1}{2}\left(b^\dagger_{2,\omega_0} - b^\dagger_{1,\omega_0}\right)\left(b^\dagger_{2,\omega_1} + b^\dagger_{1,\omega_1}\right)|\varnothing\rangle$. Note that $|\omega_1\rangle$ undergoes free propagations and do not interact with the atom so that $b^\dagger_{1,\omega_1} \rightarrow c^\dagger_{1,\omega_1}$, $b^\dagger_{2,\omega_1} \rightarrow c^\dagger_{2,\omega_1}$. In contrast, $|\omega_0\rangle$ interacts with the atom, which is characterized by the even-mode single-photon transmission amplitude [85]

   $$t_k = \frac{kv_g - \Omega - i\Gamma/2}{kv_g - \Omega + i\Gamma/2}. \tag{6.4}$$

   Thus, the resonant photon at $kv_g = \omega_0$ on both arms results in a transmission amplitude of -1. Thus, $b^\dagger_{1,\omega_0} \rightarrow -c^\dagger_{1,\omega_0}$, $b^\dagger_{2,\omega_0} \rightarrow -c^\dagger_{2,\omega_0}$. Thus, out-state is $|\text{out}\rangle = -\frac{1}{2}\left(c^\dagger_{2,\omega_0} - c^\dagger_{1,\omega_0}\right)\left(c^\dagger_{2,\omega_1} + c^\dagger_{1,\omega_1}\right)|\varnothing\rangle = -a^\dagger_{3,\omega_0}a^\dagger_{4,\omega_1}|\varnothing\rangle = -|0\rangle_{a_3}|1\rangle_{a_4}$, which acquires a π phase.

   This operation is referred to Operation 1 (O1) throughout this note because it is in nature a single-photon process.

3. $|1\rangle_{a_1}|0\rangle_{a_2} \rightarrow -|1\rangle_{a_3}|0\rangle_{a_4}$

   Similar to case 2.

4. $|0\rangle_{a_1}|0\rangle_{a_2} \rightarrow -|0\rangle_{a_3}|0\rangle_{a_4}$

   For the in-state $|\text{in}\rangle = |0\rangle_{a_1}|0\rangle_{a_2} = a^\dagger_{1,\omega_0} a^\dagger_{2,\omega_0}|\varnothing\rangle$. After BS1, the state turns into $\frac{1}{2}\left(b^{\dagger\,2}_{2,\omega_0} - b^{\dagger\,2}_{1,\omega_0}\right)|\varnothing\rangle$. When both photons are involved in the interactions, the transmission process should be analyzed in the two-photon Hilbert space, wherein a complete set includes two eigenstates, *i.e.*, plane-wave state $|W_{k,p}\rangle$ and bound state $|B_K\rangle$. Any incoming states can be orthogonally decomposed into such two states and the transmission of two states are fully described by transmission amplitudes. In particular, transmission of $|W_{k,p}\rangle$ is described by a product of two single-photon transmission amplitudes. When both photons are resonant with the atom, the plane-wave component has a transmission amplitude $t_k t_k = (-1)^2 = 1$, which does not give birth to any phase shift. The transmission amplitude of bound state component is described by

$$t_K^{(2)} = \frac{Kv_g - 2\Omega - i2\Gamma}{Kv_g - 2\Omega + i2\Gamma}, \tag{6.5}$$

   which is equal to -1 when both photons are resonant with the atom (*i.e.*, $Kv_g = 2\Omega$) so that $b^{\dagger\,2}_{1,\omega_0} \rightarrow -c^{\dagger\,2}_{1,\omega_0}$, $b^{\dagger\,2}_{2,\omega_0} \rightarrow -c^{\dagger\,2}_{2,\omega_0}$. Thus, out-state is $|\text{out}\rangle = -\frac{1}{2}\left(c^{\dagger\,2}_{2,\omega_0} - c^{\dagger\,2}_{1,\omega_0}\right)|\varnothing\rangle = -a^\dagger_{3,\omega_0} a^\dagger_{4,\omega_0}|\varnothing\rangle = -|0\rangle_{a_3}|0\rangle_{a_4}$, which acquires a π phase.

   This operation is referred to Operation 2 (O2) throughout as it is a genuine two-photon process.

As a result, the system passively performs the following unitary transformation on four two-qubit bases, $|00\rangle$, $|01\rangle$, $|10\rangle$, and $|11\rangle$,

$$U = \begin{bmatrix} -1 & & & \\ & -1 & & \\ & & -1 & \\ & & & 1 \end{bmatrix} = (-1) \times \begin{bmatrix} 1 & & & \\ & 1 & & \\ & & 1 & \\ & & & -1 \end{bmatrix}. \tag{6.6}$$

Obviously, the CZ gate is realized subject a trivial global phase π, which can be readily rectified using linear optical instruments.

6.4 Gate Demonstration

Here we demonstrate the π-phase in O1 and O2 by fully tracing out the spatio-temporal photon dynamics of an injected finite-bandwidth pulse. For O1, the incoming state is

$$\begin{aligned} |\chi_{\text{in}}\rangle &= \int dx \phi(x, t=0) c^\dagger(x) |\varnothing\rangle, \quad \text{where} \\ \phi(x, t=0) &= \frac{1}{(2\pi\sigma)^{1/4}} e^{-\frac{(x-x_o)^2}{4\sigma^2} + ik_o x}, \end{aligned} \tag{6.7}$$

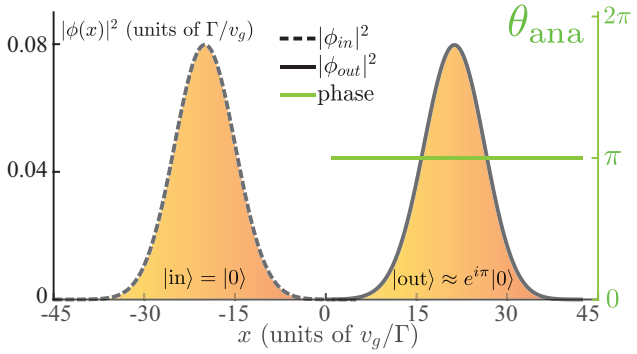

Figure 6.2: Analytical results of narrow-bandwidth ($\sigma\Gamma/v_g = 5$) Gaussian pulse evolution for O1 in the ideal case ($\delta = \gamma = 0$). In particular, a long Gaussian pulse ($\sigma = 5v_g/\Gamma$) is injected from left. The out-state wave function and phase shift are recorded.

where σ and x_o is the spatial width and initial position of the Gaussian pulse. k_o is the center wave vector that is resonant with the atom here ($\delta \equiv k_o v_g - \Omega = 0$). Here, we select a long Gaussian pulse ($\sigma = 5v_g/\Gamma$) with a narrow bandwidth $\Gamma/10$ because: first, Gaussian pulse of a long coherence time is typically adopted experimentally; and a narrow-bandwidth photon behavior mimics the single-frequency behavior, which may be well described by analytical results. By applying the ab-initio time evolution techniques in Ref. [100], the transmitted wave function in the out-state $|\chi_{\text{out}}\rangle$ is recorded. To acquire the phase shift, one performs the evolution twice, first obtaining the reference phase information $\phi_{\text{ref}}(x)$ in the absence of the atom (*i.e.*, $\Gamma = 0$), and the wave function $\phi(x)$ after interacting with the atom (*i.e.*, $\Gamma \neq 0$). The phase shift can be evaluated using

$$\theta \equiv \text{phase shift}(x) = \arg[\frac{\phi(x)}{\phi_{\text{ref}}(x)}]. \tag{6.8}$$

By doing so, the analytical result is obtained in Fig. 6.2. Apparently, the general envelope of transmitted wave (wave density represented by solid black curve) remains the same as the incoming wave (dashed black curve) while uniformly acquires a phase shift π (phase represented by green line, relative error $< 10^{-4}$). We further employ numerical tools to confirm the same result (not shown).

Here we investigate the O2 operation. The incoming state is an uncorrelated two-photon product state, described by

$$\begin{aligned} |\chi_{\text{in}}\rangle =& \iint dx_1 dx_2 \phi(x_1, x_2, t=0) \frac{1}{\sqrt{2}} c^\dagger(x_1) c^\dagger(x_2) |\varnothing\rangle, \quad \text{where} \\ \phi(x_1, x_2, t=0) =& \phi(x_1, t=0)\phi(x_2, t=0) \frac{1}{(2\pi\sigma)^{1/2}} e^{-\frac{(x_1-x_o)^2}{4\sigma^2} - \frac{(x_2-x_o)^2}{4\sigma^2} + ik_o(x_1+x_2)}. \end{aligned} \tag{6.9}$$

The parameter set of the pulse remains the same as O1. Following similar procedures as the single-photon case, the out-state and phase shift can obtained in Fig. 6.3. Specifically, the

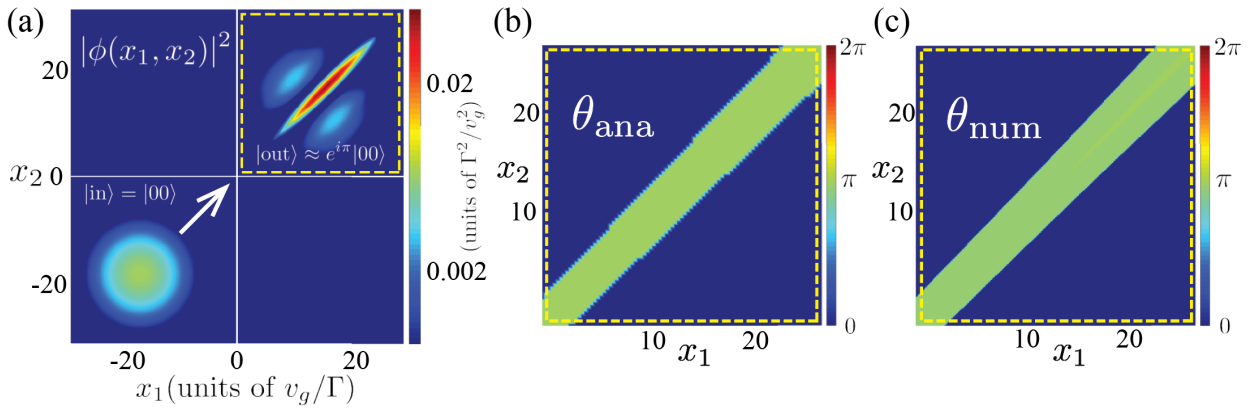

Figure 6.3: Analytical and numerical results of a narrow-bandwidth ($\sigma\Gamma/v_g = 5$) Gaussian pulse evolution for O2 in the ideal case ($\delta = \gamma = 0$). (a) Analytical results of the out-state wave function density. (b) Analytical results of the phase shift. (c) Numerical results of the phase shift. For instance, if the atomic spontaneous emission time is $1/\Gamma \approx 0.1$ns, the coherence length of the Gaussian pulse is $2\sigma/v_g \approx 1$ns.

wave function density and phase shift profile are shown in Fig. 6.3(a) and (b), respectively. As can be observed, the out-state wave function consists of two parts. The first part is the bound state part that is restricted along the diagonal line, which exhibits a clear phase shift π while the plane-wave component in the off-diagonal region exhibits zero phase shift. Both observations are consistent with our analysis in the previous section. Further numerical results in Fig. 6.3(c) confirm the analytical ones.

6.5 Gate Performance

6.5.1 Performance Metrics: Fidelity and Transmission

To quantitatively evaluate the gate performance, we now introduce two metrics, fidelity and transmission. Fidelity refers to the probability of success to detect a π phase of transmitted photon wave function in a single measurement. We now derive expression of fidelity and transmission for the two-photon process and the single-photon case can be defined

in a similar fashion. We assume the region $\mathcal{D}$ at which a π phase shift is measured, *i.e.*, $\mathcal{D} = \{(x_1, x_2)\Big||\text{phase shift}(x_1, x_2) - \pi| < \epsilon\}$. ϵ is the error tolerance, *e.g.*, $\epsilon = 0.01\pi$. Such a number does not affect the result because the numerically obtained π phase can be extremely precise (relative error $< 10^{-4}$ so that $\epsilon = 0.01\pi$ is a proper choice that does not affect the region of $\mathcal{D}$. Consider a two-photon out-state $|\chi_{\text{out}}\rangle = \int dx_1 dx_2 \phi(x_1, x_2) \frac{1}{\sqrt{2}} c^\dagger(x_1) c^\dagger(x_2) |\varnothing\rangle$, the fidelity should be equal to the integral of the probability density over $\mathcal{D}$

$$F \equiv \iint\limits_{\mathcal{D}} dx_1 dx_2 |\phi(x_1, x_2)|^2. \tag{6.10}$$

The fidelity shown in Fig. 6.2 and Fig. 6.3 is $> 99.99\%$ and $\approx 56.32\%$, respectively. On the other hand, in the presence of dissipations, photons may be scattered out of the system to the non-waveguided mode such that no photons trigger the photodetectors at all. The probability of a successful probing event can be described by the transmission T in the following

$$T = \iint dx_1 dx_2 |\phi(x_1, x_2)|^2. \tag{6.11}$$

It is worth noting that T is dependent on the dissipation rate γ solely. For the case shown in Fig. 6.2 and Fig. 6.3, transmission remains unity. To knock out the void detecting events, one can further define the normalized fidelity

$$F_{\text{norm}} \equiv \frac{\iint\limits_{\mathcal{D}} dx_1 dx_2 |\phi(x_1, x_2)|^2}{\iint dx_1 dx_2 |\phi(x_1, x_2)|^2}. \tag{6.12}$$

It is worth noting that F_{norm} is only examined in the presence of dissipations because $F_{\text{norm}} = F$ when $\gamma = 0$.

6.5.2 Necessary Condition

Necessary condition demands that a non-vanishing probability to detect π phase shift, that is, $F > 0$. We first present the necessary condition for O2, and O1 can be examined through a similar procedure. The acquired π phase shift is induced by bound state transmission amplitude $t_K^{(2)}$ in Eq. (6.5), on which discussions will be based. By taking into account the frequency detuning, $\delta \equiv Kv_g/2 - \Omega$, analytical prediction of phase shift is approximated by

$$\theta = \arg[t_K^{(2)}(\delta)] = -2\arctan[\frac{\Gamma}{\delta}], \tag{6.13}$$

as indicated by green dots in Fig. 6.4(a). Apparently, $\theta = \pi$ only when $\delta = 0$. To validate the analytical result, we send in the two-photon Gaussian pulse using the same parameter set in Eq. (6.9) and scan θ as a function of δ in a wide range of $[0, 3\Gamma]$. Here θ is evaluated at which the wave function attains the maximal. As represented by the green curve, θ essentially agrees with the analytical prediction. The slight inconsistency results from the interference of uncorrelated two-photon plane-wave states. As a result, the first necessary condition demands that $\delta = 0$.

Secondly, we investigate the requirement on γ. When the first necessary condition is fulfilled, the acquired phase is given by

$$\theta = \arg[t_K^{(2)}(\gamma)] = \begin{cases} \pi, & \gamma < \Gamma \\ 0, & \gamma \geq \Gamma \end{cases} \tag{6.14}$$

Consequently, to observe a π phase shift, the necessary condition demands that $\gamma < \Gamma$.

Then, to validate such a requirement, we numerically scan F, T, and F_{norm} as a function of γ in the range of $[0, 1.5\Gamma]$ using the same aforementioned two-photon Gaussian pulse,

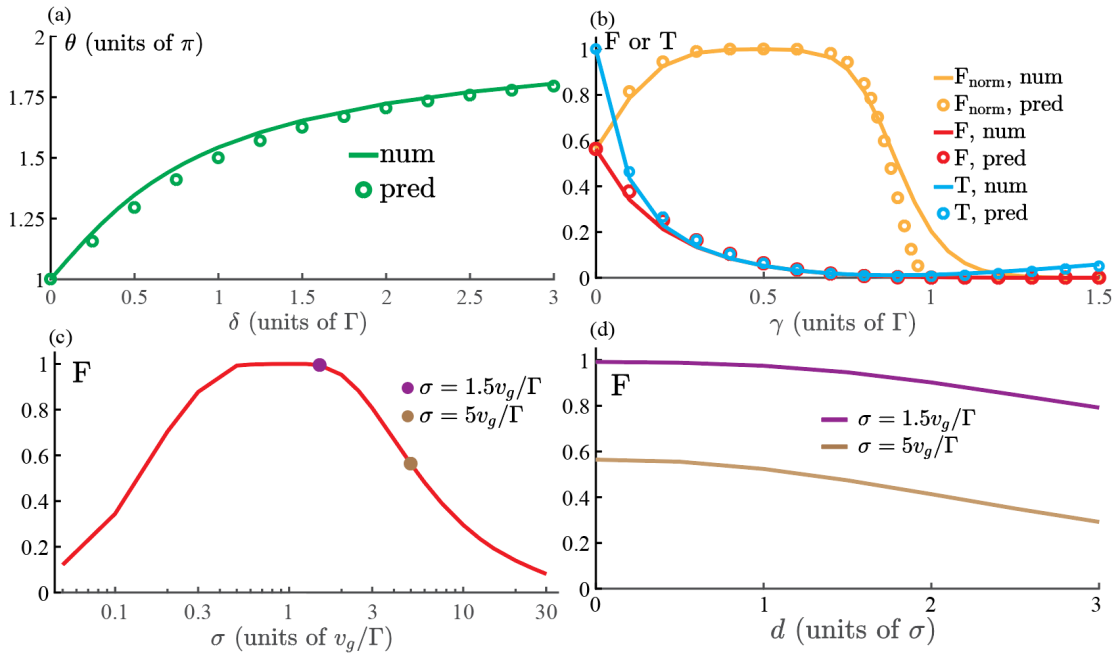

Figure 6.4: Gate performance for O2. (a) Phase shift as a function of δ when $\gamma = 0$. (b) Fidelity and transmission as a function of γ when $\delta = 0$. A narrow-bandwidth Gaussian modulation ($\sigma\Gamma/v_g = 5$) is adopted for (a) and (b). For example, if the atom has a spontaneous emission time $1/\Gamma \approx 0.1$ns, coherence time of the molecule is $2\sigma/v_g \approx 1$ns. (c) Fidelity as a function of σ. (d) Fidelity as a function of two-photon offset d.

represented by curves in Fig. 6.4(b). T (blue) significantly decreases as γ increases (when $\gamma < \Gamma$), and gradually increase as γ further increases (when $\gamma > \Gamma$) as a result of dissipation-induced transparency effect [101]. F (red curve) drops rapidly to almost zero as γ increases. Nonetheless, F_{norm} first elevates to almost unity and then remains unity when $\gamma < \Gamma$. As γ further increases, F_{norm} (orange curve) drops dramatically and approaches to zero when $\gamma \approx \Gamma$.

To understand the numerical result, we now perform analytical predictions. Note that the transmission can be orthogonally decomposed into the plane-wave and bound state parts separately, with component approximated by $F(0)$ and $1-F(0)$, respectively. In the presence of dissipations, the bound state transmission is $T_K(\gamma) = |t_K^{(2)}(\gamma)|^2 = \left(\frac{\gamma-\Gamma}{\gamma+\Gamma}\right)^2$ while that for the plane-wave state is $T_P(\gamma) = |t_k(\gamma)|^4 = \left(\frac{\gamma-\Gamma/2}{\gamma+\Gamma/2}\right)^4$. The overall transmission can thus be approximated by the linear superpositions of two parts

$$\begin{aligned} T(\gamma) \approx & F(0)T_K(\gamma) + [1-F(0)]T_P(\gamma) \\ = & F(0)\left(\frac{\gamma-\Gamma}{\gamma+\Gamma}\right)^2 + [1-F(0)]\left(\frac{\gamma-\Gamma/2}{\gamma+\Gamma/2}\right)^4. \end{aligned} \tag{6.15}$$

The fidelity can be further approximated by the bound state weight

$$\begin{aligned} F(\gamma) \approx & F(0)T_K(\gamma) \\ = & F(0)\left(\frac{\gamma-\Gamma}{\gamma+\Gamma}\right)^2, \end{aligned} \tag{6.16}$$

and normalized fidelity can be further approximated

$$\begin{aligned} F_{\text{norm}}(\gamma) = & \frac{F(\gamma)}{T(\gamma)} \\ = & \frac{F(0)\left(\frac{\gamma-\Gamma}{\gamma+\Gamma}\right)^2}{F(0)\left(\frac{\gamma-\Gamma}{\gamma+\Gamma}\right)^2 + [1-F(0)]\left(\frac{\gamma-\Gamma/2}{\gamma+\Gamma/2}\right)^4}. \end{aligned} \tag{6.17}$$

The analytical results are represented by dots in Fig. 6.4(b). T and F agree with numerical results very well (blue and red dots). F_{norm} (orange dots), however, is slightly inconsistent with numerical results around the threshold $\gamma \approx \Gamma$ due to edge effect.

Likewise, by performing a similar analysis, the necessary condition for O1 demands. $\delta = 0, \gamma < \Gamma/2$. To summarize the necessary condition for O1 and O2, one demands

$$\begin{aligned} \delta =& 0, \\ \gamma <& \Gamma/2. \end{aligned} \tag{6.18}$$

6.5.3 Effects of Finite Bandwidth and Two-photon Offset

Any practical pulse has a finite bandwidth and may affect the gate performance. Also, when two photons are not well synchronized due to imperfections of photon synchronizing techniques, the emerging two-photon offset may also degrade gate performance.

Here we perform numerical investigations of fidelity as a function of varying photon width σ in a wide range of $[0.05v_g/\Gamma, 30v_g/\Gamma]$. As shown in Fig. 6.4(c), F asymptotically approaches 0 in both the long- and short- Gaussian limit. In the long-Gaussian limit, the two-photon component is dominated by the plane-wave state to yield a vanishing fidelity. In the short-Gaussian limit, the off-resonance component dominates to yield a vanishing fidelity. Nonetheless, a high fidelity ($F \gtrsim 0.99$) is achieved when $\sigma \in [0.5v_g/\Gamma, 1.5v_g/\Gamma]$. That is, the optimal fidelity is achieved when the photon bandwidth matches the atom-photon interaction bandwidth.

Next we scan the fidelity by scanning two-photon offset d in a wide range of $[0, 3\sigma]$, wherein the choice 3σ guarantees that two Gaussian wave packet is utterly distinguishable based

on the Rayleigh criterion in diffraction limit analysis. The investigation is performed in the ideal case ($\delta = 0, \gamma = 0$) for long ($\sigma = 5v_g/\Gamma$) and middle ($\sigma = 1.5v_g/\Gamma$) Gaussian pulses, respectively, as plotted in Fig. 6.4(d). Specifically, F monotonically decreases when d increases due to an increasing off-diagonal plane-wave component contribution. Nonetheless, the middle pulse yields a high fidelity even in the presence of d. In particular, when $d = 3\sigma$, $F \approx 79.19\%$ for the middle Gaussian pulse while $F \approx 29.18\%$ for the long Gaussian pulse.

6.6 Chiral-coupling Technique

Here, we introduce possible implementations of phase gate by embedding a single quantum emitter (*e.g.*, a quantum dot) at the chiral point in a photonic crystal waveguide. That is, the atom only emits to the right-propagating electrical field so that the incoming photon can not be backscattered at the chiral point. Such a chiral coupling can be realized by two underlying mechanisms. First, at the boundary of two materials of different topological number, edge mode must exist in the photonic bandgap as a result of topology protection. One essential feature of the edge mode is that unidirectional propagating mode is supported solely where light automatically contours the impurities without backscattering [102]. Designing and implementing topological systems are technically challenging in general.

Henceforth, we seek for an alternative implementation through chiral coupling techniques [103, 104]. That is, at special locations in the photonic crystal waveguide, local transversal polarization of EM field is locked to its propagating direction (transversal spin-momentum lock, here transversal spin is the same as helicity degree of freedom in particle physics [105]). The dipole transition is also required to be polarization-selective (transversal spin-emission lock). Thus, by combining two locking mechanisms, the propagation-direction-dependent emission can be achieved, thus laying out the underlying mechanism of chiral coupling.

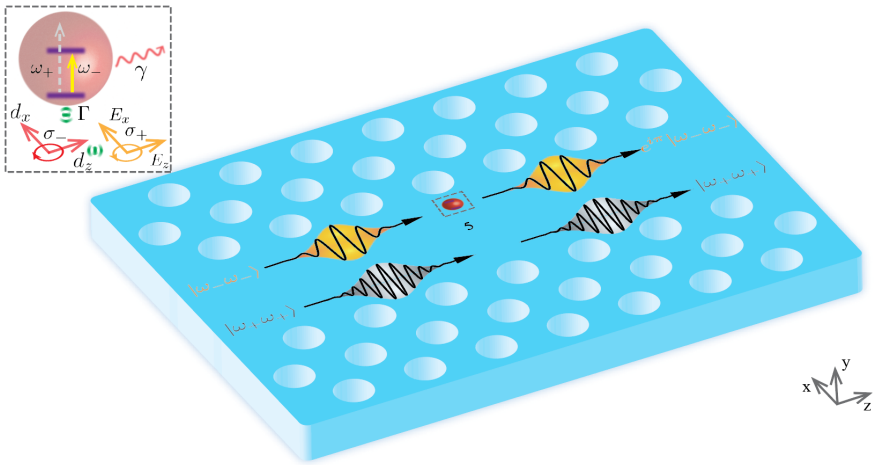

Figure 6.5: Schematic diagram of one possible experimental implementation, which includes three parts. The first part is the implementation of CZ gate. A polarization-dependent dipole emitter is embedded at the chiral point in a two-way (no chirality is required) photonic crystal waveguide. $\sigma_\pm$ denote the helicity of circular polarization. ω_- and ω_+ denote photon frequency of $|0\rangle$ and $|1\rangle$, respectively. Γ and γ are atomic decay rates into waveguided and non-waveguided modes, respectively. y is quantization axis. d_x and d_z is the dipole moment amplitude (omit the common phase factor of dipole oscillation $e^{-i\omega_- t}$ information, but includes the relative phase difference between z and x directions). E_x and E_z are the electrical field amplitude (omit the common phase factor of wave propagation $e^{i(\pm k_z z-\omega t)}$ information, but includes the relative phase difference between z and x directions) at which the dipole emitter is embedded. Photons are injected from $-z$ direction.

Here we elaborate the requirement of EM field at the chiral embedded point, as schematically shown in Fig. 6.5. The photon frequency degree of freedom is exploited as qubit. The notations are clarified in the caption. E-field has continuous translational symmetry along y-axis, that is, y is the quantization axis. E-field $\vec{E}_R$ denotes the amplitude for the right-propagating mode from $-z$ to $+z$. If E_z carries an oscillator factor $e^{-i\omega t}$, E_x should advance a $\pi/2$ phase (corresponds to the phase $e^{-i(\omega t+\pi/2)}$) so that $E_x = iE_z$. That is

$$\vec{E}_R = E_z\vec{e}_z + E_x\vec{e}_x = E_o\vec{e}_z - iE_o\vec{e}_x, \tag{6.19}$$

where E_o is the magnitude of amplitude for both directions. $\vec{e}_x$ and $\vec{e}_z$ denote unit vectors along x- and z- directions, respectively. Here, right-propagating E-field is σ_+-polarized. By invoking the time-reversal symmetry ($\vec{E}_R = \vec{E}_L^*$ where $*$ denotes the complex conjugate), one can write down other E-fields for the left-propagating mode

$$\vec{E}_L = E_o\vec{e}_z + iE_o\vec{e}_x. \tag{6.20}$$

That is, the left-moving photon has an opposite σ_+ transversal polarization. The phenomenon that counterpropagating photons have different polarization is called spin-momentum lock. The emitter is polarization-selective (*e.g.*, by imposing B-field in the quantization axis to induce the Zeeman split), whose dipole moment expressed as

$$\vec{d}_- = d_z\vec{e}_z + id_x\vec{e}_x = d_o\vec{e}_z + id_o\vec{e}_x, \tag{6.21}$$

where d_o is the magnitude of dipole moment. Note that $\vec{d}_-$ is σ_--polarized and the transition frequency for $\vec{d}_-$ is ω_-. Here we examine the coupling for the ω_- E-field with admissible

dipole transitions in the following

$$\begin{aligned} V_R &\propto \vec{E}_R \cdot \vec{d}_- = 2E_{o_1} d_o \neq 0, \\ V_L &\propto \vec{E}_L \cdot \vec{d}_- = 0. \end{aligned} \tag{6.22}$$

Here, $V_{R/L}$ denotes the coupling strength for the right/left-moving photon, and other notations are similarly defined. By defining the frequency-bin qubit as follows

$$\begin{aligned} |0\rangle =& |\omega_-\rangle, \\ |1\rangle =& |\omega_+\rangle, \end{aligned} \tag{6.23}$$

the chiral coupling condition is enabled.

6.7 Summary and Outlook

As a final remark, we now compare our proposal with those discussed in the introduction part. To gain deeper insights, we adopt seven metrics to evaluate gate performance: deterministic nature, fidelity, architecture complexity, requirement of additional pumping or driving, feasibility, requirement of sequential control, one-way property. Specifically, the deterministic nature describes whether measurement needs to be performed. The fidelity describes how reliable a single operation can yield a correct result. The architecture complexity characterizes the apparatus variety and accessibility. Generally speaking, schemes can be passive or active depending on whether the operation requires additional pumping or driving techniques. A passive device is of course preferred. Moreover, some schemes do require sequential control of optical pulses in distinct time windows, which may aggravate the difficulty of implementations. The one-way property is also preferred for photon-based designing because it may facilitate the

cascading of devices. Last but not least, feasibility characterizes the overall implementation difficulty using the current available techniques.

Table 6.1: Comparison of nine photon-based controlled-phase gate schemes.

Metrics	Baranger	Kimble	Lodahl	Lukin	Agarwal	KLM	Cluster	$\chi^{(3)}$	Shen
Deterministic	√	√	√	√	√	×	×	√	√
Faithful	√	√	×	√	√	√	√	√	√
Low-complexity	√	√	×	×	√	×	√	√	√
No-pumping/driving	√	×	×	×	√	√	√	×	√
Feasible	×	√	×	×	×	√	√	×	√
No sequential control	×	×	√	×	×	√	√	√	√
One-way	×	×	√	×	×	√	√	√	√

Chapter 7

Universal Quantum Computing Proposal

7.1 Introduction

In principle, a classic computer can be built up using a set of few logic gates only, *e.g.*, NAND or NOR gates. Analogously, for universal quantum computing task, three-qubit gate Toffoli gate solely suffices [12]. Nonetheless, it is even more technically challenging to introduce a three-qubit nonlinearity in a deterministic, faithful, and scalable manner than a two-qubit one. An alternative set typically includes three single-qubit logic gates, Hadamard, S ($\pi/4$ gate), and T ($\pi/8$ gate) gates, and one two-qubit gate (*e.g.*, CNOT or CZ). Interestingly, the S-gate is seemingly unnecessary because the same functionality can be realized by cascading two T gates. Nonetheless, for fault-tolerant quantum computing designing, it is an indispensible choice.

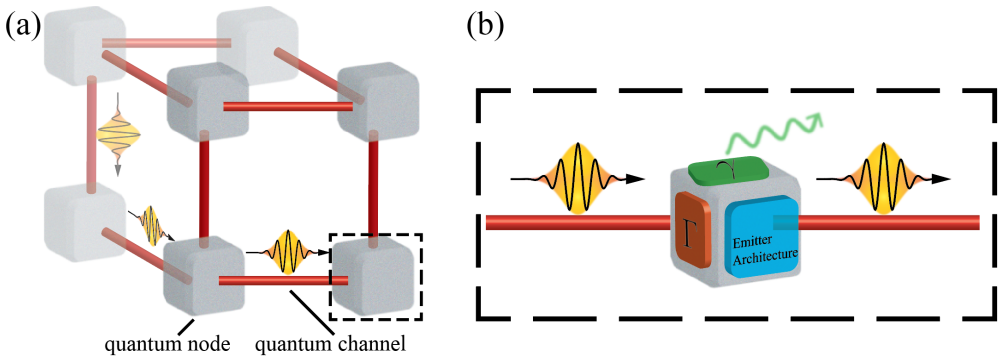

Figure 7.1: Schematic diagram of quantum internet blueprint, which is constituted by quantum nodes and quantum channels. (a) Global perspective. (b) Individual quantum node schematics, which processes photon qubits with functionalities characterized by the emitter architecture, photon-emitter coupling strength Γ, and photon loss rate γ.

For conventional atom-based implementations, desired operation can be performed by sending well-designed electromagnetic pulses in different frequency range (*e.g.*, optical pulse for quantum dots, N-V center, tapped ion, microwave pulse for superconducting qubit, and radiowave pulse for NMR systems). For photon-based one, as a result of linear nature, all three gates can be easily implemented using linear optical instruments (*i.e.*, beam splitters and phase shifters).

In the recent decade, the quantum internet blueprint is proposed [89]. As sketched in Fig. 7.1(a), information is encoded in flying qubits of individual photons, transported through quantum photonic channels, and processed by quantum atomic nodes. To this end, a complete set to perform quantum computing using atomic nodes has yet to be developed. As outlined in Fig. 7.1(b), each node is constituted by one photonic channel and a dipole emitter whose performance is characterized by the emitter architecture to determine the gate functionality, and effective Purcell factor (*i.e.*, atomic spontaneous emission rate into the waveguide Γ over that into the non-waveguided modes γ, Γ/γ) to determine the gate performance (*e.g.*, fidelity, transmission, efficiency, etc). As demonstrated by the CZ gate proposal presented in Chap. 6, the one-way chiral waveguide QED system may be a good platform. In this chapter, we

present the architecture of atomic nodes for the rest of the complete set, *i.e.*, Hadamard, S, and T gates.

7.2 Hadamard Gate Proposal

We propose a novel Hadamard gate scheme wherein binary qubits encoded by frequency degrees of freedom are accommodated in the same photonic channel to effectively increase spatial utility. In particular, the underlying mechanism is described by photonic frequency conversion in single-photon Raman scattering mediated by a Λ-type atom. To demonstrate its deterministic, high-fidelity, and high-efficiency nature, we showcase the gate operation using practical pulses of a finite bandwidth. We further quantitatively analyze the gate fidelity and efficiency metrics. Moreover, our results reveal that by tuning photon-emitter coupling and frequency detuning in a proper manner, an arbitrary unitary single-qubit rotation can be achieved. Finally, we further generalize the scheme to an N-type hyperfine atomic structure, which is more experimentally feasible. Detailed results are presented in Ref. [106].

7.2.1 Schematics

As schematically shown in Fig. 7.2, the system consists of a single-mode chiral waveguide coupled to two collocated and identical Λ-type atoms, and an incident single-photon Fock state from the left. Each Λ-type atom admits two dipole transitions, $1 \leftrightarrow 3$ and $2 \leftrightarrow 3$, of transition frequency Ω_1, Ω_2, and spontaneous decay rate into waveguided modes, Γ_1, Γ_2, respectively. Transition $1 \leftrightarrow 2$ is forbidden due to symmetry considerations. Two atoms are initialized at different ground states 1 and 2, respectively. γ denotes the spontaneous decay rate of atomic excited state 3 into non-waveguided modes, which manifests as intrinsic dissipations [60]. To realize a Hadamard gate (H-gate), it is required that the frequency

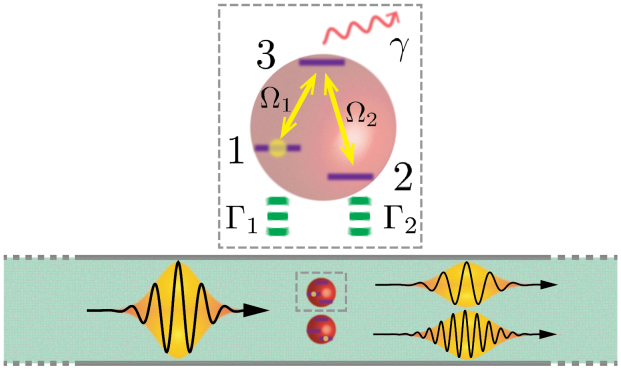

Figure 7.2: Schematics of Hadamard gate implementation. Two collocated Λ-type atoms (represented by red spheres) are coupled to a one-dimensional chiral photonic waveguide, which are initialized at different ground states. A single-photon Fock state is incoming from the left. Ω, γ, and Γ denote the atomic transition frequency, atomic dissipation rate, and atom-photon coupling, respectively. The subscript 1,2 represent transition 1 ($1 \leftrightarrow 3$) and 2 ($2 \leftrightarrow 3$), respectively.

difference of two dipole transitions is much larger than the atom-photon coupling strength, *i.e.*, $|\Omega_1 - \Omega_2| \gg \Gamma_1, \Gamma_2$, to be explained later. The injected optical pulse is near resonance with one dipole transition but far detuned with the other such that any incident photon only interacts with exactly one atom. To illustrate the physics, no dipole-dipole interactions between two atoms are taken into account.

The system Hamiltonian is described by

$$\begin{aligned}\frac{H}{\hbar} = &\int dx c^\dagger(x)(-iv_g\partial_x)c(x) + \int dx V_1\left[c^\dagger(x)\sigma_{31} + \sigma_{13}c(x)\right] + \int dx V_2\left[c^\dagger(x)\sigma_{32} + \sigma_{23}c(x)\right] \\ &+(\omega_3 - i\gamma)a_3^\dagger a_3 + \omega_2 a_2^\dagger a_2 + \omega_1 a_1^\dagger a_1,\end{aligned} \tag{7.1}$$

where $c^\dagger(x)$ ($c(x)$) denotes the creation (annihilation) operator for a right-propagating photon at position x. $a_j^\dagger$ (a_j) is the creation (annihilation) operator for the atomic state j ($j = 1, 2, 3$), which has a state energy of $\hbar\omega_j$. $\sigma_{ij} = a_j^\dagger a_i$ denotes the atomic transition operation from state i to state j. $\Omega_1 \equiv \omega_3 - \omega_1$ and $\Omega_2 \equiv \omega_3 - \omega_2$ are atomic transition frequencies of transitions 1 and 2, respectively. V_1 and V_2 represent the dipole-field coupling strength of transitions 1 and

2, respectively. In principle, V_1 and V_2 can be complex numbers while they are assumed to be real to facilitate the notations. The complex case can be readily generalized. $\Gamma_1 \equiv V_1^2/v_g$ and $\Gamma_2 \equiv V_2^2/v_g$ are dipole transition decay rate into the waveguided modes for transition 1 and 2, respectively. The general single-photon state only includes one atom. The general single-photon Fock state is described by

$$|\Phi\rangle = \left(\int dx \left[\phi_1(x) c^\dagger(x) a_1^\dagger + \phi_2(x) c^\dagger(x) a_2^\dagger \right] + e a_3^\dagger \right) |\varnothing\rangle, \tag{7.2}$$

where $|\varnothing\rangle$ is the photonic vacuum state that has no waveguided photon with no atomic state. ϕ_1 (ϕ_2) denotes the single-photon wave function when the atom is at the state 1 (2). e denotes the atomic excitation amplitude at state 3. By applying Schrödinger equation, $H|\Phi\rangle = \hbar\epsilon|\Phi\rangle$ ($\hbar\epsilon$ denotes single-photon energy), one obtains the following equations of motion

$$\begin{aligned} \epsilon\phi_1(x) =& -iv_g\partial_x\phi_1(x) + V_1\delta(x)e + \omega_1\phi_1(x), \\ \epsilon\phi_2(x) =& -iv_g\partial_x\phi_2(x) + V_2\delta(x)e + \omega_2\phi_2(x), \\ \epsilon e =& V_1\phi_1(0) + V_2\phi_2(0) + (\omega_3 - i\gamma)e. \end{aligned} \tag{7.3}$$

7.2.2 Operation Mechanism

Binary qubit information is encoded by photon frequency degree of freedom. For instance, a single photon of frequency kv_g is explicitly defined in the single-photon Hilbert space $|k\rangle = \frac{1}{\sqrt{2\pi}} \int dx e^{ikx} c^\dagger(x)|\varnothing\rangle$. The orthonormal relation is described by $\langle k_1|k_2\rangle = \delta(k_1 - k_2)$.

Now consider the case when a single photon is injected into the waveguide. Its frequency $k_1 v_g$ is near resonance with the dipole transition 1, *i.e.*, $|k_1 v_g - \Omega_1| \sim \Gamma_1$ yet far detuned with the atom initially at state 2 because $|k_1 v_g - \Omega_2| \gg \max(\Gamma_1, \Gamma_2)$. Consequently, the incident photon merely interacts with the atom that is initially at ground state 1. The reason is that

the photon is far detuned with the atom initially at state 2 because $|k_1 v_g - \Omega_2| \gg \max(\Gamma_1, \Gamma_2)$. In such a scenario, the incoming state can be expressed as

$$\begin{aligned} \phi_1(x) =& e^{ik_1 x}\left[\theta(-x) + t_1\theta(x)\right], \\ \phi_2(x) =& e^{ik_2 x} t_2 \theta(x), \end{aligned} \tag{7.4}$$

where $k_1 v_g$ and $k_2 v_g$ denote the frequency of emitted photons when the atom is relaxed to state 1 and 2, respectively. t_1 and t_2 represent the transmission amplitude for the single photon conversion $|k_1\rangle \rightarrow |k_1\rangle$ and $|k_1\rangle \rightarrow |k_2\rangle$, respectively. By solving the eigenstate involving Eqs. (7.3) and (7.4), the following frequency conversion is achieved

$$|k_1\rangle \rightarrow \frac{k_1 v_g - \Omega_1 + i\gamma - \frac{i}{2}(\Gamma_1 - \Gamma_2)}{k_1 v_g - \Omega_1 + i\gamma + \frac{i}{2}(\Gamma_1 + \Gamma_2)}|k_1\rangle + \frac{-i\sqrt{\Gamma_1\Gamma_2}}{k_1 v_g - \Omega_1 + i\gamma + \frac{i}{2}(\Gamma_1 + \Gamma_2)}|k_2\rangle, \tag{7.5}$$

which is referred to as Operation 1 (O1) throughout this chapter. Similarly, for another photon of frequency $k_2 v_g$, which is near resonant with Ω_2 (*i.e.*, $|k_2 v_g - \Omega_2| \sim \Gamma_2$) to excite the atom that is initially at ground state 2 only, it can be shown that

$$|k_2\rangle \rightarrow \frac{-i\sqrt{\Gamma_1\Gamma_2}}{k_2 v_g - \Omega_2 + i\gamma + \frac{i}{2}(\Gamma_1 + \Gamma_2)}|k_1\rangle + \frac{k_2 v_g - \Omega_2 + i\gamma + \frac{i}{2}(\Gamma_1 - \Gamma_2)}{k_2 v_g - \Omega_2 + i\gamma + \frac{i}{2}(\Gamma_1 + \Gamma_2)}|k_2\rangle, \tag{7.6}$$

referred to as Operation 2 (O2) throughout. The underlying physics here is the frequency conversion through Raman scattering process (*i.e.*, $|k_1\rangle \rightarrow |k_2\rangle$ during which ground state 1 is converted to ground state 2, or vice versa) that is mediated by the atomic excited state. When a combined condition of $k_1 v_g = \Omega_1,\ k_2 v_g = \Omega_2, \Gamma_2/\Gamma_1 = (\sqrt{2}-1)^2,\ \gamma = 0$ is fulfilled, and by defining binary qubit definition of $|0\rangle = |k_1\rangle,\ |1\rangle = |k_2\rangle$, it follows that

$$\begin{aligned} |0\rangle \rightarrow& -\frac{1}{\sqrt{2}}\left(|0\rangle + |1\rangle\right), \\ |1\rangle \rightarrow& -\frac{1}{\sqrt{2}}\left(|0\rangle - |1\rangle\right). \end{aligned} \tag{7.7}$$

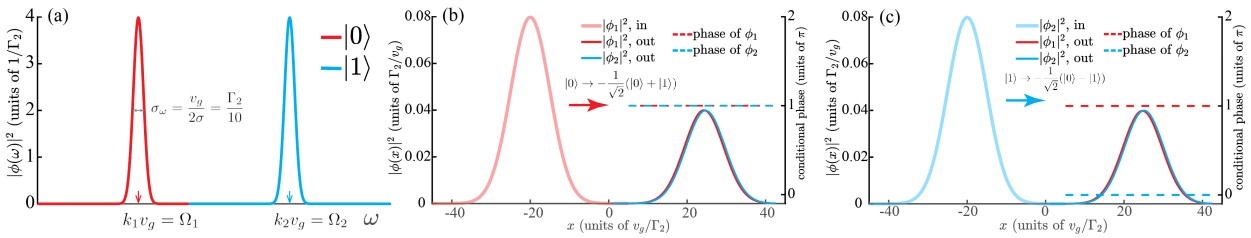

Figure 7.3: Demonstration of Hadamard gate operations. (a) Frequency-domain binary qubit wave function plot using finite bandwidth Gaussian pulse. Wave function density of in/out-states and acquired phase of out-state for (b) O1 and (c) O2.

7.2.3 Gate Demonstration

To demonstrate the gate operations (Eq. (7.1)), we investigate the single-photon Raman scattering process for a practical Gaussian pulse of a narrow bandwidth of $\Gamma_2/10$, as represented by frequency-domain wave function density (solid curves in Fig. 7.3(a)).

By employing the time-evolution operator approach on an in-state $|\chi_{\text{in}}\rangle$ (see Ref. [100] for detailed procedures), the out-state $|\chi_{\text{out}}\rangle = e^{-iHt/\hbar}|\chi_{\text{in}}\rangle$ can be obtained. Note that $|\chi_{\text{out}}\rangle$ should contain complete information of emitted single-photon wave function ϕ_1 (when atom relaxed to state 1, corresponding to $|k_1\rangle$) and ϕ_2 (when atom relaxed to state 2, corresponding to $|k_2\rangle$). Incident pulse is represented by the translucently red curve in Fig. 7.3(b). Emitted wave function density $|\phi_1|^2$ and $|\phi_2|^2$ are represented by red and blue curves in Fig. 7.3(c), respectively. Apparently, $|\phi_1|^2$ and $|\phi_2|^2$ essentially follow the same shape as the incoming pulse while density drops to only half, which confirms coefficient amplitude relation of $1/\sqrt{2}$ in Eq. (7.7). On the other hand, a precise π-phase shift is observed to confirm the amplitude phase -1 in Eq. (7.7). By quantitative examinations of the transmission amplitude and phase information, O1 ($|0\rangle \rightarrow -\frac{1}{\sqrt{2}}(|0\rangle + |1\rangle)$) is now confirmed.

Following similar procedures, we investigate O2 using the same aforementioned incident Gaussian pulse (translucently blue curve in Fig. 7.3(c)). As can be observed, $|\phi_1|^2$ and

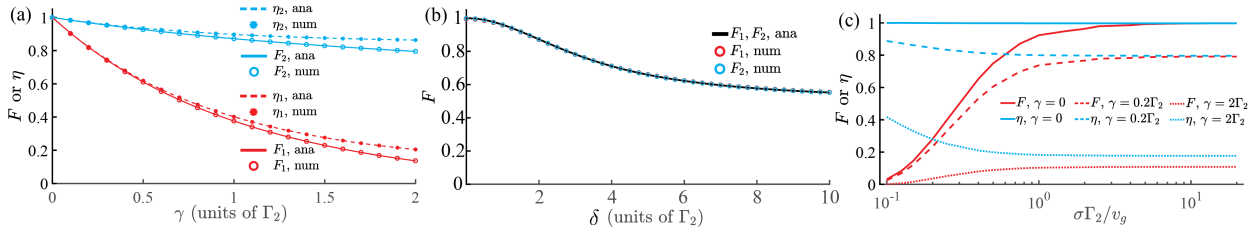

Figure 7.4: Hadamard gate performance of fidelity F and efficiency η as a function of system parameters. (a) Effects of γ on F and η. (b) Effects of Δ on F. (c) Effects of photon bandwidth on combined fidelity F and combined efficiency η for varying $\gamma = 0,\ 0.2\Gamma_2$, and $2\Gamma_2$.)

$|\phi_2|^2$ decrease to one half of that of the incoming pulse to confirm the amplitude relation. Moreover, ϕ_1 and ϕ_2 acquire phase shift of π and 0, respectively. Consequently, O2 ($|1\rangle \rightarrow -\frac{1}{\sqrt{2}}(|0\rangle - |1\rangle)$) is now confirmed.

7.2.4 Gate Performance

To quantify gate performances, we define two metrics, fidelity ($F_{1(2)}$), and efficiency ($\eta_{1(2)}$) for O1 (O2). Specifically, F characterizes the similarity of out-state $|\chi_{\text{out}}\rangle$ to the expected state $|\chi_{\text{expect}}\rangle$, *i.e.*, $F = |\langle\chi_{\text{expect}}|\chi_{\text{out}}\rangle|^2$. Note that $|\chi_{\text{expect}}\rangle = -\frac{1}{\sqrt{2}}(|0\rangle + |1\rangle)$ for O1 and $|\chi_{\text{expect}}\rangle = -\frac{1}{\sqrt{2}}(|0\rangle - |1\rangle)$ for O2. By invoking such a metric in Fig. 7.3(b)(c), $F_1 \approx 99.67\%$ and $F_2 \approx 99.91\%$ are obtained, respectively, implying that H-gate operates in a highly faithful manner. On the other hand, coupling between the system of interest and the environment results in irreversible photon leakages, which manifest as dissipations. Dissipations lead to photonic flux loss, thus degrading detecting efficiency. Efficiency η can be evaluated by photonic flux remained in the system of interest, *i.e.*, $\eta = \langle\chi_{\text{out}}|\chi_{\text{out}}\rangle$. $\eta_1 = \eta_2 = 1$ are obtained in Fig. 7.3(b)(c).

By adopting two metrics, we study effects of atomic dissipations (γ) and photon frequency detuning (Δ), respectively. When dissipations are present solely ($\gamma \neq 0, \Delta = 0$), by defining

$\lambda = \frac{\Gamma_1 - \Gamma_2}{2},\ \mu = \sqrt{\Gamma_1 \Gamma_2},\ \nu = \frac{\Gamma_1 + \Gamma_2}{2}$, gate operations (Eqs. (7.5) and (7.6)) now turn into

$$\begin{aligned} |0\rangle &\rightarrow \frac{\gamma - \lambda}{\gamma + \nu}|0\rangle + \frac{-\mu}{\gamma + \nu}|1\rangle, \\ |1\rangle &\rightarrow \frac{-\mu}{\gamma + \nu}|0\rangle + \frac{\gamma + \lambda}{\gamma + \nu}|1\rangle. \end{aligned} \tag{7.8}$$

Considering that $|\chi_{\text{expect}}\rangle$ remains unchanged as Eq. (7.7), fidelity and efficiency are obtained by $F_1(\gamma) = \frac{1}{2}\left(\frac{\gamma-\lambda-\mu}{\gamma+\nu}\right)^2$, $F_2(\gamma) = \frac{1}{2}\left(\frac{\gamma+\lambda+\mu}{\gamma+\nu}\right)^2$, $\eta_1(\gamma) = 1 - \frac{2\gamma(\nu+\lambda)}{\gamma^2+\nu^2+2\gamma\nu}$, and $\eta_2(\gamma) = 1 - \frac{2\gamma(\nu-\lambda)}{\gamma^2+\nu^2+2\gamma\nu}$. Results are plotted in Fig. 7.4(a): firstly, when γ increases, both $F_{1,2}$ and $\eta_{1,2}$ monotonically decrease, indicating that dissipations degrade the fidelity and efficiency for both operations; secondly, the decreasing rate of F as a function of γ is slightly shorter than that of η for both operations, which indicates that the fidelity has an upper limit of efficiency; and thirdly, the decreasing rate for O2 is much smaller than that of O1, which implies that O2 is more robust to the effects of dissipations. We further numerically confirm the results using the same aforementioned Gaussian pulses, as denoted by stars and circles in Fig. 7.4(a).

On the other hand, when only frequency detuning is present ($\gamma = 0, \Delta \neq 0$), the incident photon for O1 and O2 are of frequency $k_1 v_g = \Omega_1 + \Delta$ and $k_2 v_g = \Omega_2 + \Delta$, respectively. By redefining $|0\rangle = |k_1\rangle,\ |1\rangle = |k_2\rangle$, gate operations (Eqs. (7.5) and (7.6)) now yield

$$\begin{aligned} |0\rangle &\rightarrow \frac{\Delta - i\lambda}{\Delta + i\nu}|0\rangle + \frac{-i\mu}{\Delta + i\nu}|1\rangle, \\ |1\rangle &\rightarrow \frac{-i\mu}{\Delta + i\nu}|0\rangle + \frac{\Delta + i\lambda}{\Delta + i\nu}|1\rangle, \end{aligned} \tag{7.9}$$

thereby giving rise to ungraded efficiency ($\eta_1(\Delta) = \eta_2(\Delta) \equiv 1$) and degraded fidelity $F_1(\Delta) = \frac{1}{2}\left(1 + \frac{2\lambda\mu}{\Delta^2+\nu^2}\right)$ and $F_2(\Delta) = \frac{1}{2}\left(1 + \frac{2\lambda\mu}{\Delta^2+\nu^2}\right)$. As observed in Fig. 7.4(b), first, fidelity as a function of detuning is the same for both operations; secondly, fidelity decreases as $|\Delta|$ increases and has an lower limit $1/2$ as $|\Delta| \rightarrow \infty$; and thirdly, fidelity only depends on the

magnitude of detuning (Δ) whereas irrelevant to the red- or blue- shift base (sign of Δ). All three observations are further numerically confirmed, as represented by circles in Fig. 7.4(b).

In practice, the practical pulse of finite photon bandwidth may contain substantial off-resonance frequency component to compromise the fidelity and efficiency. Here we numerically investigate F and η as a function of photon bandwidth σ_ω (noting that $\sigma\Gamma_2/v_g = \Gamma_2/2\sigma_\omega$) for varying dissipation cases $\gamma = 0, 0.2\Gamma_2, 2\Gamma_2$. Specifically, to describe the overall performance for both operations, we adopt the combined fidelity $F = F_1F_2$ and combined efficiency $\eta = \eta_1\eta_2$ as evaluation metrics. As shown in Fig. 7.4(c), when $\sigma\Gamma_2/v_g$ increases (*i.e.*, decreasing photon bandwidth σ_ω), fidelity monotonically increases due to increasing resonance frequency component. Nonetheless, the efficiency monotonically decreases because more photon leakages emerge in the resonance case than that in the off-resonant case. When $\sigma\Gamma_2/v_g \to \infty$ (*i.e.*, $\sigma_\omega \to 0$ to exhibit asymptotic single-frequency behavior), both F and η can be asymptotically predicted by the single-frequency analytical results.

7.2.5 Universal Single-qubit Operation

The presented configuration is not restricted to H-gate solely. Remarkably, by properly tuning free parameters, it provides versatile utilities to achieve an arbitrary unitary single-qubit operation. Particularly, to fulfill the versatile utilities, photon-emitter interaction Γ_2/Γ_1 and frequency detuning Δ/Γ_1 need to be properly manipulated. The atom is assumed to be non-dissipative ($\gamma = 0$). Under such requirement, the gate operations can be summarized by transformation matrix in a more compact way described by $U = \begin{bmatrix} \frac{\Delta-i\lambda}{\Delta+i\nu} & \frac{-i\mu}{\Delta+i\nu} \\ \frac{-i\mu}{\Delta+i\nu} & \frac{\Delta+i\lambda}{\Delta+i\nu} \end{bmatrix}$. It has been shown that arbitrary single-qubit operation can be decomposed into three rotations on Bloch sphere: (1) rotate ζ w.r.t. the z-axis; (2) rotate θ w.r.t. the y-axis; and (3) rotate β w.r.t. the z-axis, subject to a trivial global phase α [12]. Correspondingly, the transformation

matrix is described by $U = e^{i\alpha} R_z(\beta) R_y(\theta) R_z(\zeta) = e^{i\alpha} \begin{bmatrix} e^{-\frac{i}{2}(\zeta+\beta)} \cos\frac{\theta}{2} & -e^{\frac{i}{2}(\zeta-\beta)} \sin\frac{\theta}{2} \\ e^{-\frac{i}{2}(\zeta-\beta)} \sin\frac{\theta}{2} & e^{\frac{i}{2}(\zeta+\beta)} \cos\frac{\theta}{2} \end{bmatrix}$. By relating two transformation matrices, it can be shown that when a combined condition of

$$\frac{\Delta}{\Gamma_1} = \frac{\tan\zeta}{2}\left[\left(\sqrt{c^2+1}-c\right)^2 - 1\right],\ \frac{\Gamma_2}{\Gamma_1} = \left(\sqrt{c^2+1}-c\right)^2,\ c = \left|\frac{\cos\zeta}{\tan\frac{\theta}{2}}\right|, \tag{7.10}$$

is fulfilled, a universal single-qubit operation can be achieved with rotation angles specified by

$$\begin{aligned} &\zeta, \theta \text{ arbitrary},\ \beta = \zeta + (2m_1+1)\pi, m_1 \in \mathbf{Z}, \\ &\alpha = \arctan\left[\tan\zeta \frac{\left[\left(\sqrt{c^2+1}-c\right)^2 - 1\right]}{\left[\left(\sqrt{c^2+1}-c\right)^2 + 1\right]}\right] + (m_2 + \frac{1}{2})\pi, m_2 \in \mathbf{Z}. \end{aligned} \tag{7.11}$$

Note that β is not free because we have assumed that V_1, V_2 are real numbers. In principle, when V_1, V_2 are complex numbers, arbitrary β can be realized, thus enabling a genuinely arbitrary single-qubit rotation.

In addition, we report five representative single-qubit gates that can be realized by properly tuning Γ_2/Γ_1 and Δ/Γ_1 in Table 7.1. It is worth noting that the condition of $\Gamma_2/\Gamma_1 = 0$ represents the situation that Λ-type atom reduces to a two-level atom whereby only a single atom rather than two is needed in the configuration (Fig. 7.2).

Table 7.1: Five representative single-qubit gates realized by manipulating Γ_2/Γ_1 and Δ/Γ_1 in the presented configuration (Fig. 7.2).

Gate	Hadamard	X	Z	S	T
Δ/Γ_1	0	0	0	$\frac{1}{2}$	$\frac{\sqrt{2}+1}{2}$
Γ_2/Γ_1	$(\sqrt{2}-1)^2$	1	0	0	0
U	$(-1)\frac{1}{\sqrt{2}}\begin{bmatrix} 1 & 1 \\ 1 & -1 \end{bmatrix}$	$(-1)\begin{bmatrix} 0 & 1 \\ 1 & 0 \end{bmatrix}$	$(-1)\begin{bmatrix} 1 & 0 \\ 0 & -1 \end{bmatrix}$	$e^{-i\frac{\pi}{2}}\begin{bmatrix} 1 & 0 \\ 0 & i \end{bmatrix}$	$e^{-i\frac{\pi}{4}}\begin{bmatrix} 1 & 0 \\ 0 & e^{i\frac{\pi}{4}} \end{bmatrix}$

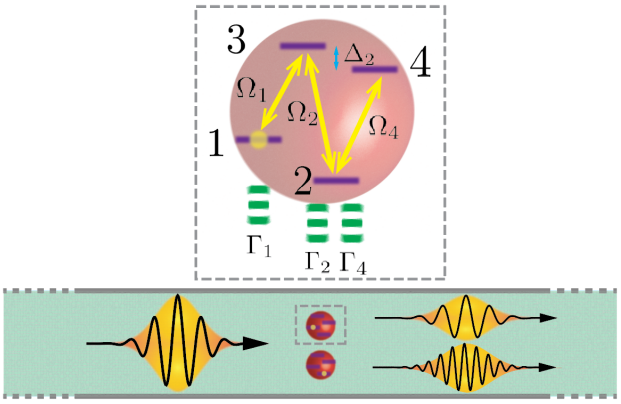

Figure 7.5: Alternative Hadamard gate scheme using N-type four-level system. Dipole transition $2 \leftrightarrow 4$ of transition frequency Ω_4 and photon-emitter coupling strength Γ_4. $\Delta_2 \equiv \Omega_2 - \Omega_4$. Dipole transition $1 \leftrightarrow 3$ and $2 \leftrightarrow 3$ have photon-emitter coupling strengths of Γ_1 and Γ_2, respectively.

7.2.6 Alternative N-type Four-level System Scheme

So far, we have laid out an analysis of H-gate proposal using Λ-type atom architectures. Moreover, such a scheme requires a significantly different photon-emitter coupling of transitions 1 and 2, $\Gamma_2/\Gamma_1 \approx 0.17$. Notably, for practical Λ-type atoms, it follows that $\Gamma_2/\Gamma_1 \approx 1$. Thus, an experimentally accessible scheme requires $\Gamma_1 \approx \Gamma_2$.

Here we show that by introducing an extra state 4 to form an N-type atomic state, H-gate operations are still fulfilled subject to the requirement of $\Gamma_1 = \Gamma_2$. Figure 7.5 plots the schematic diagram wherein a new state 4 enables another dipole transition $2 \leftrightarrow 4$ of transition frequency Ω_4 and photon-emitter coupling strength Γ_4. $\Delta_2 \equiv \Omega_4 - \Omega_2$ denotes transition frequency difference. To yield desired H-gate operations, we found two resonance conditions.

1. **Resonant Condition 1**

Firstly, when $\Delta = \Gamma/\sqrt{2}, \sqrt{2}\Delta_2 + \Gamma_4/4 = -\Gamma$, the transformation described by $U = -\frac{i}{\sqrt{2}}\begin{bmatrix} 1 & 1 \\ 1 & -1 \end{bmatrix}$ is realized, which connects to H-gate operation subject to a global phase of $-\pi/2$. Apparently, when such resonance condition holds, Δ and Γ are in the same order of magnitude. Note that an N-type atom is typically enabled by a hyperfine structure, which is of a typical energy shift Δ_2 at an order of magnitude, 10GHz [107]. Due to the advent of strong coupling techniques, atom-photon coupling of 10GHz is readily applicable [30], thereby consolidating the experimental feasibility.

2. **Resonant Condition 2**

   Analogously, the second resonance condition requires $\Delta = -\Gamma/\sqrt{2}, -\sqrt{2}\Delta_2 + \Gamma_4/4 = -\Gamma$, thus leading to desired H-gate operations described by $U = \frac{i}{\sqrt{2}}\begin{bmatrix} 1 & 1 \\ 1 & -1 \end{bmatrix}$ subject to a global phase $\pi/2$.

7.3 S Gate Proposal

The single-qubit S gate introduces a $\pi/4$ phase shift for one particular qubit, described by the unitary matrix $\begin{bmatrix} 1 & 0 \\ 0 & i \end{bmatrix}$. As schematically shown in Fig. 7.6(a), a single two-level system is chirally coupled to a photonic waveguide. By exploiting photon frequency degree of freedom and defining $|0\rangle = |\Omega + \frac{\Gamma}{2}\rangle$ and $|1\rangle = |\Omega + \Delta\rangle$ ($|\Delta| \gg \Gamma$), it can be shown that $|0\rangle \to e^{-i\pi/2}|0\rangle$ and $|1\rangle \to |1\rangle$ to fulfill a S-gate operation subject to a global phase $\pi/2$.

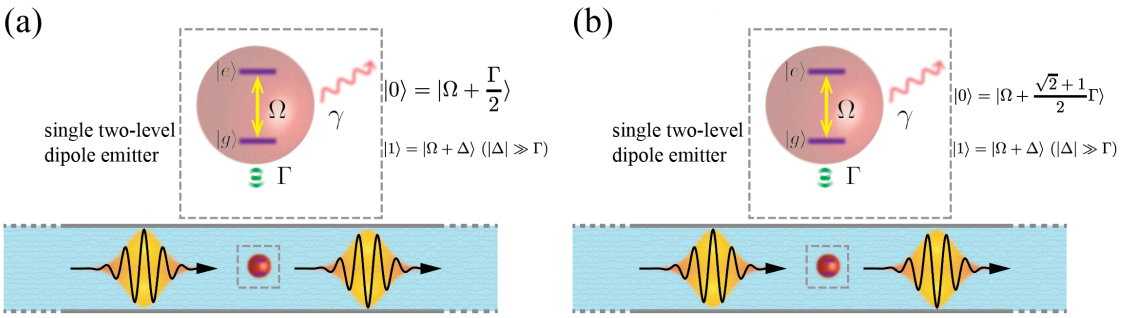

Figure 7.6: Schematics of (a) S and (b) T gate proposals.

7.4 T Gate Proposal

Similar to S gate, the schematics for T gate is shown in Fig. 7.6(b), which performs the operation of $\begin{bmatrix} 1 & 0 \\ 0 & e^{i\frac{\pi}{4}} \end{bmatrix}$. By defining $|0\rangle = |\Omega + \frac{\sqrt{2}+1}{2}\Gamma\rangle$ and $|1\rangle = |\Omega + \Delta\rangle$ $(|\Delta| \gg \Gamma)$, it can be shown that $|0\rangle \to e^{-i\pi/4}|0\rangle$ and $|1\rangle \to |1\rangle$ to fulfill a S-gate operation subject to a global phase $\pi/4$.

7.5 Summary and Outlook

In this chapter, we present proposals of three single-qubit quantum logic gates using chiral waveguide QED systems. Our proposals are of a deterministic nature and a high scalability. Due to the advent of directional emissions, the required chiral coupling condition is readily available. Our work provides recipe in designing quantum logic gates by exploiting photon-emitter interactions, and unearth possibility of implementing frequency-based quantum logic gates in quantum nanophotonics [108, 109].

References

1. Shor, P. Algorithms for quantum computation: discrete logarithms and factoring in *Proceedings 35th Annual Symposium on Foundations of Computer Science* (IEEE Comput. Soc. Press, 1994).
2. Grover, L. K. A fast quantum mechanical algorithm for database search (1996).
3. Monroe, C., Meekhof, D. M., King, B. E., Itano, W. M. & Wineland, D. J. Demonstration of a Fundamental Quantum Logic Gate. *Physical Review Letters* **75,** 4714–4717 (1995).
4. Wallraff, A. et al. Strong coupling of a single photon to a superconducting qubit using circuit quantum electrodynamics. *Nature* **431,** 162–167 (2004).
5. Loss, D. & DiVincenzo, D. P. Quantum computation with quantum dots. *Physical Review A* **57,** 120–126 (1998).
6. Cory, D. G., Fahmy, A. F. & Havel, T. F. Ensemble quantum computing by NMR spectroscopy. *Proceedings of the National Academy of Sciences* **94,** 1634–1639 (1997).
7. Gershenfeld, N. A. & Chuang, I. L. Bulk Spin-Resonance Quantum Computation. *Science* **275,** 350–356 (1997).
8. Kane, B. E. A silicon-based nuclear spin quantum computer. *Nature* **393,** 133–137 (1998).
9. Manson, N. B., Harrison, J. P. & Sellars, M. J. Nitrogen-vacancy center in diamond: Model of the electronic structure and associated dynamics. *Physical Review B* **74,** 104303 (2006).
10. O'Brien, J. L., Furusawa, A. & Vučković, J. Photonic quantum technologies. *Nature Photonics* **3,** 687–695 (2009).
11. Northup, T. E. & Blatt, R. Quantum information transfer using photons. *Nature Photonics* **8,** 356–363 (2014).
12. Nielsen, M. A. & Chuang, I. Quantum Computation and Quantum Information (2002).
13. Knill, E., Laflamme, R. & Milburn, G. J. A scheme for efficient quantum computation with linear optics. *Nature* **409,** 46–52 (2001).

14. Aaronson, S. & Arkhipov, A. The Computational Complexity of Linear Optics. *Theory of Computing* **9,** 143–252 (2013).

15. Raussendorf, R. & Briegel, H. J. A One-Way Quantum Computer. *Physical Review Letters* **86,** 5188–5191 (2001).

16. Briegel, H. J. & Raussendorf, R. Persistent Entanglement in Arrays of Interacting Particles. *Physical Review Letters* **86,** 910–913 (2001).

17. Gottesman, D. & Chuang, I. L. Demonstrating the viability of universal quantum computation using teleportation and single-qubit operations. *Nature* **402,** 390–393 (1999).

18. Chuang, I. L. & Yamamoto, Y. Simple quantum computer. *Physical Review A* **52,** 3489–3496 (1995).

19. Kok, P., Lee, H. & Dowling, J. P. Single-photon quantum-nondemolition detectors constructed with linear optics and projective measurements. *Physical Review A* **66,** 063814 (2002).

20. Shen, J.-T. & Fan, S. Strongly Correlated Two-Photon Transport in a One-Dimensional Waveguide Coupled to a Two-Level System. *Physical Review Letters* **98,** 153003 (2007).

21. Shen, Y. & Shen, J.-T. Photonic-Fock-state scattering in a waveguide-QED system and their correlation functions. *Physical Review A* **92,** 033803 (2015).

22. Davidovich, L., Brune, M., Raimond, J. M. & Haroche, S. Mesoscopic quantum coherences in cavity QED: Preparation and decoherence monitoring schemes. *Physical Review A* **53,** 1295–1309 (1996).

23. Blais, A., Huang, R.-S., Wallraff, A., Girvin, S. M. & Schoelkopf, R. J. Cavity quantum electrodynamics for superconducting electrical circuits: An architecture for quantum computation. *Physical Review A* **69,** 062320 (2004).

24. Shen, J. T. & Fan, S. Coherent photon transport from spontaneous emission in one-dimensional waveguides. *Optics Letters* **30,** 2001 (2005).

25. Hennessy, K. et al. Quantum nature of a strongly coupled single quantum dot–cavity system. *Nature* **445,** 896–899 (2007).

26. Fushman, I., Englund, D., Faraon, A., Stoltz, N., Petroff, P. & Vuckovic, J. Controlled Phase Shifts with a Single Quantum Dot. *Science* **320,** 769–772 (2008).

27. Astafiev, O., Zagoskin, A. M., Abdumalikov, A. A., Pashkin, Y. A., Yamamoto, T., Inomata, K., Nakamura, Y. & Tsai, J. S. Resonance Fluorescence of a Single Artificial Atom. *Science* **327,** 840–843 (2010).

28. O'Connell, A. D. et al. Quantum ground state and single-phonon control of a mechanical resonator. *Nature* **464,** 697–703 (2010).

29. Hausmann, B. J. M. et al. Integrated Diamond Networks for Quantum Nanophotonics. *Nano Letters* **12,** 1578–1582 (2012).

30. Tiecke, T. G., Thompson, J. D., de Leon, N. P., Liu, L. R., Vuletić, V. & Lukin, M. D. Nanophotonic quantum phase switch with a single atom. *Nature* **508,** 241–244 (2014).

31. Cortes, C. L., Newman, W., Molesky, S. & Jacob, Z. Corrigendum: Quantum nanophotonics using hyperbolic metamaterials. *Journal of Optics* **16,** 129501 (2014).

32. Goban, A., Hung, C.-L., Hood, J., Yu, S.-P., Muniz, J., Painter, O. & Kimble, H. Superradiance for Atoms Trapped along a Photonic Crystal Waveguide. *Physical Review Letters* **115,** 063601 (2015).

33. González-Tudela, A., Paulisch, V., Chang, D., Kimble, H. & Cirac, J. Deterministic Generation of Arbitrary Photonic States Assisted by Dissipation. *Physical Review Letters* **115,** 163603 (2015).

34. Sipahigil, A. et al. An integrated diamond nanophotonics platform for quantum-optical networks. *Science* **354,** 847–850 (2016).

35. Deutsch, I. H., Chiao, R. Y. & Garrison, J. C. Diphotons in a nonlinear Fabry-Pérot resonator: Bound states of interacting photons in an optical "quantum wire". *Physical Review Letters* **69,** 3627–3630 (1992).

36. Cheng, Z. & Kurizki, G. Optical "Multiexcitons": Quantum Gap Solitons in Nonlinear Bragg Reflectors. *Physical Review Letters* **75,** 3430–3433 (1995).

37. Drummond, P. D. & He, H. Optical mesons. *Physical Review A* **56,** R1107–R1109 (1997).

38. Firstenberg, O., Peyronel, T., Liang, Q.-Y., Gorshkov, A. V., Lukin, M. D. & Vuletić, V. Attractive photons in a quantum nonlinear medium. *Nature* **502,** 71–75 (2013).

39. Bradford, M. & Shen, J.-T. Numerical approach to statistical properties of resonance fluorescence. *Optics Letters* **39,** 5558 (2014).

40. Zheng, H. & Baranger, H. U. Persistent Quantum Beats and Long-Distance Entanglement from Waveguide-Mediated Interactions. *Physical Review Letters* **110,** 113601 (2013).

41. Gonzalez-Ballestero, C., Moreno, E. & Garcia-Vidal, F. J. Generation, manipulation, and detection of two-qubit entanglement in waveguide QED. *Physical Review A* **89,** 042328 (2014).

42. Li, Q., Zhou, L. & Sun, C. P. Waveguide quantum electrodynamics: Controllable channel from quantum interference. *Physical Review A* **89,** 063810 (2014).

43. Calajó, G., Ciccarello, F., Chang, D. & Rabl, P. Atom-field dressed states in slow-light waveguide QED. *Physical Review A* **93,** 033833 (2016).

44. Schneider, M. P., Sproll, T., Stawiarski, C., Schmitteckert, P. & Busch, K. Green's-function formalism for waveguide QED applications. *Physical Review A* **93,** 013828 (2016).

45. Mirza, I. M. & Schotland, J. C. Multiqubit entanglement in bidirectional-chiral-waveguide QED. *Physical Review A* **94,** 012302 (2016).

46. Liao, Z., Zeng, X., Nha, H. & Zubairy, M. S. Photon transport in a one-dimensional nanophotonic waveguide QED system. *Physica Scripta* **91,** 063004 (2016).

47. Liao, Z., Al-Amri, M. & Zubairy, M. S. Measurement of deep-subwavelength emitter separation in a waveguide-QED system. *Optics Express* **25,** 31997 (2017).

48. Lu, Y., Gao, S., Fang, A., Li, P., Li, F. & Zubairy, M. S. Coherent frequency down-conversions and entanglement generation in a Sagnac interferometer. *Optics Express* **25,** 16151 (2017).

49. Yang, D.-C., Cheng, M.-T., Ma, X.-S., Xu, J., Zhu, C. & Huang, X.-S. Phase-modulated single-photon router. *Physical Review A* **98,** 063809 (2018).

50. Tian, T. & Song, L. J. Collective effect of single-photon scattering on the three-level atomic array. *EPL (Europhysics Letters)* **124,** 34002 (2018).

51. Song, G.-Z., Kwek, L.-C., Deng, F.-G. & Long, G.-L. Microwave transmission through an artificial atomic chain coupled to a superconducting photonic crystal. *Physical Review A* **99,** 043830 (2019).

52. Parit, M. K., Ahmed, S., Singh, S., Lakshmi, P. A. & Panigrahi, P. K. Correlated photons of desired characteristics from a dipole coupled three-atom system. *OSA Continuum* **2,** 2293 (2019).

53. Liang, Q.-Y. et al. Observation of three-photon bound states in a quantum nonlinear medium. *Science* **359,** 783–786 (2018).

54. Xu, C., Zipfel, W., Shear, J. B., Williams, R. M. & Webb, W. W. Multiphoton fluorescence excitation: new spectral windows for biological nonlinear microscopy. *Proceedings of the National Academy of Sciences* **93,** 10763–10768 (1996).

55. Hell, S. W. Three-photon excitation in fluorescence microscopy. *Journal of Biomedical Optics* **1,** 71 (1996).

56. Boto, A. N., Kok, P., Abrams, D. S., Braunstein, S. L., Williams, C. P. & Dowling, J. P. Quantum Interferometric Optical Lithography: Exploiting Entanglement to Beat the Diffraction Limit. *Physical Review Letters* **85,** 2733–2736 (2000).

57. Tsang, M. Quantum Imaging beyond the Diffraction Limit by Optical Centroid Measurements. *Physical Review Letters* **102,** 253601 (2009).

58. Giovannetti, V., Lloyd, S., Maccone, L. & Shapiro, J. H. Sub-Rayleigh-diffraction-bound quantum imaging. *Physical Review A* **79,** 013827 (2009).

59. Turchette, Q. A., Hood, C. J., Lange, W., Mabuchi, H. & Kimble, H. J. Measurement of Conditional Phase Shifts for Quantum Logic. *Physical Review Letters* **75,** 4710–4713 (1995).

60. Chen, Z., Zhou, Y. & Shen, J.-T. Exact dissipation model for arbitrary photonic Fock state transport in waveguide QED systems. *Optics Letters* **42,** 887 (2017).

61. Hofheinz, M. et al. Generation of Fock states in a superconducting quantum circuit. *Nature* **454,** 310–314 (2008).

62. Firstenberg, O., Adams, C. S. & Hofferberth, S. Nonlinear quantum optics mediated by Rydberg interactions. *Journal of Physics B: Atomic, Molecular and Optical Physics* **49,** 152003 (2016).

63. Zhou, Y., Chen, Z. & Shen, J.-T. Single-photon superradiant emission rate scaling for atoms trapped in a photonic waveguide. *Physical Review A* **95,** 043832 (2017).

64. Zhou, Y., Chen, Z. & Shen, J.-T. Ultrafast single-photon spontaneous emission from an array of quantum-emitters along a photonic waveguide in *Photonic and Phononic Properties of Engineered Nanostructures VIII*. **10541** (SPIE, 2018).

65. Chen, Z., Zhou, Y. & Shen, J.-T. Three-photon molecule generation through coherent scattering process in nonlinear quantum nanophotonics in *Quantum Nanophotonics 2018*. **10734** (SPIE, 2018).

66. Zhou, Y., Chen, Z. & Shen, J.-T. Orders of magnitude enhancement in two photon excitation efficiency using photonic molecules in *Quantum Communications and Quantum Imaging XVI*. **10771** (SPIE, 2018).

67. Zhou, Y., Chen, Z., Wang, L. V. & Shen, J.-T. Efficient two-photon excitation by photonic dimers. *Optics Letters* **44,** 475 (2019).

68. Chen, Z., Zhou, Y. & Shen, J.-T. Photon antibunching and bunching in a ring-resonator waveguide quantum electrodynamics system. *Optics Letters* **41,** 3313 (2016).

69. Chen, Z., Zhou, Y. & Shen, J.-T. Photonic bound state and antibunching generations in atom-ring resonator-waveguide QED system in *Photonic and Phononic Properties of Engineered Nanostructures VIII*. **10541** (SPIE, 2018).

70. Petrov, N., Fedotov, A. & Zheltikov, A. High-brightness photon pairs and strongly antibunching heralded single photons from a highly nonlinear optical fiber. *Optics Communications* **450,** 304–307 (2019).

71. Liu, J., Zhou, M. & Yu, Z. Quantum scattering theory of a single-photon Fock state in three-dimensional spaces. *Optics Letters* **41,** 4166 (2016).

72. Shen, J.-T. & Fan, S. Theory of single-photon transport in a single-mode waveguide. I. Coupling to a cavity containing a two-level atom. *Physical Review A* **79,** 023837 (2009).

73. Verslegers, L., Yu, Z., Catrysse, P. B. & Fan, S. Temporal coupled-mode theory for resonant apertures. *Journal of the Optical Society of America B* **27,** 1947 (2010).

74. Senitzky, I. R. Dissipation in Quantum Mechanics. The Harmonic Oscillator. *Physical Review* **119,** 670–679 (1960).

75. Lindblad, G. On the generators of quantum dynamical semigroups. *Communications in Mathematical Physics* **48,** 119–130 (1976).

76. Scully, M. O. & Zubairy, M. S. Quantum Optics (Cambridge University Press, 1997).

77. Gardiner, C. W. & Collett, M. J. Input and output in damped quantum systems: Quantum stochastic differential equations and the master equation. *Physical Review A* **31,** 3761–3774 (1985).

78. Zoller, P., Marte, M. & Walls, D. F. Quantum jumps in atomic systems. *Physical Review A* **35,** 198–207 (1987).

79. Dalibard, J., Castin, Y. & Mølmer, K. Wave-function approach to dissipative processes in quantum optics. *Physical Review Letters* **68,** 580–583 (1992).

80. Sirtori, C., Faist, J., Capasso, F., Sivco, D. L., Hutchinson, A. L. & Cho, A. Y. Quantum cascade laser with plasmon-enhanced waveguide operating at 8.4 μm wavelength. *Applied Physics Letters* **66,** 3242–3244 (1995).

81. Joannopoulos, J. D., Johnson, S. G., Winn, J. N. & Meade, R. D. Photonic crystals: molding the flow of light (Princeton university press, 2011).

82. Selvaraja, S. K., Sleeckx, E., Schaekers, M., Bogaerts, W., Thourhout, D. V., Dumon, P. & Baets, R. Low-loss amorphous silicon-on-insulator technology for photonic integrated circuitry. *Optics Communications* **282,** 1767–1770 (2009).

83. Lee, H., Chen, T., Li, J., Yang, K. Y., Jeon, S., Painter, O. & Vahala, K. J. Chemically etched ultrahigh-Q wedge-resonator on a silicon chip. *Nature Photonics* **6,** 369–373 (2012).

84. Chen, Z., Zhou, Y. & Shen, J.-T. Entanglement-preserving approach for reservoir-induced photonic dissipation in waveguide QED systems. *Physical Review A* **98,** 053830 (2018).

85. Shen, J.-T. & Fan, S. Strongly correlated multiparticle transport in one dimension through a quantum impurity. *Physical Review A* **76,** 062709 (2007).

86. Imamolu, A., Schmidt, H., Woods, G. & Deutsch, M. Strongly Interacting Photons in a Nonlinear Cavity. *Physical Review Letters* **79,** 1467–1470 (1997).

87. Peyronel, T., Firstenberg, O., Liang, Q.-Y., Hofferberth, S., Gorshkov, A. V., Pohl, T., Lukin, M. D. & Vuletić, V. Quantum nonlinear optics with single photons enabled by strongly interacting atoms. *Nature* **488,** 57–60 (2012).

88. Thompson, J. D. et al. Symmetry-protected collisions between strongly interacting photons. *Nature* **542,** 206–209 (2017).

89. Kimble, H. J. The quantum internet. *Nature* **453,** 1023–1030 (2008).

90. Quijandría, F., Porras, D., García-Ripoll, J. J. & Zueco, D. Circuit QED Bright Source for Chiral Entangled Light Based on Dissipation. *Physical Review Letters* **111,** 073602 (2013).

91. Poyatos, J. F., Cirac, J. I. & Zoller, P. Quantum Reservoir Engineering with Laser Cooled Trapped Ions. *Physical Review Letters* **77,** 4728–4731 (1996).

92. Murch, K. W., Vool, U., Zhou, D., Weber, S. J., Girvin, S. M. & Siddiqi, I. Cavity-Assisted Quantum Bath Engineering. *Physical Review Letters* **109,** 183602 (2012).

93. Brennecke, F., Mottl, R., Baumann, K., Landig, R., Donner, T. & Esslinger, T. Real-time observation of fluctuations at the driven-dissipative Dicke phase transition. *Proceedings of the National Academy of Sciences* **110,** 11763–11767 (2013).

94. Chen, Z., Zhou, Y. & Shen, J.-T. Dissipation-induced photonic-correlation transition in waveguide-QED systems. *Physical Review A* **96,** 053805 (2017).

95. Zheng, H., Gauthier, D. J. & Baranger, H. U. Waveguide-QED-Based Photonic Quantum Computation. *Physical Review Letters* **111,** 090502 (2013).

96. Duan, L.-M. & Kimble, H. J. Scalable Photonic Quantum Computation through Cavity-Assisted Interactions. *Physical Review Letters* **92,** 127902 (2004).

97. Gorshkov, A. V., Otterbach, J., Demler, E., Fleischhauer, M. & Lukin, M. D. Photonic Phase Gate via an Exchange of Fermionic Spin Waves in a Spin Chain. *Physical Review Letters* **105,** 060502 (2010).

98. Ralph, T., Söllner, I., Mahmoodian, S., White, A. & Lodahl, P. Photon Sorting, Efficient Bell Measurements, and a Deterministic Controlled-ZGate Using a Passive Two-Level Nonlinearity. *Physical Review Letters* **114,** 173603 (2015).

99. Biswas, A. & Agarwal, G. S. Quantum logic gates using Stark-shifted Raman transitions in a cavity. *Physical Review A* **69,** 062306 (2004).

100. Shen, Y., Chen, Z., He, Y., Li, Z. & Shen, J.-T. Exact approach for spatiotemporal dynamics of spontaneous emissions in waveguide quantum electrodynamic systems. *Journal of the Optical Society of America B* **35,** 607 (2018).

101. Guo, A., Salamo, G. J., Duchesne, D., Morandotti, R., Volatier-Ravat, M., Aimez, V., Siviloglou, G. A. & Christodoulides, D. N. Observation ofPT-Symmetry Breaking in Complex Optical Potentials. *Physical Review Letters* **103,** 093902 (2009).

102. Wang, Z., Chong, Y. D., Joannopoulos, J. D. & Soljačić, M. Reflection-Free One-Way Edge Modes in a Gyromagnetic Photonic Crystal. *Physical Review Letters* **100,** 013905 (2008).

103. Söllner, I. et al. Deterministic photon–emitter coupling in chiral photonic circuits. *Nature Nanotechnology* **10,** 775–778 (2015).

104. Lodahl, P., Mahmoodian, S., Stobbe, S., Rauschenbeutel, A., Schneeweiss, P., Volz, J., Pichler, H. & Zoller, P. Chiral quantum optics. *Nature* **541,** 473–480 (2017).

105. Gaisser, T. K., Engel, R. & Resconi, E. Cosmic Rays and Particle Physics (Cambridge University Press, 2016).

106. Chen, Z., Zhou, Y. & Shen, J.-T. Single-channel Hadamard gate by exploiting frequency conversion of single-photon Raman scattering in chiral quantum nanophotonics in *Advances in Photonics of Quantum Computing, Memory, and Communication XII*. **10933** (SPIE, 2019).

107. Bason, M. G., Mohapatra, A. K., Weatherill, K. J. & Adams, C. S. Narrow absorptive resonances in a four-level atomic system. *Journal of Physics B: Atomic, Molecular and Optical Physics* **42,** 075503 (2009).

108. Kobayashi, T. et al. Frequency-domain Hong–Ou–Mandel interference. *Nature Photonics* **10,** 441–444 (2016).

109. Kues, M. et al. On-chip generation of high-dimensional entangled quantum states and their coherent control. *Nature* **546,** 622–626 (2017).

110. Pletcher, R. H., Tannehill, J. C. & Anderson, D. A. Computational Fluid Mechanics and Heat Transfer 774 pp. (Taylor & Francis Inc, 2012).

111. Ascher, U. M. Numerical Methods for Evolutionary Differential Equations (Computational Science and Engineering) (Society for Industrial and Applied Mathematics, 2008).

112. Breuer, H.-P. & Petruccione, F. The theory of open quantum systems (Oxford University Press on Demand, 2002).

Appendix A

Computational Approach of Ab-initio Three-photon Dynamics

Here we present the ab-initio computational approach to study the spatio-temporal three-photon dynamics in Eqs. (2.3) and (2.4). Notably, they fall into the category of hyperbolic differential equations, which have first-order derivatives in both space and time. Given the initial condition of an injected wave packet, and a suitable boundary condition (*e.g.*, periodic boundary condition, hard-wall boundary condition, etc), the hyperbolic problem is well-posed and widely studied [110]. Nonetheless, the emergence of Dirac-δ functions are quite annoying as they may introduce singularities on the numerical mesh to cause the computational approach blow up. It is worth noting that the Fourier image of Dirac-δ function is a trivial constant over the entire momentum space. Consequently, to study the equations alternatively in the reciprocal momentum space might be a proper option to work around the singularity in the real space methods.

To begin with, we adopt the following Fourier transform for a single variable as follows

$$\begin{aligned}\phi_k(k) &= \frac{1}{\sqrt{2\pi}}\int dx e^{-ikx}\phi(x),\\ \phi(x) &= \frac{1}{\sqrt{2\pi}}\int dk e^{ikx}\phi_k(k),\end{aligned} \tag{A.1}$$

where $\phi(x)$ is the single-particle wave function in real space with $\phi_k(k)$ is its Fourier image in the momentum space. With this in mind, the Fourier image of Dirac-δ function is mapped to a constant of $1/\sqrt{2\pi}$. In Eqs. (2.3) and (2.4), there are three types of wave functions subject to Fourier transforms, that is, three-photon wave function (*e.g.*, $\phi_{RRR}(x_1, x_2, x_3)$), atomic excitation wave function (*e.g.*, $e_{RR}(x_1, x_2)$), and three-photon wave function with one variable evaluated at a constant (*e.g.*, $\phi_{RRR}(x_1, x_2, 0)$). By defining the three-dimensional Fourier transform for the three-photon wave function (without loss of generality, use ϕ_{RRR} as an example) as follows

$$\phi_{k_{RRR}}(k_1, k_2, k_3) = \frac{1}{(2\pi)^{3/2}}\iiint dx_1 dx_2 dx_3 \phi_{RRR}(x_1, x_2, x_3) e^{-i(k_1x_1+k_2x_2+k_3x_3)}, \tag{A.2}$$

two-dimensional Fourier transform for the two-photon wave function (without loss of generality, use e_{RR} as an example) as follows

$$e_{k_{RR}}(k_1, k_2) = \frac{1}{2\pi}\iint dx_1 dx_2 \phi_{RR}(x_1, x_2) e^{-i(k_1x_1+k_2x_2)}, \tag{A.3}$$

and two-dimensional Fourier transform for $\phi_{RRR}(x_1, x_2, 0)$ as follows

$$\begin{aligned}\phi_{k_{RR}R}(k_1, k_2, x_3 = 0) =& \frac{1}{2\pi}\iint dx_1 dx_2 \phi_{RRR}(x_1, x_2, x_3 = 0) e^{-i(k_1x_1+k_2x_2)}\\ =& \frac{1}{\sqrt{2\pi}}\int dk_3 e^{ik_3x_3}|_{x_3=0}\phi_{k_{RRR}}(k_1, k_2, k_3)\\ =& \frac{1}{\sqrt{2\pi}}\int dk_3 \phi_{k_{RRR}}(k_1, k_2, k_3),\end{aligned} \tag{A.4}$$

Eqs. (2.3) and (2.4) can be transformed into fully momentum-space representation

$$
\begin{aligned}
\partial_t \phi_{k_{RRR}} =& - iv_g \left(k_1 + k_2 + k_3\right) \phi_{k_{RRR}} - \frac{i\bar{V}}{\sqrt{6\pi}} \Big[e_{k_{RR}}(k_2, k_3) + e_{k_{RR}}(k_1, k_3) + e_{k_{RR}}(k_1, k_2) \Big] e^{-i\Omega t}, \\
\partial_t \phi_{k_{RRL}} =& - iv_g \left(k_1 + k_2 - k_3\right) \phi_{k_{RRL}} - \frac{i\bar{V}}{\sqrt{6\pi}} \Big[e_{k_{RL}}(k_2, k_3) + e_{k_{RL}}(k_1, k_3) + e_{k_{RR}}(k_1, k_2) \Big] e^{-i\Omega t}, \\
\partial_t \phi_{k_{RLR}} =& - iv_g \left(k_1 - k_2 + k_3\right) \phi_{k_{RLR}} - \frac{i\bar{V}}{\sqrt{6\pi}} \Big[e_{k_{LR}}(k_2, k_3) + e_{k_{RR}}(k_1, k_3) + e_{k_{RL}}(k_1, k_2) \Big] e^{-i\Omega t}, \\
\partial_t \phi_{k_{RLL}} =& - iv_g \left(k_1 - k_2 - k_3\right) \phi_{k_{RLL}} - \frac{i\bar{V}}{\sqrt{6\pi}} \Big[e_{k_{LL}}(k_2, k_3) + e_{k_{RL}}(k_1, k_3) + e_{k_{RL}}(k_1, k_2) \Big] e^{-i\Omega t}, \\
\partial_t \phi_{k_{LRR}} =& iv_g \left(k_1 - k_2 - k_3\right) \phi_{k_{LRR}} - \frac{i\bar{V}}{\sqrt{6\pi}} \Big[e_{k_{RR}}(k_2, k_3) + e_{k_{LR}}(k_1, k_3) + e_{k_{LR}}(k_1, k_2) \Big] e^{-i\Omega t}, \\
\partial_t \phi_{k_{LRL}} =& iv_g \left(k_1 - k_2 + k_3\right) \phi_{k_{LRL}} - \frac{i\bar{V}}{\sqrt{6\pi}} \Big[e_{k_{RL}}(k_2, k_3) + e_{k_{LL}}(k_1, k_3) + e_{k_{LR}}(k_1, k_2) \Big] e^{-i\Omega t}, \\
\partial_t \phi_{k_{LLR}} =& iv_g \left(k_1 + k_2 - k_3\right) \phi_{k_{LLR}} - \frac{i\bar{V}}{\sqrt{6\pi}} \Big[e_{k_{LR}}(k_2, k_3) + e_{k_{LR}}(k_1, k_3) + e_{k_{LL}}(k_1, k_2) \Big] e^{-i\Omega t}, \\
\partial_t \phi_{k_{LLL}} =& iv_g \left(k_1 + k_2 + k_3\right) \phi_{k_{LLL}} - \frac{i\bar{V}}{\sqrt{6\pi}} \Big[e_{k_{LL}}(k_2, k_3) + e_{k_{LL}}(k_1, k_3) + e_{k_{LL}}(k_1, k_2) \Big] e^{-i\Omega t}, \\
\partial_t e_{k_{RR}} =& - \gamma e_{k_{RR}} - iv_g \left(k_1 + k_2\right) e_{k_{RR}} - i\frac{\bar{V}}{\sqrt{6\pi}} \Big\{ \int dk_1 \Big[\phi_{k_{RRR}} + \phi_{k_{LRR}} \Big] + \int dk_2 \Big[\phi_{k_{RRR}} + \phi_{k_{RLR}} \Big] \\
& + \int dk_3 \Big[\phi_{k_{RRR}} + \phi_{k_{RRL}} \Big] \Big\} e^{i\Omega t}, \\
\partial_t e_{k_{RL}} =& - \gamma e_{k_{RL}} - iv_g \left(k_1 - k_2\right) e_{k_{RL}} - i\frac{\bar{V}}{\sqrt{6\pi}} \Big\{ \int dk_1 \Big[\phi_{k_{RRL}} + \phi_{k_{LRL}} \Big] + \int dk_2 \Big[\phi_{k_{RRL}} + \phi_{k_{RLL}} \Big] \\
& + \int dk_3 \Big[\phi_{k_{RLR}} + \phi_{k_{RLL}} \Big] \Big\} e^{i\Omega t}, \\
\partial_t e_{k_{LR}} =& - \gamma e_{k_{LR}} + iv_g \left(k_1 - k_2\right) e_{k_{LR}} - i\frac{\bar{V}}{\sqrt{6\pi}} \Big\{ \int dk_1 \Big[\phi_{k_{RLR}} + \phi_{k_{LLR}} \Big] + \int dk_2 \Big[\phi_{k_{LRR}} + \phi_{k_{LLR}} \Big] \\
& + \int dk_3 \Big[\phi_{k_{LRR}} + \phi_{k_{LRL}} \Big] \Big\} e^{i\Omega t}, \\
\partial_t e_{k_{LL}} =& - \gamma e_{k_{LL}} + iv_g \left(k_1 + k_2\right) e_{k_{LL}} - i\frac{\bar{V}}{\sqrt{6\pi}} \Big\{ \int dk_1 \Big[\phi_{k_{RLL}} + \phi_{k_{LLL}} \Big] + \int dk_2 \Big[\phi_{k_{LRL}} + \phi_{k_{LLL}} \Big] \\
& + \int dk_3 \Big[\phi_{k_{LLR}} + \phi_{k_{LLL}} \Big] \Big\} e^{i\Omega t},
\end{aligned}
\tag{A.5}
$$

which are now converted to ordinary differential equations (ODE) because no partial derivatives show up any longer. Simulation methods of ODE are well studied in the textbook [111].

We adopt the numerical approach of a second-order accuracy in time, in which a paradigm to illustrate the essential spirit is shown as follows

$$\begin{aligned} \dot{f}(t) =& af(t) + g(t), \\ \Rightarrow f(t+\Delta t) =& f(t)e^{a\Delta t} + g(t+\frac{\Delta t}{2})e^{a\frac{\Delta t}{2}}\Delta t. \end{aligned} \tag{A.6}$$

To fully trace out the spatial-temporal three-photon dynamics, we initiate the momentum-space wave functions as follows

$$\phi_{k_{RRR}}(k_1,k_2,k_3,t=0) = \left(\frac{2\sigma^2}{\pi}\right)^{3/4} e^{-\sigma^2(k_1-k_o)^2-\sigma^2(k_2-k_o)^2-\sigma^2(k_3-k_o)^2} e^{-i(k_1-k_o)x_o-i(k_2-k_o)x_o-i(k_3-k_o)x_o}, \tag{A.7}$$

where k_o, x_o, and σ are photon center frequency, initial position, and pulse width. Typically, assuming the pulse is incident from the left, $x_o < -3.3\sigma$ to guarantee that $> 99.9\%$ pulse energy is involved in the scattering process. k_o and σ may vary depending on particular physical situation of interest. For instance, the most common scenario of interest is a narrow-bandwidth resonant pulse injected to the waveguide, in which $k_o = \Omega/v_g$ and $\sigma = 5v_g/\Gamma$ (corresponding to photon bandwidth $v_g/2\sigma{=}\Gamma/10$). The initialization equivalent to inject an uncorrelated three-photon pulse of the Gaussian profile described by

$$\phi_{RRR}(x_1,x_2,x_3,t=0) = \frac{1}{(2\pi\sigma^2)^{3/4}} e^{-\frac{(x_1-x_o)^2}{4\sigma^2}-\frac{(x_2-x_o)^2}{4\sigma^2}-\frac{(x_3-x_o)^2}{4\sigma^2}} e^{i\frac{\omega_o}{v_g}x_1+i\frac{\omega_o}{v_g}x_2+i\frac{\omega_o}{v_g}x_3}. \tag{A.8}$$

At the final time t_f, we apply inverse Fourier transform on the momentum-space wave function to end up with the real-space wave function $\phi(x_1,x_2,x_3,t_f)$, which are visualized and further processed.

Appendix B

Effective Mapping from Three-level to Two-level System

Here we present the analytical procedures to show that in the far-detuned regime, the intermediate state of the three-level ladder system can be adiabatically eliminated so that the three-level system can be effectively mapped to a two-level system with renormalized system parameters. To illustrate the physics, the calculation is performed in the single-photon picture. The Hamiltonian of the effective two-level system in Fig. B.1(a) is

$$\begin{aligned}\frac{H}{\hbar} &= \int dx c^\dagger(x)(\omega_a + \Delta_o - iv_g\partial_x)c(x) + \int dx V_o\delta(x)\left[c^\dagger(x)\sigma_- + \sigma_+ c(x)\right] + \omega_a a_e^\dagger a_e \\ &= \underbrace{\int dx(\omega_a + \Delta_o)c^\dagger(x)c(x) + \omega_a a_e^\dagger a_e}_{H_o} + \underbrace{\int dx c^\dagger(x)(-iv_g\partial_x)c(x) + \int dx V_o\delta(x)\left[c^\dagger(x)\sigma_- + \sigma_+ c(x)\right]}_{H_1},\end{aligned} \tag{B.1}$$

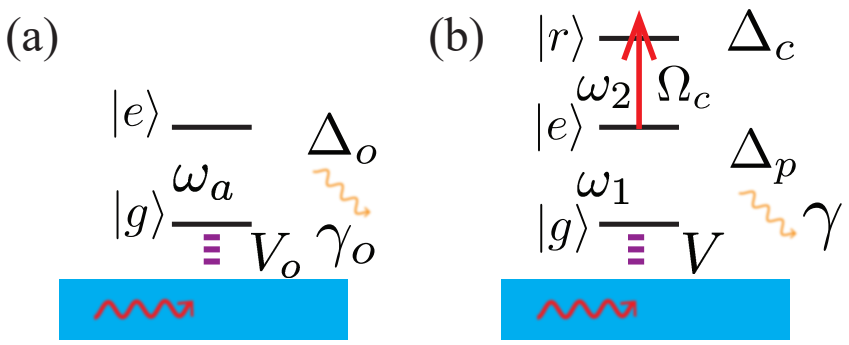

Figure B.1: Effective mapping from a three-level ladder system (b) to a two-level system (a). In (a), $|e\rangle$ and $|g\rangle$ are atomic excited and ground states, respectively, which is weakly driven by individual photons injected into the waveguide. Parameters are defined by: ω_a is transition frequency; Δ_o is single-photon detuning; γ_o is spontaneous emission rate into non-waveguided modes that manifest as dissipation rate; and V_o is atom-photon coupling strength. In (b), $|r\rangle$, $|e\rangle$, and $|g\rangle$ are excited, intermediate, and ground states, respectively. $e \leftrightarrow g$ is weakly driven similar to (a) of coupling strength V while $r \leftrightarrow e$ is coupled to a strong laser of Rabi frequency Ω_c. ω_1 and ω_2 are respective transition frequencies. Δ_c and Δ_p are respective frequency detunings. γ is spontaneous emission rate into non-waveguided mode of transition $e \leftrightarrow g$.

where notations are defined in Fig. B.1 caption. H_o and H_1 describes the free and interaction parts, respectively. In the interaction picture, one has that

$$\begin{aligned} V_1(t) =& e^{i\frac{H_o}{\hbar}t} H_1 e^{-i\frac{H_o}{\hbar}t} \\ =& \int dx c^\dagger(x)(-iv_g\partial_x)c(x) + \int dx V_o \delta(x) \left[c^\dagger(x)\sigma_- e^{i\Delta_o t} + \sigma_+ c(x) e^{-i\Delta_o t}\right]. \end{aligned} \tag{B.2}$$

The general state is

$$|\Phi_1(t)\rangle = \left[\int dx \phi(x) c^\dagger(x) + e(t) e^{-i\Delta_o t} a_e^\dagger\right] |\varnothing\rangle, \tag{B.3}$$

where ϕ is single-photon wave function and e is atomic excitation amplitude. $|\varnothing\rangle$ denotes the photonic vacuum state. By applying the Schrödinger equation in the interaction picture, we

end up with the equations of motion

$$\begin{aligned}\partial_t\phi =& - v_g\partial_x\phi - iV_o e\delta(x),\\ \partial_t e =& \, i(\Delta_o + i\gamma_o)e - iV_o\phi(0).\end{aligned} \tag{B.4}$$

The Hamiltonian describing the three-level ladder system of Fig. B.1(b) in the interaction-picture is

$$\begin{aligned}V_2(t) =& \int dx c^\dagger(x)(-iv_g\partial_x)c(x) + \int dx V\delta(x)\left[c^\dagger(x)\sigma_{eg}e^{i\Delta_p t} + \sigma_{ge}c(x)e^{-i\Delta_p t}\right]\\ &+\frac{\Omega_c}{2}(|e\rangle\langle r|e^{i\Delta_c t} + |r\rangle\langle e|e^{-i\Delta_c t}).\end{aligned} \tag{B.5}$$

The general state is

$$|\Phi_2(t)\rangle = \left[\int dx\phi(x)c^\dagger(x) + e_1(t)e^{-i\Delta_p t}a_e^\dagger + e_2(t)e^{-i(\Delta_p+\Delta_c)t}a_r^\dagger\right]|\varnothing\rangle, \tag{B.6}$$

where e_1 and e_2 denote excitation amplitudes of $|e\rangle$ and $|r\rangle$, respectively. Other notations are defined the same as previous. By applying the Schrödinger equation in the interaction picture, one has that

$$\begin{aligned}\partial_t\phi =& - v_g\partial_x\phi - iVe_1\delta(x),\\ \partial_t e_1 =& \, i(\Delta_p + i\gamma)e_1 - iV\phi(0) - i\frac{\Omega_c}{2}e_2,\\ \partial_t e_2 =& \, i(\Delta_p + i\gamma + \Delta_c)e_2 - i\frac{\Omega_c}{2}e_1.\end{aligned} \tag{B.7}$$

It can be shown that in the far-detuned regime $|\Delta_p| \gg \Omega_c$, e_1 is approximated by $\frac{V}{(\Delta_p+i\gamma)}\phi(0,t) + \frac{\Omega_c}{2(\Delta_p+i\gamma)}e_2$. By substituting it into Eq. (B.7), e_1 can be adiabatically eliminated [76]

$$\begin{aligned}\partial_t\phi =& - v_g\partial_x\phi - i\frac{V\Omega_c}{2(\Delta_p + i\gamma)}e_2\delta(x),\\ \partial_t e_2 =& -i\frac{\Omega_c^2}{4(\Delta_p + i\gamma)}e_2 - i\frac{V\Omega_c}{2(\Delta_p + i\gamma)}\phi(0,t).\end{aligned} \tag{B.8}$$

By relating Eqs. (B.4) and (B.8) with the condition $V \ll \Omega_c$, the following effective mapping relation can be established

$$\begin{aligned} \Delta_o &= -\frac{\Omega_c^2 \Delta_p}{4(\Delta_p^2 + \gamma^2)}, \\ \gamma_o &= \frac{\Omega_c^2 \gamma}{4(\Delta_p^2 + \gamma^2)}. \end{aligned} \tag{B.9}$$

Appendix C

Material Loss Model Using Density Matrix Approach

In this appendix, for the material loss scenario presented in Chap. 4, we compare our entanglement-preserving approach with the conventional density matrix approach. The density matrix approach provides a probabilistic measure of the system dynamics while does not directly provide the information of the photonic wave function and the entanglement. By invoking the Markovian assumptions as in Ref. [76], the dynamics for the reduced density matrix of the atom is given by

$$\dot{\rho}_A = -\gamma_D[\sigma_+\sigma_-\rho_A - 2\sigma_-\rho_A\sigma_+ + \rho_A\sigma_+\sigma_-], \tag{C.1}$$

where $\gamma_D = \pi\eta^2(\Omega)D(\Omega)$ is the resulting dissipation rate. The right-hand side of Eq. (C.1) is exactly the Lindblad superoperator with a damping rate γ_D. First, the dissipation rate γ_D is the same as the lowest-order dissipation rate γ_1 in Eq. (4.6) in our entanglement-preserving approach, as the density matrix approach does not describe the photonic dynamics in the

reservoir (*i.e.*, the coherent hopping events described by the β's). That is, for coherent processes, only in the weak-reservoir limit ($\bar{\beta}\bar{D}\Delta\omega/\bar{\delta} \ll 1$), does the density matrix approach yields the approximate dissipation rate. Nonetheless, the frequency shift Δ_1 is not predicted by the density matrix approach even in the weak-reservoir limit. Our approach provides a framework to investigate the photonic loss mechanisms by engineering the excitable reservoir and beyond the weak-reservoir limit.

As a further comparison, we now apply the non-Markovian density matrix approach to investigate the same excitable reservoir scenario. After some algebra, it can be shown that ρ_A fulfills

$$\dot{\rho}_A(t) = -i\Delta_{NM}(t)\left[\sigma_+\sigma_-, \rho_A(t)\right] - \gamma_{NM}(t)\left[\sigma_+\sigma_-\rho_A(t) + \rho_A(t)\sigma_+\sigma_- - 2\sigma_-\rho_A(t)\sigma_+\right], \tag{C.2a}$$

$$\Delta_{NM}(t) = -\mathrm{Im}\left[\frac{\dot{a}(t)}{a(t)}\right], \quad \gamma_{NM}(t) = -\mathrm{Re}\left[\frac{\dot{a}(t)}{a(t)}\right], \tag{C.2b}$$

$$\begin{aligned}\dot{a}(t) =& (-i)^2 \sum_{i_1} \eta_{i_1}^2 e^{-i(\omega_{a_{i_1}} - \Omega - i\varepsilon)t} \int_{t_i}^{t} a(t_1) e^{i(\omega_{a_{i_1}} - \Omega - i\varepsilon)t_1} dt_1 \\ &+ \sum_{n=2}^{\infty} (-i)^{n+1} \sum_{i_1} \sum_{i_2 \neq i_1} \cdots \sum_{i_n \neq i_{n-1}} \eta_{i_1}\beta_{i_1 i_2}\cdots\beta_{i_{n-1}i_n}\eta_{i_n} e^{-i(\omega_{a_{i_1}} - \Omega - i\varepsilon)t} \times \\ &\int_{t_i}^{t} e^{i(\omega_{a_{i_1}} - \omega_{a_{i_2}})t_1} dt_1 \cdots \int_{t_i}^{t_{n-2}} e^{i(\omega_{a_{i_{n-1}}} - \omega_{a_{i_n}})t_{n-1}} dt_{n-1} \int_{t_i}^{t_{n-1}} a(t_n) e^{i(\omega_{a_{i_n}} - \Omega - i\varepsilon)t_n} dt_n,\end{aligned} \tag{C.2c}$$

where $\Delta_{NM}(t)$ and $\gamma_{NM}(t)$ are time-dependent frequency shift and dissipation rate for non-Markovian approach, respectively. Apparently, such a non-Markovian approach can describe photon hopping processes up to an arbitrary order of accuracy. Nonetheless, it again yields a mixed state solution to lose the coherence information [112]. Moreover, such a approach does not apply when multi-photon entanglement is necessarily taken into account, *e.g.*, two-photon

bound state solution. The comparison of the Markovian, the non-Markovian density matrix approaches, and the entanglement-preserving approach is summarized in Table C.1.

Table C.1: Comparison of Markovian and non-Markovian density matrix (DM) approach and the entanglement-preserving approach.

	Markovian DM	non-Markovian DM	Entanglement-Preserving
order of accuracy	lowest-order	all-order	all-order
multi-photon entanglement	$\times$	$\times$	$\surd$
state description	mixed state	mixed state	pure state